Università degli Studi di Torino
Facoltà di Scienze M.F.N.

Laurea Specialistica in
Fisica delle Interazioni Fondamentali

Physics performance of the ALICE muon spectrometer for pp collisions at 14 TeV

Candidato:
Diego Stocco

Relatore: **Prof. Ermanno Vercellin**

Controrelatore: **Prof. Mauro Anselmino**

Anno accademico: 2004/2005

Non all'arbitrio, non al cuore né al fato

Contents

Introduction

High-energy physics has established and validated over the last decades a detailed, though still incomplete, theory of elementary particles and their fundamental interactions: the Standard Model. Such theory has encountered a lot of success in explaining the phenomenology of interactions at a fundamental level, but further investigations are necessary in order, on one hand, to answer still unresolved questions and, on the other, to apply and extend the SM to complex and dynamically evolving systems of finite size.

The Large Hadron Collider (LHC), with its high center of mass energy and the possibility to accelerate both nucleons and nuclei, will provide a deep insight into such topics, as well as a deeper understanding of the underlying physics.

Among the four experiments at LHC, namely CMS, ATLAS, LHCb and ALICE, the latter is the only specifically dedicated to the analysis of ultra-relativistic heavy-ion collisions. The focus is to study and understand how collective phenomena and macroscopic properties, involving many degrees of freedom, emerge from the microscopic laws of elementary-particle physics. The most striking case of a collective bulk phenomenon predicted by the Standard Model, is the occurrence of phase transitions in quantum fields at characteristic energy densities. In particular, Quantum Chromodynamics (QCD) calculations foresee that at temperatures of about 170 MeV the ordinary hadronic matter, constituted by uncolored bound states of quarks, could undergo a transition to a new state of unbound quarks and gluons: the Quark Gluon Plasma (QGP).

The study of phase transitions is of great interest not only in particle physics, but also in cosmology. According to Big-Bang theory, the Universe evolved from an initial state of extremely high energy density to its present state through rapid expansion and cooling, thereby traversing the series of phase transitions predicted by the Standard Model. Global features of our Universe, like baryon-antibaryon asymmetry or large scale structures (galaxy distribution), are believed to be linked to characteristic properties of such transitions.

As far as we know, the only way to create and study the primordial

plasma in the laboratory is to collide two heavy nuclei and analyze the resulting small droplets of hot and dense medium. The system formed undergoes a fast dynamical evolution from the extreme initial conditions to the dilute final hadronic state, making direct measurements impossible. In order to test the characteristics of the new state of matter it is necessary to use suitable "probes". Among them, heavy quarkonium states such as J/ψ and Υ play an important role as a test of deconfinement.

Unfortunately, the probes are affected not only by the presence of the plasma, but also by other effects resulting from the use of the complex systems of ordinary matter: the heavy ions. An understanding of such effects can only be achieved through precise studies of nucleon-nucleon and nucleon-nucleus collisions, which represent an essential part of the ALICE programme. In addition, the analysis of those collisions holds an importance of its own as it will allow to extend the tests of the standard model to unexplored regions. From this point of view should be emphasized that, owing to its unique design, ALICE is probably the only LHC experiment with access to the low-p_T region.

The present work has the twofold aim of studying, through simulations, the physics performance of the ALICE muon spectrometer in the detection of heavy quarkonia produced in pp collisions at 14 TeV, and of exploring possible contributions to our present understanding of physics.

Chapter 1 provides a general overview of the physics that can be studied by the ALICE experiment. Its main goal, the analysis of the Quark-Gluon Plasma and its experimental observables, is described in more detail, with particular emphasis on heavy quarkonium states. A discussion of the most interesting features that will be analyzed in proton-proton collisions follows.

Chapter 2 presents a short description of the ALICE experiment. The section is meant as a brief summary of the characteristics of the main detectors, with a more detailed insight into the muon spectrometer.

As the focus of the present work is on heavy quarkonia, Chapter 3 shows a theoretical and experimental review about this topic. At present the quarkonia production relies on a number of models, which have been continuously tested by new experiments. A description of the most important is given, with a particular regard on the ones whose predictions match, to some extent, the most recent data. Finally, the latest results from Tevatron, the collider whose center of mass energy is closest to the one achievable at the LHC, are presented. A comparison of theoretical models predictions and such data closes the section.

In Chapter 4, a discussion of the "fast simulation" of the ALICE muon spectrometer is performed. Such a tool, employed in this work, allows the generation and analysis of quarkonia with high statistics, in an amount

of time significatively reduced with respect to the one needed by the full simulation.

The simulation results are described in Chapter 5. The mass spectra of the muon pairs are fitted by a suitable function in order to disentangle the signal, constituted by leptons from ψ and Υ resonances, from the background. It will be shown that the statistics is high enough to allow a measurement of the rapidity and transverse momentum distributions of quarkonia.

Finally, Chapter 6 analyzes one of the possible way to employ the rapidity distribution obtained in the previous chapter, in order to get information about the gluon distribution functions. The parton distributions (PDFs), fundamental in QCD calculations, can be determined only experimentally. However, depending on the energies achievable and on the detection features, each experiment can provide information on PDFs only in a limited region. The study performed in this chapter shows the possibility to use the heavy quarkonia detected in the ALICE muon spectrometer in order to explore the gluon distribution functions in the low x region, where, so far, only extrapolations are available.

Chapter 1

Physics with the ALICE experiment

The ALICE experiment is one of the four experiments at the Large Hadron Collider (LHC) at CERN. With a circumference of about 27 km and a center of mass energy of 14 TeV for *pp* collisions, LHC is the largest and most powerful in the world. The other three experiments (ATLAS, CMS and LHCb) will acquire data during proton-proton collisions, but ALICE is the only one specifically designed for heavy ion collisions.

However the detector is able to collect data even during *pp* runs, thus providing two specific physics programs.

1.1 Heavy ion (AA) collisions

The focus of heavy-ion physics is to study and understand how collective phenomena and macroscopic properties, involving many degrees of freedom, emerge from the microscopic laws of elementary-particle physics. Specifically, heavy-ion physics addresses these questions in the sector of strong interactions by studying nuclear matter under conditions of extreme density and temperature.

The nucleon-nucleon center of mass energy for collisions of the heaviest ions at the LHC ($\sqrt{s} = 5.5$ TeV) will exceed that available at the Relativistic Heavy Ion Collider (RHIC) by a factor of about 30, opening up a new physics domain. Heavy-ion collisions at the LHC access not only a quantitatively different regime of much higher energy density, but also a qualitatively new regime, mainly because:

1. A novel range of Bjorken-x values, where strong nuclear gluon shadowing is foreseen, can be accessed. The initial density of these low-x gluons is expected to be close to saturation.

2. Hard processes are produced at sufficiently high rates for detailed measurements.

3. Weakly interacting hard probes become accessible, thus providing information about nuclear parton distributions at very high Q^2.

4. Parton dynamics dominate the fireball expansion.

All these features will allow an accurate study of the phase transition in the hot and dense hadronic matter environment.

1.1.1 The Quark Gluon Plasma

The most striking case of a collective bulk of phenomenon predicted by the Standard Model is the occurrence of phase transitions in quantum fields at characteristic energy densities. The generic form of the QCD phase diagram is shown in figure 1.1. Lattice calculations of Quantum Chromodynamics predicts that at a critical temperature of $T_c \simeq 170$ MeV, corresponding to an energy density of $\varepsilon_c \simeq 1$ GeV/fm^3, nuclear matter undergoes a phase transition to a deconfined state of quarks and gluons. In addition, at high temperature T and vanishing chemical potential μ_B (quantity related to baryon-number density), chiral symmetry is approximately restored and quark masses are reduced from their large effective values in hadronic matter to their small bare ones.

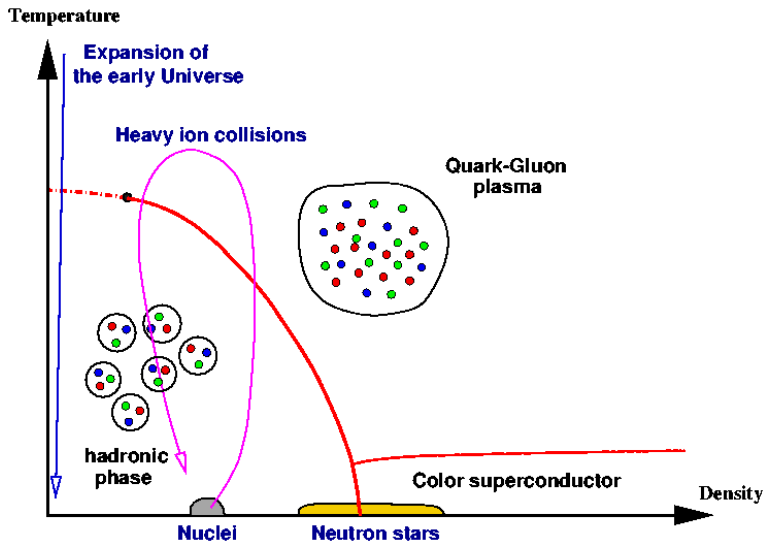

Fig. 1.1: The phase diagram of QCD

The basic mechanism for deconfinement in dense matter is the Debye screening of the color charge. When the screening radius r_D becomes less

than the binding radius r_H of the quark system (hadron), the confining force can no longer hold the quarks together and hence deconfinement sets in.

The phase transition can be well described by QCD thermodynamics, and in particular by finite temperature lattice calculations. However, the transition from hadronic matter to quark gluon plasma can be illustrated by simple and intuitive arguments, based on the "MIT bag model". This model describes the confined state of matter as an ideal gas of non-interacting massless pions, with essentially three degrees of freedom. On the contrary, even a two flavor quark gluon plasma (composed by massless u and d quarks only), has 16 gluonic and 12 quark degrees of freedom. In the passage from a confined to a deconfined state, the energy density, which is proportional to the degrees of freedom, undergoes a sudden enhancement (latent heat of deconfinement). The behavior is shown in figure 1.2, obtained with lattice calculations.

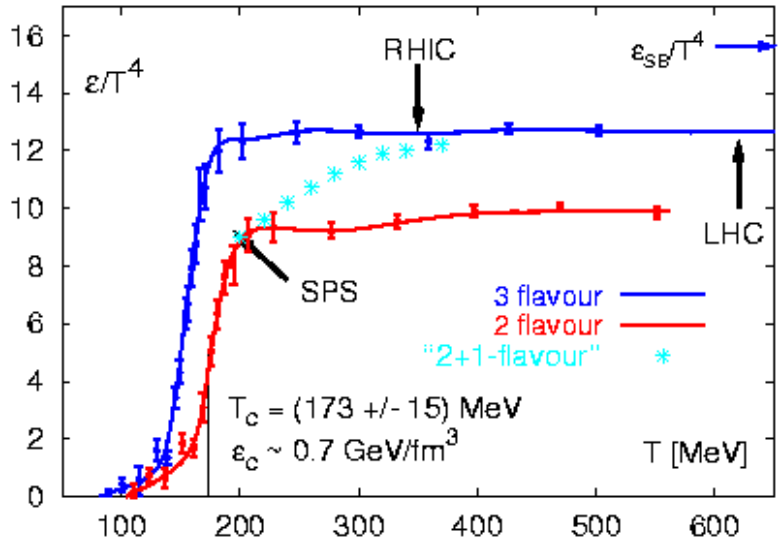

Fig. 1.2: Temperature dependence of the energy density over T^4 in QCD with 2 and 3 degenerate quark flavors as well as with two light and a heavier (strange) quark. The arrows on the right-side ordinates show the value of the Stefan-Boltzmann limit for an ideal quark-gluon gas.

At present the only way to achieve the energy densities necessary for the quark gluon plasma formation is through heavy ion collisions. The process that leads from the initial collision to hadronization and freeze-out, is described in figure 1.3. The main steps are:

- Pre-equilibrium ($\tau \leq 1$ fm/c). The initial partons scatter among each other giving rise to an abundant production of quarks and gluons.

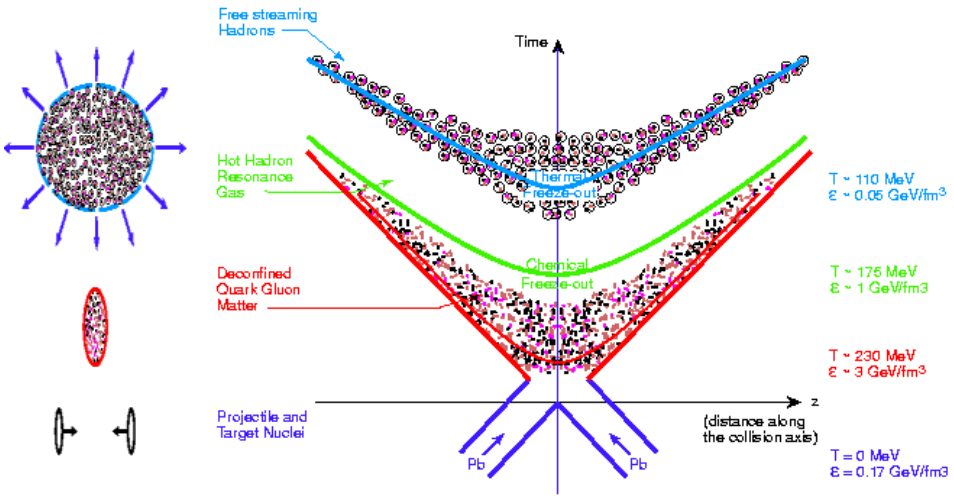

Fig. 1.3: Expected evolution of a nuclear collision

- Quark gluon plasma ($\tau \sim 10$ fm/c). The quark gluon gas evolves into thermal equilibrium: the QGP is formed and starts expanding.
- Mixed phase. The QGP, while expanding, starts converting into a hadron gas.
- Hadronization ($\tau \sim 20$ fm/c). As far as the system expands, its temperature decreases till quarks and gluons are again confined in hadrons.
- Freeze-out. Hadrons decouple from the gas, thus becoming free.

The very short lasting time of QGP (only few 10^{-23} s), together with the interdiction to detect free quarks, do not allow to directly measure the transition. Nevertheless, information are indirectly provided by series of "probes", specifically thought to test different aspects of the medium. In the following, a short overview of such signals will be presented.

1.1.2 Experimental signatures of QGP

The phase transitions are critical behaviors, and the general way to probe such behaviors consists in finding the transition point and determine how the system and its observables change from one side to the other. In the case of complex phenomena, such as the QGP formation, different observables can be used in order to investigate different aspects of the same system, in many phases of its evolution.

Probes of the equation of state

The basic idea behind this class of signatures is the identification of modifications in the dependence of energy density (ε), pressure (P) and entropy

density (s) of superdense hadronic matter on temperature T and baryochemical potential μ_B. A rapid rise in the ratios ε/T^4 or s/T^4 is, indeed, an evidence of a first-order phase transition.

The observables related to such quantities, obtainable through an analysis of the particle spectra, are the average transverse momentum $\langle p_T \rangle$ and the charged particle multiplicity per rapidity unit $\mathrm{d}N/\mathrm{d}y$ or transverse energy per rapidity unit at mid-rapidities $\mathrm{d}E_T/\mathrm{d}y$. In particular, a first-order transition should manifest itself through a saturation of $\langle p_T \rangle$ during the mixed phase.

Particle spectra can provide information about another class of phenomena related to the equation of state: the flow. With this term is meant a collective motion of particles, superimposed to the thermal one. The flow is directly related to the pressure gradient, and can quantify the effective equation of state of the matter.

Signatures of chiral symmetry restoration

One of the most important probes of the chiral symmetry restoration comes from the study of the light vector meson resonances, ρ, ω and ϕ. Such particles, created in the hot hadronic phase, can provide direct access to in-medium modifications. The ρ meson, in particular, plays a key role since its e^+e^- decay width (through which resonances are mainly detected) is a factor of ~ 10 (5) larger than the ω (ϕ). In addition, the ρ has a well-defined partner under $SU(2)$ chiral transformations, the $a_1(1260)$.

The approach toward restoration of chiral symmetry at T_c, requires the spectral distributions in the corresponding vector and axial channel to become degenerate. How this degeneracy occurs is one of the crucial questions related to the chiral phase transition.

The possibilities range from both the ρ and a_1 masses dropping to (almost) zero, the so-called Brown-Rho scaling conjecture, to a complete melting of the resonance structures, due to the intense rescattering in the hot and dense hadronic environment, or scenarios with rather stable resonance structures.

Soft probes of deconfinement: strangeness enhancement

In pp collisions, the production of particles containing strange quarks is strongly suppressed, as compared to the production of hadrons with u and d quarks. The suppression, probably due to the higher mass of the $s\bar{s}$ pair, increases with the strangeness content of the particles.

QGP formation in nucleus-nucleus collisions leads to a different scenario. In this case the strange hadron yield derives from two independent reaction steps following each other in time:

1. in a deconfined QGP, strange quark pairs ($s\bar{s}$) can be copiously produced through gluon-gluon fusion, while in hadronic gas $s\bar{s}$ pairs have to be produced via pairs of strange hadrons with higher production thresholds

2. the initial s and $\bar{s}$ survive the process of fireball expansion, thus resulting, at hadronization, in an unusually high yield of strange and multi-strange (anti)baryon abundance.

The process can be illustrated in figure 1.4.

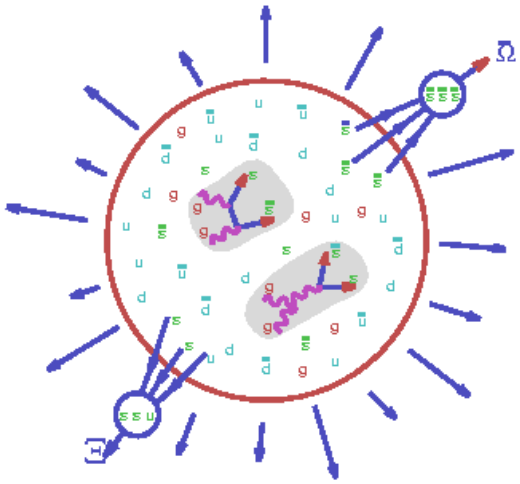

Fig. 1.4: Illustration of the two steps mechanism of strange hadron formation from QGP

In the ensuing hadronization, quark recombination leads to emergence of particles such as $\Xi(ssq)$ and $\bar{\Omega}(\bar{s}\bar{s}\bar{s})$, which otherwise could only very rarely be produced [1], as well as to a global increase of the strange particles production.

The described enhancement as a function of the centrality of collision has been already observed [2] in experiments such as NA57 at SPS, as it is clearly shown in figure 1.5.

It is trivial to stress the importance of measuring strange production even in pA and pp collisions, as the enhancement can be noticed only in comparison with such data.

Hard and electromagnetic probes of deconfinement

In order to be sensitive to the onset of deconfinement, any probe must satisfy some requirements, and in particular they must:

- be hard enough to resolve sub-hadronic scales;

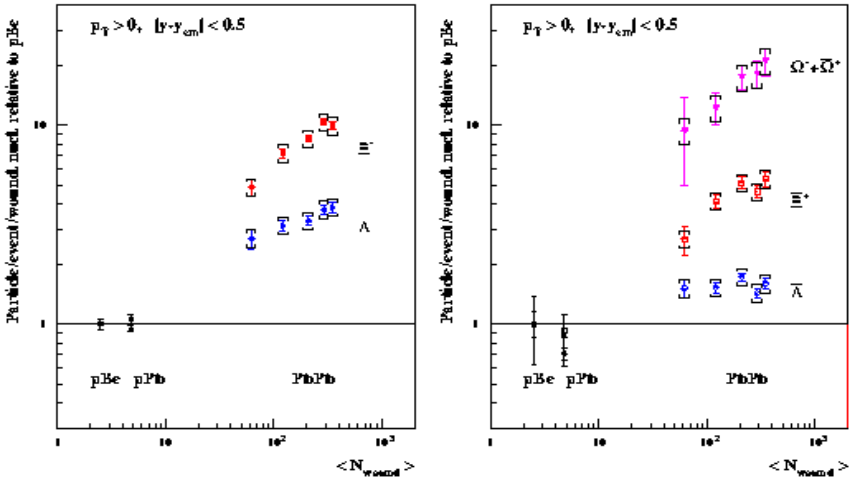

Fig. 1.5: Centrality dependence of hyperon enhancements at 158A GeV/c

- be able to distinguish confinement and deconfinement;
- be present in the early stage of the evolution;
- retain the information throughout the subsequent evolution.

The last point requires that probes should not be in thermal equilibrium with later evolution stages, since this would lead to a loss of memory of the previous stages.

So far, two types of probes satisfying these conditions fully or in part have been considered.

- *External* probes are produced essentially by primary collisions, before the existence of any medium. Their observed behavior can indicate whether the subsequent medium was deconfined or not. The most important observables are the production of quarkonium states and the energy loss or attenuation of hard jets.
- *Internal* probes are produced by the quark-gluon plasma itself. Since they must leave the medium without being affected by its subsequent states, they should undergo only weak or electromagnetic interactions after their formation. Thus the main candidates are thermal dileptons and photons.

Quarkonium suppression was long ago suggested as a signal of deconfinement [3]. If a heavy quark bound state ($Q\bar{Q}$) is placed into a hot medium of deconfined quarks and gluons, color screening will dissolve the binding, so that the Q and $\bar{Q}$ separate. When the medium cools down to the confinement transition point, they will therefore in general be too far apart to

see each other, and the heavy quark will combine with a light one to form heavy flavored mesons.

Due to their small size, quarkonia can, in principle, survive the deconfinement phase transition. However, because of color screening, no bound state can exist at temperatures $T > T_D$, when the screening radius, $1/\mu_D(T)$ becomes smaller than the typical bound-state size.

With increasing temperature, a hot medium will lead to successive quarkonium melting: bigger size resonances, such as χ_c and ψ' are dissolved first, while more tightly bound states, such as J/ψ, are destroyed later. Hence the suppression of specific quarkonium states serves as a thermometer of the medium.

In fact, a slight reduction in quarkonium production can be noticed even in ordinary nuclear matter, due to absorption by nucleons and comoving secondaries. In order to take into account this effects, it is of extreme importance to achieve a good knowledge of the quarkonia absorption cross section behavior from pA and pp data. Only when such a baseline is clearly understood, it is finally possible to search for "anomalous" suppression patterns, which are a clear signature of deconfinement.

Evidences of the phenomenon have been found by the NA50 experiment at CERN SPS [4], as shown in figure 1.6.

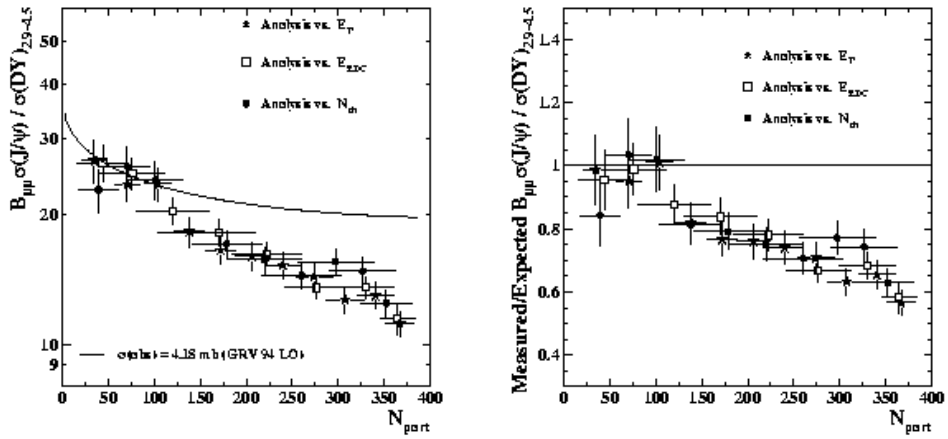

Fig. 1.6: The J/ψ/Drell-Yan cross section ratio as a function of N_{part} for three analyses of the $PbPb$ 2000 data sample in NA50, compared to (left) and divided by (right) the normal nuclear absorption pattern [4]

The LHC will add a significant contribution in the understanding of QGP via heavy quarkonia probes. The achievable energy is unique for suppression studies since it allows, for the first time, the spectroscopy of charmonium and bottomonium states in heavy ion collisions. In particular, because the Υ is expected to dissolve significantly above the critical temperature, the

spectroscopy of the Υ family at the LHC energies should reveal unique information on the characteristics of the QGP.

On the other hand, the study of heavy quark resonances in heavy ion collisions at the LHC is subject to significant differences with respect to lower energies. In addition to prompt charmonia produced directly via hard scattering, secondary charmonia can be produced from bottom decay, $D\bar{D}$ annihilation, and by coalescence mechanisms which could result in enhancement rather than suppression.

The role of jets as a deconfinement probe was first proposed in 1982 by Bjorken. He stressed that a "high-p_T quark or gluon might lose tens of GeV of its initial transverse momentum while plowing through quark-gluon plasma produced in its local environment". While Bjorken estimates based on collisional energy loss had to be revised, it was later suggested that the dominant energy-loss mechanism is radiative rather than collisional. In particular, the mechanism is not the direct analogous of the Abelian bremsstrahlung radiation, but a genuine non-Abelian effect: gluon rescattering.

A deeper insight into this topic is beyond the scope of the present thesis. However it has to be said that, since the partonic energy loss grows quadratically with the in-medium path length and is proportional to the gluon density, the observation of jet quenching in heavy ion collisions can be accounted as a proof of deconfinement.

It is clear that, in order to notice a "quenching", comparisons with jets in ordinary matter have to be performed. An important benchmark for fragmentation function of jets will be provided by analyses of pp collisions.

Hadronic probes are not the only ones able to give information on the formed medium. A lot of advantages can arise from the use of electromagnetic probes. Indeed, owing to their small coupling, photons, once produced, don't interact with the surrounding matter and can thus provide information on the state of matter at the time of their formation.

The production of photons in the different stages of heavy-ion collision can be summarized qualitatively as follows:

1. Early in the collisions, so-called "prompt" photons are produced by parton-parton scattering in the primary nucleus-nucleus collisions. An important background to such photons is the decay $\pi^0 \to \gamma\gamma$.

2. In the following stage of the collision, a quark-gluon plasma is expected to be formed with a temperature up to 1 GeV. Photons are radiated off the quarks which undergo collisions with other quarks and gluons in the thermal bath. The energy spectrum of these photons is exponentially suppressed, but should extend up to several GeV.

3. The plasma expands and cools. At the critical temperature, a hadronic phase is formed, during which photons can be produced in hadron rescattering or in resonance decays. The mechanism continues until the resonances cease to interact, that means until the freeze-out temperature ($\sim$ 100 MeV) is reached. Photons produced in this phase will have energies between few hundred MeV and several GeV.

4. Finally, after freeze-out, further photons can be produced by the decay of π^0's, η's and higher resonances. Their energy lies in the range of up to few hundred MeV.

The prompt photons of phase one constitutes an "irreducible" background to thermal photons of phase two and three. Such background has to be kept under control, for example via comparison to the *pp* benchmark. The occurrence of an excess in thermal photons (after background subtraction) in the few GeV range, would be a clear indication of a thermalized medium.

Lepton pair production shows analogies with the photon generation. In fact, they are emitted throughout the evolution of the system, and with the same stages described above.

The prompt contribution to the continuum in the dilepton mass range above pair mass $M \sim 2$ GeV is dominated by semileptonic decays of heavy flavor mesons and by the Drell-Yan process (figure 1.7). The latter was par-

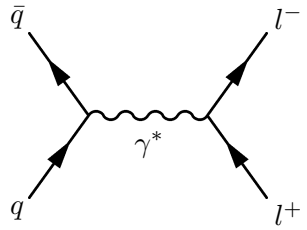

Fig. 1.7: Drell-Yan process

ticularly important in previous experiments, not as a deconfinement probe, but because it gives information on the initial state. Its prediction were usually adopted as a benchmark in heavy ion collisions, as it is affected only by ordinary nuclear matter effects, but it is not modified by the formation of a hot dense system. However, in the LHC, it is overwhelmed by heavy quark decays, which dominate the lepton pair continuum between the J/ψ and the Z^0 peaks.

Dileptons have the same functionality as photons in the different stages of the system evolution, but, in addition, they offer distinct advantages. In particular, lepton pairs carry an additional variable, the pair invariant mass, which encodes dynamical information on the vector excitations of matter.

At masses above $\sim$ 1.5 GeV thermal radiation is expected to originate from the early hot phases, with a rather structureless emission rate determined by perturbative $q\bar{q}$ annihilation. The physics objective is then similar to that of the photon case, which is the discrimination of the QGP radiation from the large prompt background.

At low masses, less than 1.5 GeV, thermal dilepton spectra are dominated by radiation from the hot hadronic phase. Here, the electromagnetic current is saturated by the light vector mesons (ρ, ω and ϕ), allowing direct access to their in-medium modifications

A schematic view of the characteristic dilepton sources in ultra-relativistic heavy ion collisions is shown in figure 1.8. The plot was obtained for center of mass energies lower than the LHC one, and it is shown here in order to get a rough idea of the dilepton mass distribution. As previously said, at high energies contributions from bottom flavored hadrons become important.

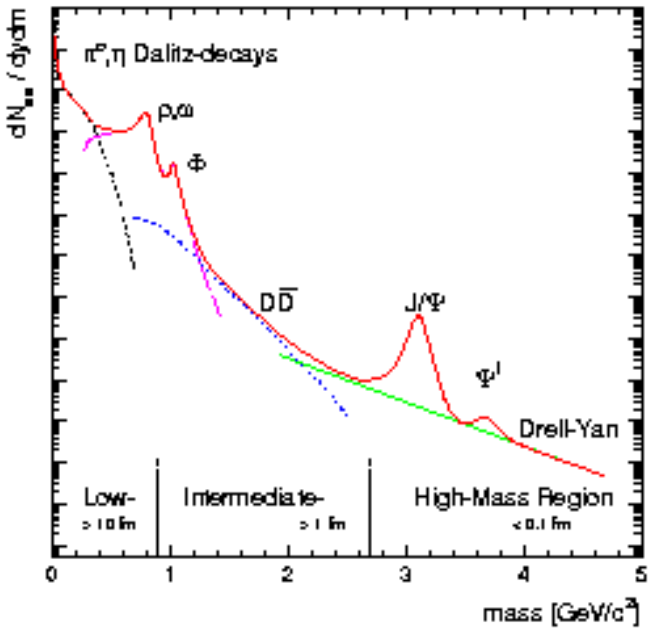

Fig. 1.8: Expected sources for dilepton production as a function of invariant mass in ultra-relativistic heavy ion collisions. The plot, obtained for lower energies than LHC is meant to give a rough idea of mass spectra in the low mass region. At higher energies contributions from bottom flavored hadron decays become important.

As in the case of photons, the determination of details of the medium effect relies on comparisons to smaller systems and to pp collisions.

1.2 Proton-proton (pp) collisions

ALICE has several features that make it an important contributor to proton-proton physics at the LHC. Its design allows particle identification over a broad momentum range, powerful tracking with good resolution from 100 MeV/c to 100 GeV/c, and excellent determination of secondary vertices. These, combined with a low material thickness and a low magnetic field, will provide unique information about low-p_T phenomena in pp collisions.

1.2.1 A benchmark for heavy ion physics

The identification of phenomena due to the formation of a new state of matter needs a good knowledge of ordinary nuclear matter effects, that can be achieved through comparison with pp collisions. A long list of observables have to be analyzed to this aim; some of them have already been presented in the previous section, but the overview will be completed in the following.

- Particle multiplicities: differences in particle multiplicities between pp and AA are related to the features of parton distributions in the nucleon with respect to those in nuclei (shadowing) and to the onset of saturation phenomena occurring at small x.
- Slopes of transverse mass distributions: the comparison of slopes in AA collisions with those in pp allows to determine the collective effects, such as transverse flow, present in AA and absent in pp.
- Particle yields and ratios: particle ratios are indicative of the chemical equilibration achieved in AA collisions and should be compared to those in pp collisions.
- Ratios of momentum spectra: the ratios of transverse momentum spectra at sufficiently high momenta allow to discriminate between the different partonic energy losses of quarks and gluons. In particular, due to their different color representation, hard gluons are expected to loose approximatively a factor of two more energy than hard quarks.

The dominant error for all these observables is often due to the systematics. In order to reduce it, it is thus of fundamental importance to measure the physical quantities in the same experimental setup, as it will be done in ALICE.

1.2.2 Specific aspects

In addiction to the benchmark role for $PbPb$ collisions, the study of pp physics in the ALICE experiment has an importance of its own. In particular, the characteristics of the LHC will allow the exploration of a new

range of energies and Bjorken-x values (chapter 6 of the present thesis is entirely dedicated to one aspect of this topic). More generally, the ALICE pp programme aims at studying non-perturbative strong coupling phenomena related to confinement and hadronic structure. The main contribution will be in the low transverse momentum domain for which the ALICE detector was optimized.

During pp collisions, ALICE efforts will be focused in the study of a large amount of observables, such as:

Particle multiplicity. Feynman predicted a simple scaling law for the $\sqrt{s}$ dependence of the observable, which was proved to be only approximate. Thus, a direct measurement is necessary, in order to get a better understanding of the phenomenon. Moreover the high statistics charged multiplicity study could allow to get access to the initial states, where new physics such as high-density effects and saturation phenomena sets in.

Particle spectra. The analysis will allow to study the minijet[1] contribution, by determining the hardening of p_T spectra and various correlations between particles with high p_T.

Strangeness production. The possibility to access considerably increased charged particle densities, together with a better control of the transverse momentum measurements, should allow ALICE to explain not well understood phenomena observed in previous experiments. One of these is the fact that correlation between the mean kaon transverse momentum and the charged particle multiplicity observed at the Tevatron is significantly stronger than that for pions.

Baryon number transfer in rapidity. The rapidity distribution of baryon number in hadronic collisions is not understood. A number of models provide explanation of the experimental data, some involving diquark exchange, some others adopting purely gluonic mechanism. The ALICE detector, with its particle identification capabilities, is ideally suited to clarify this issue with abundant baryon statistics in several channels in the central-rapidity region.

Correlations. Two-particle correlations have been traditionally studied in pp multiparticle production in order to gain insight into the dynamics of high energy collisions via a unified description of correlations and multiplicity.

[1] Jets whose E_T, though larger than the hadronic scale, is much smaller than the hadronic center of mass energy $\sqrt{s}$ (at the LHC it means $E_T \leq 10$ GeV). Such jets cannot be understood solely in terms of the fragmentation of partons of comparable E_T, produced in a hard subprocess. The minijets also receive a contribution from the dynamics of underlying events, which in nucleus-nucleus collisions have a substantial transverse activity.

Heavy flavor production. The low p_T cutoff for particle detection will require a smaller extrapolation of the total heavy flavor cross section, thus improving precision and clarifying underestimations of some theoretical models predictions.

Jet studies. Owing to its ability to identify particles and measure their properties in a very high density environment, the detector will be able to study jet fragmentation in a unique way.

Photon production. Although the production of photons at large transverse momentum has been extensively studied, no good agreement between experiment and theory has yet been achieved. The rate of production is essentially proportional to the gluon distribution in the proton, which can be probed directly by looking at the p_T dependence of the photon spectrum. ALICE will be able to measure prompt-photon production in a region where the not well known gluon fragmentation into photon is dominant, and where NLO calculations become insufficient, thus needing only recently explored theories.

Diffractive physics. Even in this case, new physical regions will be reached, because ALICE should be able to observe central-region events with large rapidity gaps as well as very low x phenomena (down to 10^{-6}). Investigation of the structure of the final hadronic state (with particle identification) produced in diffractive processes can provide important information on the mechanism of high energy hadronic interactions.

Double parton collisions. First measurements at Tevatron of double parton collisions show non-trivial correlations of the proton structure in transverse space, which indicate that the structure of the proton is much richer than the independent superposition of single-parton distribution functions accessible by deep-inelastic scattering. Since increasing the center of mass energy leads to an increase of the parton fluxes, it is clear that at LHC multiple-parton collisions will gain more and more importance, thus allowing a deeper study of the phenomenon.

Chapter 2

The ALICE experiment and the muon spectrometer

The ALICE experiment was first proposed as a central detector in the 1993 Letter of Intent (LoI), and later complemented by an additional forward muon spectrometer designed in 1995. It is a general-purpose heavy-ion experiment, sensitive to the majority of known observables (including hadrons, electrons, muons and photons). ALICE was designed in order to measure the flavor content and phase-space distribution, event by event, for a large number of particles whose momenta and masses are of the order of the typical energy scale involved (temperature $\sim \Lambda_{QCD} \sim 200$ MeV). The experiment will be able to cope with the highest particle multiplicities anticipated for $PbPb$ reactions ($\mathrm{d}N_{ch}/\mathrm{d}y = 8000$).

2.1 ALICE experiment: general overview

The ALICE detector (figure 2.1) has the typical aspect of detectors at colliders, with a cylindrical shape around the beam axis, but with in addition a forward muon spectrometer, detecting muons in a large pseudorapidity domain. Moreover, the central barrel angular acceptance is enhanced by detectors located at large rapidities, thus allowing measurements of low p_T particles and of global event structure. ALICE can be divided in three parts:

- the central part, which covers $\pm 45^\circ$ (corresponding to the pseudorapidity interval $|\eta| < 0.9$) over the full azimuth and is embedded in a large magnet with a weak solenoidal field. It consists (from the inside out) of
  - ◇ an Inner Tracking System (ITS)
  - ◇ a cylindrical Time Projection Chamber (TPC)
  - ◇ a Transition-Radiation Detector (TRD)

  - ◇ a large area Particle Identification (PID) array of Time Of Flight (TOF) counters
  - ◇ an electromagnetic calorimeter (PHOS)
  - ◇ an array of counters optimized for High-Momentum inclusive Particle Identification (HMPID)
- the forward detectors, constituted of
  - ◇ a Zero-Degree Calorimeter (ZDC)
  - ◇ a Forward Multiplicity Detector (FMD)
  - ◇ a Photon Multiplicity Detector (PMD)
- the Forward Muon Spectrometer (FMS)

Inner Tracking System (ITS). The main purposes of the ITS are the detection of the primary and secondary vertices (hyperons and charm) and the stand-alone track finding of low p_T charged particles, down to p_T of ~ 20 MeV/c for electrons. Moreover it can be used to improve the momentum resolution at high momenta, to reconstruct low energy particles and to identify them via energy loss, and, in the end, to define the angles of the tracks for HBT interferometry analysis.

The system consists of six cylindrical layers of coordinate-sensitive detectors. The granularity required for the innermost planes, given the expected high multiplicity of charged particle tracks, can only be achieved with silicon micro-pattern detectors with true two-dimensional readout, such as Silicon Pixel Detectors (SPDs) and Silicon Drift Detectors (SDDs). In particular silicon pixel detectors are used in the first two layers, silicon drift detectors in the third and forth layers, while in the fifth and sixth, where requirements in term of granularity are less stringent, strip detectors are adopted.

Time Projection Chamber (TPC). It is the main tracking detector of ALICE. Beyond track finding, it was specifically designed for momentum measurement and particle identification by $\mathrm{d}E/\mathrm{d}x$. The mean momentum of the particles tracked in the TPC is around 500 MeV/c. Despite being a comparatively slow detector, with about 90 μs drift time over the full length of 2.5 m, the time projection chamber can cope with the minimum-bias collision rate in $PbPb$ of about 8 kHz, expected for the design luminosity $\mathcal{L} = 10^{27}\, cm^{-2}s^{-1}$.

Transition-Radiation Detector (TRD). The TRD detector fills the radial space between the TPC and the TOF. It is constituted by a total of 540 detector modules, each consisting of a radiator and a multi-wire proportional readout chamber, together with its front-end electronic.

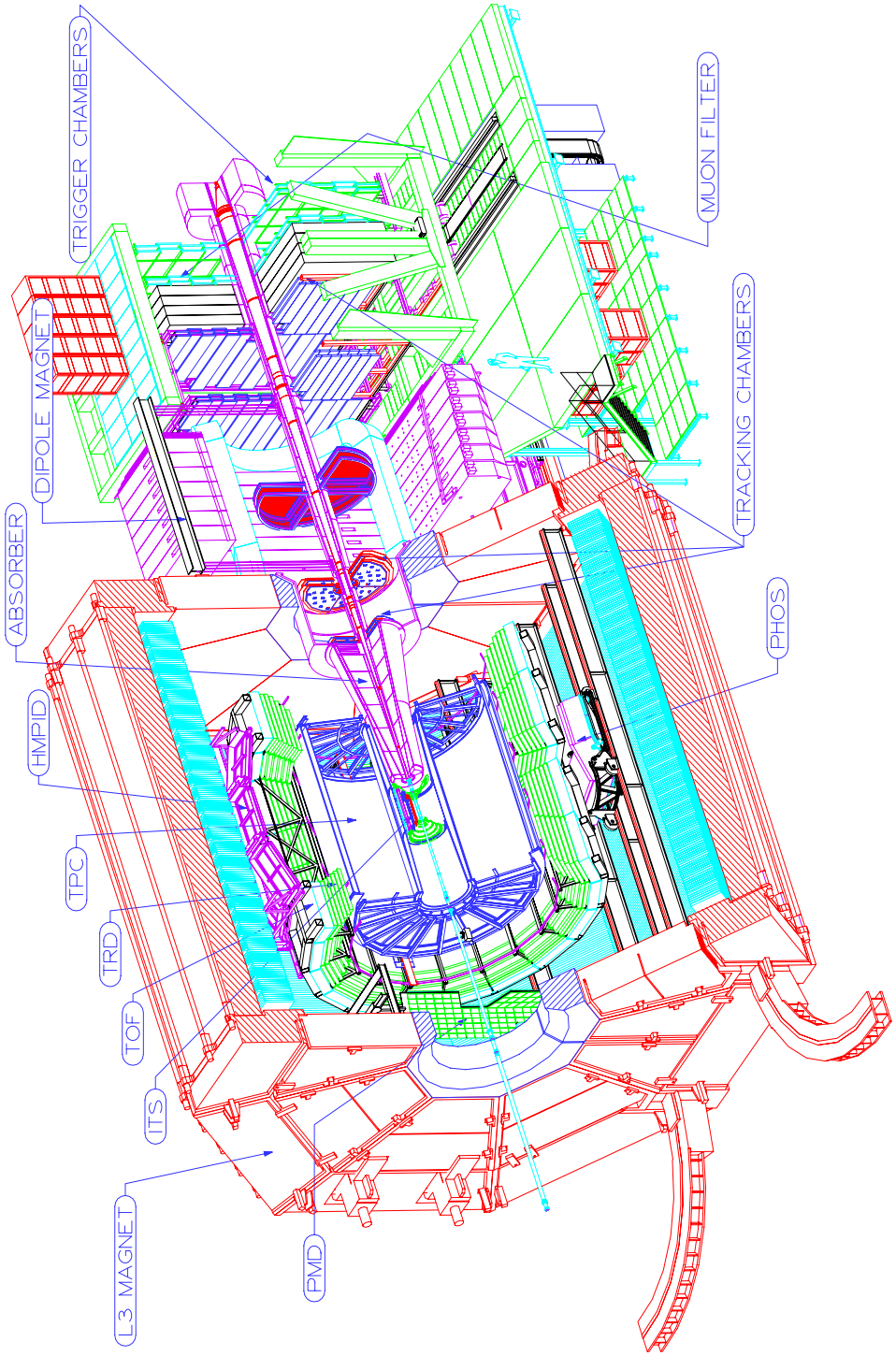

Fig. 2.1: The ALICE detector

The detector will provide electron identification for momenta greater than 1 GeV/c, where the pion rejection capability through energy-loss measurement in the TPC is no longer sufficient. Such identification, in conjunction with ITS, will be used in order to measure open charm and open beauty, as well as light and heavy vector mesons produced in the collisions. Moreover, the combined use of TRD and ITS data will allow to separate the directly produced J/ψ mesons from those coming from B decays.

Particle Identification (PID). Particle identification (PID) over a large part of the phase space and for many different particles is an important design feature of ALICE. There are two detector systems dedicated exclusively to PID: a *Time Of Flight* (TOF) and a small system specialized on higher momenta.

The time of flight is a Multi-Gap Resistive-Plate Chamber (MRPC), with a resolution better than 100 ps. It will be used to separate pions from kaons in the momentum range $0.5 < p < 2$ GeV/c, i.e. from the TPC upper limit for K/π separation through $\mathrm{d}E/\mathrm{d}x$, to the statistics limit in single event. In addition it will be able to distinguish between electrons and pions in the range $140 < p < 200$ MeV/c.

The High Momentum Particle Identification (HMPID) was specifically thought for hadron identification in the momentum region above 1.5-2 GeV/c. The dedicated detector was chosen to be a Ring Imaging Čherenkov (RICH), which provides a K/π and K/p separation up to 3.4 GeV/c and 5 Gev/c respectively.

Photon Spectrometer (PHOS). The PHOS is an electromagnetic calorimeter designed to search for direct photons, but it can also detect γ coming from π^0 and η decays at the highest momenta, where the momentum resolution is one order of magnitude better than for charged particles measured in the tracking detectors. The study of the high momentum particles spectrum is extremely useful because it gives information about the propagation of jets in the dense medium created during the collision ("jet quenching").

In addition to photons, the PHOS also responds to charged hadrons and to neutral particles such as K^0_L, n and $\bar{n}$. Some measures have to be taken in order to reject these particles, such as the inclusion of a charged-particle veto detector (multi wire proportional chambers were adopted) in front of the PHOS for charged hadrons, and a cut on the shower width and on the time of flight for neutral particles. The calorimeter is placed at 4.6 m from the beam axis, covers the pseudorapidity region $|\eta| \leq 0.12$ and has an area of 8 m^2.

Magnet. The last component of the central barrel is the magnet. The

optimal choice for the experiment is a large solenoid with a weak field. The choice of a weak and uniform solenoidal field together with continuous tracking in a TPC eases considerably the task of pattern recognition. The field strength of $\sim$ 0.5 T allows full tracking and particle identification down to $\sim$ 100 MeV/c in p_T. Lower momenta are covered by the inner tracking system. The magnet of the L3 experiment fulfills the requirements and, due to its large inner radius, can accommodate a single-arm electromagnetic calorimeter for prompt photon detection, which must be placed at a distance of $\sim$ 5 m from the vertex because of the particle density.

Zero-Degree Calorimeter (ZDC). The main aim of the ZDC is the estimate of the collision geometry through the measurement of the non-interacting beam nucleons (the "spectators"). There are four calorimeters, two for neutrons and two for protons, placed at 116 m from the interaction point, where distance between beam pipes ($\sim$8 cm) allows insertion of a detector. At this distance, spectator protons are spatially separated from neutrons from magnetic elements of the LHC beam line.

The neutron detector is made up of a tungsten alloy, while the proton one is constituted of brass. Both calorimeters have quartz fibers as the active material instead of the conventional scintillating ones.

Forward Multiplicity Detector (FMD). The purpose of the FMD is to measure $\mathrm{d}N/\mathrm{d}\eta$ in the rapidity region outside the central acceptance and to provide information for the trigger system in a very short time. The FMD is a silicon detector segmented into seven disks which surround the beam pipe at distances of between $\sim$ 42 and 225 cm from the vertex. Together they will cover the pseudorapidity range from -3.4 to -1.7 on the muon arm side and from 1.7 to 5.1 on the opposite hemisphere. It is designed in order to measure charged particle multiplicities from tens (in pp runs) to thousands ($PbPb$ runs) per unit of pseudorapidity.

Photon Multiplicity Detector (PMD). The PMD is a preshower detector that measures the multiplicity and spatial ($\eta - \varphi$) distribution of photons in order to provide estimates of the transverse electromagnetic energy and the reaction plane. It consists of two identical planes of proportional chambers with a $3X_0$ thick lead converter in between. It will be installed at 350 cm from the interaction point, on the opposite side of the muon spectrometer, covering the region $2.3 \leq \eta \leq 3.5$, in order to minimize the effect of upstream material such as the beam pipe and the structural component of TPC and ITS.

ALICE detector coordinate system

As a conclusion of the detector overview, the officially adopted coordinate system is provided. It is a right-handed orthogonal Cartesian system with the origin at the beam intersection point. The axis are defined as follows:

- x-axis is perpendicular to the mean beam direction, aligned with the local horizontal and pointing to the accelerator center;
- y-axis is perpendicular to the x-axis and to the mean beam direction, pointing upward;
- z-axis is parallel to the mean beam direction.

Hence the positive z-axis is pointing in the direction opposite to the muon spectrometer. The convention is coherent with other LHC experiments and has been changed from the one previously adopted in ALICE.

2.2 The muon spectrometer

The muon spectrometer (figure 2.2) was specifically designed in order to detect heavy quarkonia in the muon pairs decay channel. As the primary interest is on ψ (and Υ) resonances directly produced in the collision, it is important to measure J/ψ and ψ' at low p_T, where the contribution from charmonia coming from B mesons decay is lower.

Muon identification in the LHC environment is only feasible for muon momenta above ~ 4 GeV, because of the amount of absorber material required to reduce the flux of hadrons. Hence the important measurement of low p_T charmonium is possible only at small angles in the forward region, where the muons are Lorentz-boosted. Moreover, owing to the higher momenta of hadrons at forward rapidity and the corresponding lower decay probability, the background of decay muons is also reduced in the forward region. These are the reasons that led the design criteria of the detector.

The angular acceptance of the muon spectrometer goes from $2\,^\circ$ to $9\,^\circ$ ($2.5 < \eta < 4$)[1]. Its mass resolution (determined by angle and energy-loss fluctuations in the front absorber, multiple scattering in the tracking chambers, spatial resolution, number and position of the tracking planes, and the magnetic field integrals of the muon magnet) is better than 100 MeV at around 10 GeV, sufficient to separate all resonance states. The detector consists of a composite absorber starting 90 cm from the vertex, a large dipole magnet with 3 Tm field integral placed outside the L3 magnet, and 10

[1] In fact, in the ALICE coordinate system the muon spectrometer angular acceptance is $171\,^\circ < \vartheta < 178\,^\circ$, corresponding to a pseudorapidity of $-4 < \eta < -2.5$. However, in the analysis, for reasons of convenience, a polar coordinate system where the z-axis points toward the muon spectrometer will be adopted.

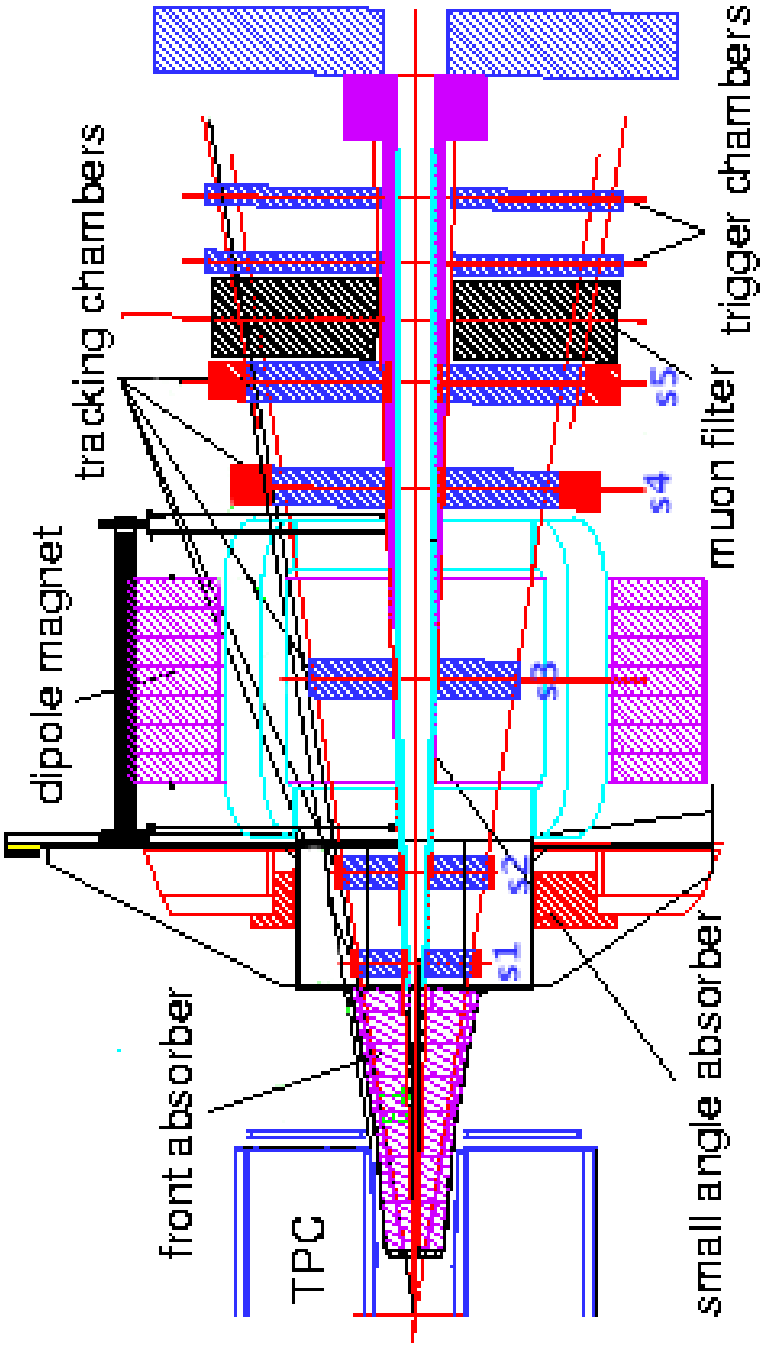

Fig. 2.2: The muon spectrometer

planes of thin, high-granularity tracking stations. The picture is completed by a second absorber, made of iron and acting as a muon filter, and four more detector planes, used for triggering. The spectrometer is shielded throughout its length by a dense absorber tube, of about 60 cm outer diameter, which surrounds the pipe.

Besides the heavy quarkonia detection, the ALICE spectrometer will provide a spectrum of the ϕ meson, and, in conjunction with TRD, will be able to study the heavy flavor production in the region $-2.5 < \eta < -1$, owing to the measurement of the $e - \mu$ coincidences.

2.2.1 Absorbers

The muon arm contains three absorber sections:

- the front absorber in the acceptance region ($\sim 10\,\lambda_{int}$)
- the beam shield surrounding the beam pipe
- the muon filter between the tracking and trigger chambers ($\sim 7.2\,\lambda_{int}$ of iron)

The front absorber (total length of 4.13 m) has the double task of attenuating the particle flux into the muon spectrometer by at least two orders of magnitude and of decreasing the muon background by limiting the free path for primary π, $K \to \mu$ decays. The minimal distance to the interaction point (90 cm) is imposed by the dimension of the inner tracker and the position of the multiplicity counters. The front section consists of dense low-Z materials to limit multiple scattering, while the rear one contains alternating layers of neutron moderator and absorber and high-Z material to shield against neutrons and photons. The use of a very dense material at the end of the absorber has an important consequence for the tracking. Since the multiple scattering in this layer is large, whereas the distance to the first tracking chamber is small, the muon production angle is best defined by combining the position measurement in the first chamber with the position of the interaction vertex, determined by the inner tracking system.

Outside the muon arm acceptance, a tungsten cone at $\vartheta < 2^\circ$ absorbs particles emanating from the beam pipe, and lead is employed at $\vartheta > 10^\circ$ to reduce the particle load in the TPC.

The small-angle beam shield consists of dense materials encased in a 4 cm thick stainless steel tube. Its outer envelope is "pencil shaped", i.e. it follows an angle of 2° until it reaches an outer radius of 30 cm and then stays constant up to the end of the spectrometer. The $r = 30$ cm prevents acceptance losses by taking into account the bending of tracks in the dipole field.

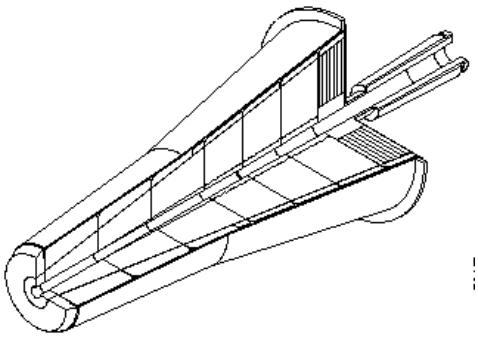

Fig. 2.3: Front absorber

The muon filter consists of a 5.6×5.6×1.2 m^3 iron wall, located at $z =$ 15 m between the last tracking and the first triggering plane. The hit rate in the trigger chambers is mainly due to surface emissions of soft particles from the beam shield and the backside of the muon filter.

2.2.2 Magnetic dipole

The size and bending strength of the muon spectrometer magnet are defined by the requirements on mass resolution and geometrical acceptance. The magnet has to cover the pseudorapidity range $2.5 < \eta < 4$, corresponding to an angular acceptance of $2\,^\circ < \vartheta < 9\,^\circ$.

Given the reduced requirements on size (a 5×6.6×8.6 m^3 box is enough to satisfy the angular coverage) and magnetic field ($B_{nom} \sim 0.7$ T), it is not necessary to use a superconducting magnet. It was therefore chosen a window-frame warm magnet (see figure 2.4) equipped with resistive coils and arranged so as to produce a magnetic field in the horizontal direction, along the x-axis (cf. section at page 20). With its integral magnetic field of 3 Tm, the dipole will be able to bend the muons along the y-axis and will allow a mass resolution better than 100 MeV, enough to separate the bottomonium states. The magnet will be placed directly adjacent to the ALICE L3 magnet.

2.2.3 Tracking chambers

The muon tracking system is composed of 5 stations, each consisting of 2 multi-wire chambers. Two of them are located in front of the muon magnet, two others behind and one in its center. Each chamber is read out by cathode planes in two orthogonal projections (X-Y) to provide two dimensional hit information. The two stations before and after the dipole magnet measure the corresponding track angles and the station located inside the magnet adds sagitta information. This layout provides redundant information and

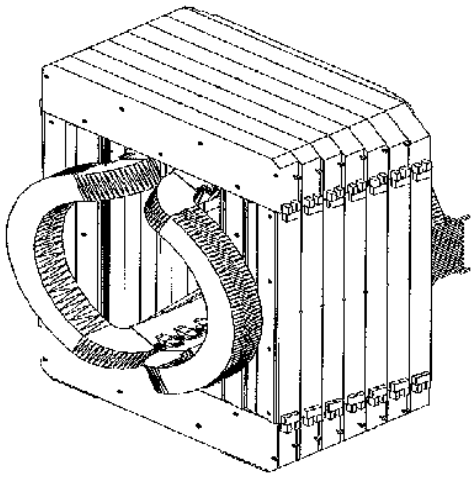

Fig. 2.4: General overview of the dipole magnet

can operate even if one of the ten station planes malfunctioned. The chambers are arranged in a projective geometry and are slightly larger than the acceptance of the spectrometer to account for bending in the magnetic field. The total sensitive surface is about 100 m^2.

In order to achieve a mass resolution of better than 100 MeV, the tracking chambers have to meet the following requirement:

- spatial resolution of $\lesssim 100\ \mu m$ to achieve a spatial momentum resolution of $\Delta p/p < 1\%$;
- resolution of $\sim$ 2 mm in the non-bending plane to reconstruct the angle of the muons and to allow an efficient pattern recognition;
- average material thickness of each sensitive plane of about $2 - 3\%$ of X_0;
- efficiently operativity at hit densities of up to $3{\times}10^{-2}$ cm^{-2}, as expected in the first station;
- low sensitivity to photon and neutron backgrounds.

Cathode Pad Chambers (CPC) and Cathode Strip Chambers (CSC) seem the best suited segmentation configurations for the muon arm. They, in fact, allow a fine segmentation of the cathode plane which, in addiction, can be continuously varied across the chamber area. The channel occupancy can thus be kept constant by adapting the pad or strip size to the local particle density.

Pads are used in the innermost (and hence with the highest particle density) region, while at large radii strips are adopted. The position resolution has been evaluated [8] with three different methods (center of gravity, ratio

of charges on adjacent pads and fit to charge distribution with a realistic function), giving a result of about 50 μm.

2.2.4 Trigger chambers

In central $PbPb$ collisions, about eight low-p_T muons from π and K decays are expected to be detected per event in the spectrometer. To reduce to an acceptable level the probability of triggering on events where these low-p_T muons are not accompanied by the high-p_T ones, emitted in the decay of heavy quarkonia (or in the semi-leptonic decay of open charm and beauty), a p_T cut has to be applied at the trigger level on each individual muon.

A dimuon trigger signal is issued when at least two tracks above a predefined p_T threshold are detected in an event. According to simulation results, a "low"-p_T cut (1 GeV/c) will be used for J/ψ and a "high" one (2 GeV/c) for Υ selection.

The trigger is performed by two trigger stations, each consisting of two single gap Resistive Plate Chamber (RPC), placed behind the muon filter. The RPCs match all the requirements concerning position resolution, fast response and low sensitivity to neutron and photon background.

Within ALICE, two trigger levels are foreseen for the muon spectrometer. A first level trigger (L0) rejects most of the low p_T muons, below the defined threshold (see above), which are essentially due to π and K decays. Some fast barrel detectors, like the pixel planes of the ITS, are read in coincidence. The decision to collect these events has to be available locally after a fixed latency of less than 1 μs in order to be distributed to the muon tracking chambers. This is achieved by using dedicated trigger electronics which work independently and in parallel to find muons candidates: two muons above a p_T threshold are required to give a L0 trigger signal.

The high level trigger (HLT) is more selective by sharpening the transverse momentum cut of the muon pairs. This trigger, carried out by online computer processing, will reduce the need in bandwidth and data storage by a factor of four to five.

The first level trigger is based on a transverse momentum cut in order to reduce the huge rate of low p_T muons from π and K decays. It requires a coincidence between the two trigger stations in which impact points must lie within a "road", whose width depends on the magnetic field and on the desired momentum threshold. Each hit in the first trigger station is combined with any hit inside a variable search area in the second station. Moreover, an approximate pointing toward the vertex is required in the non-bending plane, parallel to the field axis.

In practice such a p_T cut is performed approximately, knowing only the trigger chamber positions, in the bending plane, of the two stations. Given an x_1 value in the first station, a band in the second station can be deter-

mined according to the p_T limit considered. If the particle falls outside the region it is rejected (see figure 2.5).

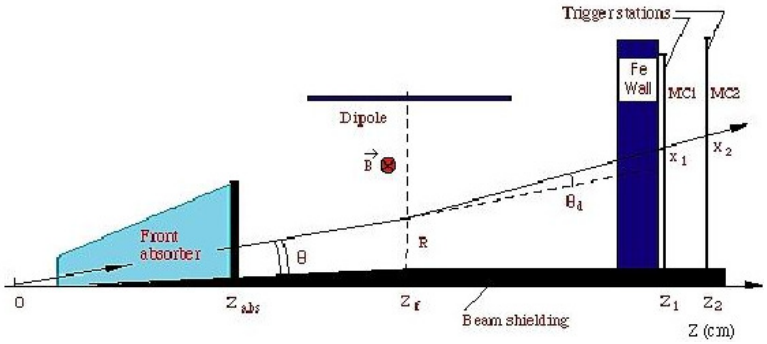

Fig. 2.5: Trigger method: projection in the bending plane

In the high level trigger, the muon p_T is calculated by using the information of the last two tracking chambers, just before the muon filter. In this way the accuracy in the lepton position measurement is enhanced, thus providing a better determination of the transverse momentum, and hence sharpening the p_T cut.

The two main sources of background in the trigger chambers are muons from particle decays and low-energy particles leaking out of the absorber and beam shield. In fact most of the soft background is due to electrons belonging to the latter category. The rest is from γ and neutrons interactions in the chamber material itself. These particles create random hits which are not correlated between the chamber planes. In addiction, the background is spread out in time on a μs time scale and can be partially rejected (the time interval that elapses between the detection of the fastest and the slowest muon is $\lesssim 5$ ns).

The RPCs are perfectly suited for background rejection and muons detection owing to their characteristics including

- fast response time (rise time ~ 2 ns);
- good time resolution ($\sigma_t \sim 1$ ns);
- high efficiency;
- spatial resolution $\lesssim 1$ cm (cf. [9]);
- neutron sensitivity of $\sim 3{\times}10^{-3}$ and $< 10^{-4}$ for 1 MeV and thermal neutrons respectively;
- gamma sensitivity $\leq 10^{-2}$;
- low cost and industrial production potential.

2.2.5 Track reconstruction

The muon arm was specifically designed to measure low p_T quarkonia with a mass resolution better than 100 MeV. The mass resolution is essentially determined by the precision reached in the measurement of the angle between the two muons and of their momenta. Unfortunately, behind the absorber the angular information is almost lost, because of the multiple scattering.

The reconstruction of the angle between the two muon tracks makes use of the event vertex, measured with high precision by the Si pixel layers of the ITS. Therefore, the angular precision is mainly determined by the lateral displacement of the muon tracks in the absorber and not so much by the scattering angle.

The momentum resolution depends on three main contributions: measurement precision of the tracking chambers, multiple scattering inside the tracking system and energy-loss fluctuations in the absorber. The relative importance of these contributions depends on the track momentum.

The tracking is initiated by a matching in the two nearby detection planes of each station. All hits of the second plane laying in a road defined by the vertex position and the hit position in the first plane, are kept to feed the track-finding algorithm. This one starts from the last two muon stations where hit densities are more favorable. Higher momentum tracks are processed first, as they have the smaller extrapolation errors form multiple scattering and from track curvature.

In a first step, vectors are extrapolated from Station 4 to Station 5 and conversely in order to initiate the track-finding procedure with a straight line behind the magnet. In a second step, tracks are extrapolated to the interaction point, through the magnetic field, and the nearest vector (or single hit) found in the neighboring tracking station is added to the track.

A track is validated if at least three hits (out of four possible) are found in the detector planes behind the dipole magnet and at least one hit (out of two) in the station located inside the magnet and in the chambers in front of the magnet.

The procedure stops when the next candidate has an estimated momentum of below 3 GeV/c, since such muons come essentially from background sources.

Chapter 3

Theoretical and experimental benchmarks

The ALICE experiment is the last of a series of attempts to investigate new states of matter.

Although the technological and physical problems encountered by different experiments are peculiar and always represent a new challenge for researchers, it is obviously important to take into account the previous investigations as milestones along an unexplored path.

The new results obtained at higher and higher energies can be used in order to opportunely tune or test existing theoretical models, or can give rise to new ones that better describe the physics of the new experimental conditions.

In the following chapter it will be presented an overview of the most used theoretical models whose aim is a description, as accurate as possible, of quarkonia production in hadronic collisions. Moreover some of the latest results obtained by the most recent experiments that investigated quarkonia production with a center of mass energy lower than the one obtainable in the LHC, will be shown.

3.1 Theoretical models

Differently from the QED theory, which is now well known and provides some of the most precise prediction ever, the QCD, though laying on solid basis, is still affected by technological difficulties in calculations, due to its $SU(3)$ color structure and to the elevated value of the coupling constant α_s. Hard processes are well described, but when energy involved approaches to the QCD scale (Λ_{QCD}), such as in hadronization or quarkonia formation processes, the perturbation theory cannot be applied and models are required.

In the case of the ALICE experiment, the situation is even more challenging, as the use of heavy ions generates non-trivial effects, both in the initial and in the final states, which have to be taken into account. Nevertheless, as this thesis is about proton proton collisions, it will be avoided an insight into this important topic, which is well discussed in other works (see for instance reference [13] for further details).

3.1.1 Color Singlet Model (CSM)

The color singlet model, which nowadays has an historical more than a practical relevance, was one of the first proposed, shortly after the discovery of the J/ψ. The initial applications were to η_c and χ_c production through two gluons fusion. Somewhat later, the CSM was applied to the production of J/ψ and η_c in B-meson decays and to the production of J/ψ plus a gluon through two gluons fusion and photon gluon fusion. However the model, though largely used in the past, is no more adopted in high energy experiments. In fact in 1995, experiments at the Tevatron showed that it under-predicts the cross section for prompt charmonium production in $p\bar{p}$ collisions by more than an order of magnitude [14].

The main concept of the CSM is that, in order to produce a quarkonium, a $Q\bar{Q}$ pair must be generated with the right quantum numbers. In particular the pair has to be produced in a color-singlet state. The model can be obtained by the NRQCD factorization formula of equation 3.2 by dropping all of the color-octet terms. However, in case of a P-wave state or a state of higher orbital angular momentum, the CSM leads to infrared divergences that cancel only when one includes color-octet terms. Thus, the CSM is theoretically inconsistent for quarkonium states with nonzero orbital angular momentum.

3.1.2 Color Evaporation Model (CEM)

The color evaporation model was first discussed at the end of the 70s [16]. The main idea of CEM is that the quarkonium production cross section is some fraction F_C of all $Q\bar{Q}$ pairs below the $H\bar{H}$ threshold, where H is the lowest mass heavy flavored hadron. Thus, the CEM cross section is simply the $Q\bar{Q}$ production cross section with a cut on the pair mass, but without any constraints on the color or spin of the final state. The produced $Q\bar{Q}$ pair then neutralizes its color by interaction with the collision-induced color field — hence the name "color evaporation". If the partonic center of mass energy ($\sqrt{\hat{s}}$) is less than the heavy hadron threshold ($2m_H$), the additional energy needed to produce heavy-flavored hadrons is obtained non-perturbatively from the color field in the interaction region. Thus the yield of all quarkonium states may be only a small fraction of the total $Q\bar{Q}$ cross section below $2m_H$.

At *leading order*, the production cross section of quarkonium state C in AB collision is:

$$\sigma_C^{CEM} = F_C \sum_{i,j} \int_{4m_Q^2}^{4m_H^2} \mathrm{d}\hat{s} \int \mathrm{d}x_1 \mathrm{d}x_2 \, f_{i/A}(x_1, \mu^2) f_{j/B}(x_2, \mu^2) \hat{\sigma}_{ij}(\hat{s}) \delta(\hat{s} - x_1 x_2 s) \tag{3.1}$$

where

- A and B can be any hadrons or nuclei
- $ij = q\bar{q}$ or gg
- $\hat{\sigma}_{ij}(\hat{s})$ is the $ij \to Q\bar{Q}$ subprocess cross section
- $f_{i/A}(x_1, \mu^2)$ is the parton density in hadron or nucleus (see sec. 6.1)

In order for the model to have predictive power, it is necessary that the fraction F_C is universal so that, once it is fixed by data, the quarkonium production ratios should be constant as a function of $\sqrt{s}$, y and p_T. The actual value of F_C depends on the heavy quark mass, m_Q, the scale, μ^2, the parton densities and the order of the calculation. It was shown [17] that the quarkonium production ratios were indeed constant, as expected by the model.

The leading order formula 3.1 is surely insufficient to describe high p_T quarkonium production since the $Q\bar{Q}$ pair p_T is zero at LO. Therefore the CEM was taken to NLO, thus including processes such as $gg \to gQ\bar{Q}$.

The determination of the fraction F_C for J/ψ and Υ production was done with different parton densities, quark masses and scales, summarized in table 3.1. The values are obtained as a fit to data from pp and pA collisions with a center of mass energy up to 63 GeV for charmonium states and up to 1.8 TeV for bottomonium states.

	Label	PDF	$m_c(GeV)$	μ/m_c	$F_{J/\psi}$
$c\bar{c}$	$\psi 1$	MRSTHO	1.2	2	0.0144
	$\psi 2$	MRSTHO	1.4	1	0.0248
	$\psi 3$	CTEQ5M	1.2	2	0.0155
	$\psi 4$	GRV98HO	1.3	1	0.0229
	Label	PDF	$m_b(GeV)$	μ/m_b	F_Υ
$b\bar{b}$	$\Upsilon 1$	MRSTHO	4.75	1	0.0276
	$\Upsilon 2$	MRSTHO	4.5	2	0.0201
	$\Upsilon 3$	MRSTHO	5.0	0.5	0.0508
	$\Upsilon 4$	GRV98HO	4.75	1	0.0225

Tab. 3.1: Parameters used to obtain the best agreement to the $Q\bar{Q}$ cross section

Some discrepancies can be noticed among the cross sections obtained with different parameter sets. In the case of Υ, as it can be seen in figure 3.1, the NLO CEM calculations that better reproduce data at high energies are the ones obtained with parameter sets $\Upsilon 1$ and $\Upsilon 2$ of table 3.1. Between the two, the better agreement is shown by the latter, whose predictions were therefore adopted in this thesis. The $b\bar{b}$ cross section obtained employing $\Upsilon 2$ parameters is a factor of almost 40% higher than the one obtainable with $\Upsilon 1$.

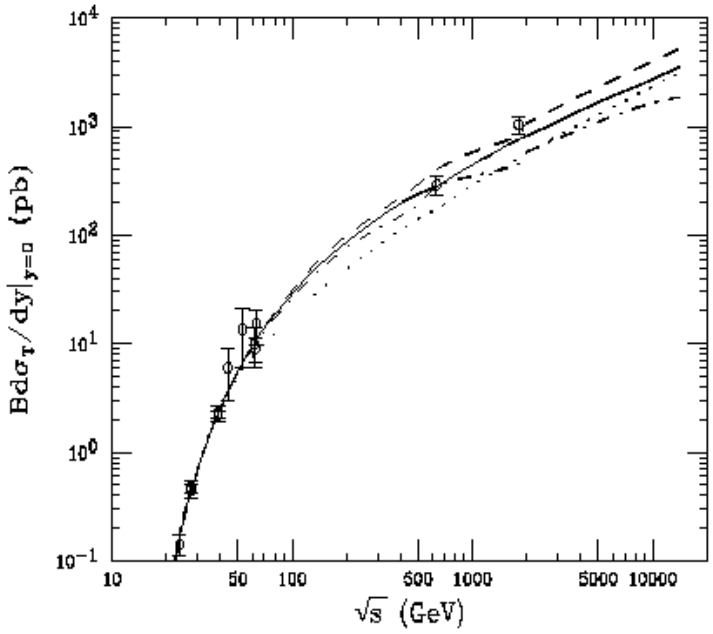

Fig. 3.1: Inclusive combined $\Upsilon + \Upsilon' + \Upsilon''$ production data compared to NLO CEM calculations. The results are obtained with parameter choices $\Upsilon 1$ (solid), $\Upsilon 2$ (dashed), $\Upsilon 3$ (dot-dashed) and $\Upsilon 4$ (dotted).

In the case of J/ψ the parameter sets $\psi 1$, $\psi 3$ and $\psi 4$ lead to similar values for the cross sections, while a 50% less is achieved with the $\psi 2$. As the adopted parameters for the bottomonium states are the ones obtained with the MRSTHO parton distribution functions, it was consistently decided to employ the corresponding sets for charmonium states, namely $\psi 1$ and $\psi 2$. Extrapolations to the recent CDF data at 1.96 TeV show that the $\psi 1$ predictions are closest to the experimental cross section, and was therefore employed in this thesis. It has to be said that, in any case, the CEM underestimate the total charmonium production at Tevatron by about a factor of two. Despite of this, it was nevertheless decided to adopt the

model predictions as a benchmark for the simulations, being aware that a scaling factor could be needed in order to fit the ALICE data.

The calculated cross sections for directly produced (i.e. without feed-down from higher resonances) quarkonia, and the inclusive ones multiplied by the branching ratio in muon pairs are summarized in table 3.2. The values reported will be used in section 5.2, when determining the heavy quarkonia detection in the ALICE muon spectrometer.

Quarkonium	σ^{dir} (μb)	$BR_{\mu\mu}\sigma^{inc}$ (μb)
J/ψ	32.9	3.18
ψ'	7.43	0.057
Υ	0.602	0.028
Υ'	0.378	0.0070
Υ''	0.224	0.0042

Tab. 3.2: Direct cross section for pp collisions at 14 TeV. The results are given for $\psi 1$ and $\Upsilon 2$. The cross sections showed will be adopted in the following simulation.

3.1.3 Non Relativistic QCD (NRQCD)

In both heavy-quarkonium decays and hard-scattering production, large energy-momentum scales appear. The heavy-quark mass m_Q is much larger than Λ_{QCD}, and, in the case of production, the transverse momentum p_T can be much larger than Λ_{QCD} as well. Thus the associated value of α_s are much less than one: $\alpha_s(m_c) \approx 0.25$ and $\alpha_s(m_b) \approx 0.18$. It is therefore possible to calculate the rates for heavy quarkonium production and decay rather accurately in perturbation theory. However there are clearly low-momentum, non-perturbative effects associated with the dynamics of the quarkonium bound state that invalidate the direct application of perturbation theory.

In order to make use of perturbative methods, one must first separate the *short-distance/high-momentum* perturbative effects from the *long-distance/low-momentum* non-perturbative effects — a process which is known as *factorization*. A convenient way to carry out this separation is through the use of the effective field theory Non-Relativistic QCD (NRQCD).

NRQCD consists of a non-relativistic Schrödinger field theory for the heavy quark and antiquark that is coupled to the usual relativistic field theory for light quarks and gluons [18]. The theory reproduces full QCD accurately at momentum scales of order $m_Q v$ and smaller, where v is the heavy-quark velocity in the center of mass of the bound state ($v^2 \approx 0.3$ for charmonium; $v^2 \approx 0.1$ for bottomonium).

$Q\bar{Q}$ production occurs at momentum scales of order m_Q or larger, thus

manifesting itself through contact interactions. As a result, the quarkonium production cross section can be written as a sum of the products of NRQCD matrix elements and short-distance coefficients:

$$\sigma(H) = \sum_n \sigma^{(Q\bar{Q})_n}(\Lambda)\langle 0|\mathcal{O}_n^H(\Lambda)|0\rangle \tag{3.2}$$

where:

- H is the quarkonium state
- Λ is the ultraviolet cutoff of the effective theory
- $\sigma^{(Q\bar{Q})_n}(\Lambda)$ are short-distance coefficients
- $\mathcal{O}_n^H$ are four-fermion operators
- n runs over all color and angular momentum states of the $Q\bar{Q}$ pair

The short-distance coefficients $\sigma^{(Q\bar{Q})_n}(\Lambda)$ are essentially the process-dependent partonic cross sections to make a $Q\bar{Q}$ pair, which can be produced in a color-singlet or a color-octet state. The vacuum matrix element of the four-fermion operator is the probability for a $Q\bar{Q}$ pair to form a quarkonium plus anything, thus being somewhat analogous to parton fragmentation functions. It contains all of the non-perturbative physics associated with the evolution of the $Q\bar{Q}$ pair into a quarkonium state.

Color-singlet model is obtained by dropping all color octet contributions in equation 3.2. In contrast, NRQCD is not a model, but a rigorous consequence of QCD in the limit $\Lambda_{QCD}/m_Q \to 0$. Moreover, the NRQCD matrix elements have the important property of being universal, i.e. process independent, which greatly increases the prediction power of the theory.

NRQCD was used in order to get predictions in the LHC energy range. The most important matrix elements for J/ψ = $\psi(1S)$ and ψ' = $\psi(2S)$ production can be reduced to the color-singlet parameter $\langle\mathcal{O}_1^{\psi(nS)}(^3S_1)\rangle$ and the three color octet parameters $\langle\mathcal{O}_8^{\psi(nS)}(^3S_1)\rangle$, $\langle\mathcal{O}_8^{\psi(nS)}(^1S_0)\rangle$ and $\langle\mathcal{O}_8^{\psi(nS)}(^3P_0)\rangle$.

In pp collisions, different partonic processes for $Q\bar{Q}$ production dominate in different p_T ranges. If p_T is of the order of m_Q, fusion processes dominate and so $Q\bar{Q}$ pair is produced in the hard-scattering process. These contributions can be written in the form

$$\sigma_{Fu}(H) = \sum_{i,j}\int \mathrm{d}x_1\mathrm{d}x_2 f_{i/p_1}(x_1,\mu^2) f_{j/p_2}(x_2,\mu^2)\hat{\sigma}_{ij}^{(Q\bar{Q})_n}\langle\mathcal{O}_n^H\rangle \tag{3.3}$$

where p_1 and p_2 are the incoming protons. The parton processes $ij \to Q\bar{Q}X$, where ij = gg, $q\bar{q}$, qg and $\bar{q}g$, and q = u, d, s, were included in NLO calculations.

For $p_T \gg m_Q$, the dominant partonic process is gluon fragmentation through the color octet $^3S_1$ channel. The contribution can be expressed as

$$\sigma_{Fr}(H) = \sum_{i,j} \int \mathrm{d}x_1 \mathrm{d}x_2 f_{i/p_1}(x_1, \mu^2) f_{j/p_2}(x_2, \mu^2) \hat{\sigma}_{ij}^g D_g^{(Q\bar{Q})_8(^3S_1)}(z, \mu_{Fr}^2) \langle \mathcal{O}_n^H \rangle \tag{3.4}$$

where $D_g^{(Q\bar{Q})_8(^3S_1)}(z, \mu_{Fr}^2)$ is the fragmentation function for a gluon fragmenting into a $Q\bar{Q}$ pair, P/z is the momentum of the fragmenting gluon, P is the momentum of the $Q\bar{Q}$ pair, and μ_{Fr} is the fragmentation scale.

In fact the fragmentation process, which scales as $\mathrm{d}\hat{\sigma}/\mathrm{d}p_T^2 \sim 1/p_T^4$, can be already included in the fusion process of equation 3.3. Nevertheless, in order to get a better accuracy at large p_T, equation 3.4 should be used instead of equation 3.3, which systematically overestimate the cross section in the high transverse momentum region.

The NRQCD shows a good agreement with experimental data with a center of mass energy up to 2 TeV. An explicative example of this assertion is shown in figure 3.2, where the predicted prompt p_T differential cross section for J/ψ production is compared with CDF data. Further discussions about this topic will be performed in section 3.2.1.

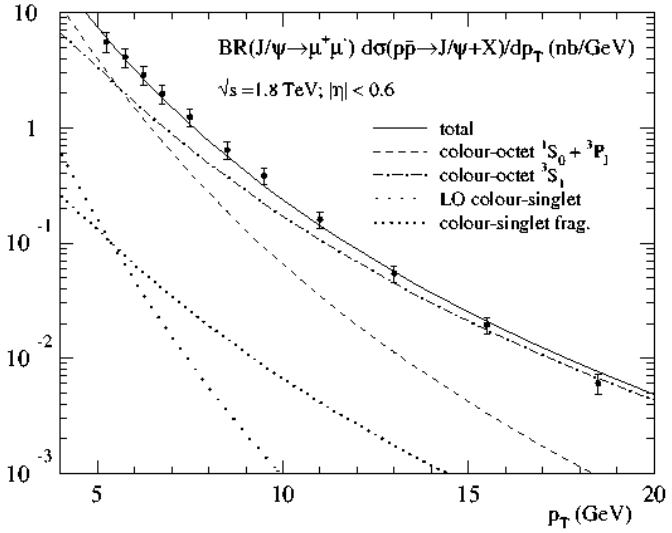

Fig. 3.2: J/ψ cross section as a function of p_T. The data points are from CDF measurement.

3.1.4 Comover Enhancement Scenario (CES)

The last model proposed in this chapter is the color enhancement scenario. Although its predictions will not be used in the following, it nevertheless

deserves to be cited in a section concerning the theoretical models at present adopted for the description of quarkonia production.

The CES was born from the analysis of agreements and discrepancies between the CSM and quarkonium data. Its main statement is that the hadroproduced $Q\bar{Q}$ pairs are created within a comoving color field and form quarkonia through *absorption* rather than emission of gluons. The cross section relative to the CSM is thus enhanced, since the pair gains rather than loses energy and momentum.

Such a mechanism is consistent with the success of CSM in mesons photoproduction, since no color fields are expected in the photon fragmentation region, $x \gtrsim 0.3$.

The origin of the comoving color field is illustrated in figure 3.3. Light charged particles carry gauge fields which are radiated in high energy annihilations into a heavy particle pair. In $e^+e^- \to \mu^+\mu^-$ reactions, the photon fields pass through each other and materialize as forward bremsstrahlung (figure 3.3(a)). In $gg \to Q\bar{Q}$ interactions, instead, the self-interaction of the color field allows the creation of a gluon field at midrapidities (figure 3.3(b)). This is not possible in direct meson photoproduction, because the incoming photon doesn't carry any color field (figure 3.3(c)).

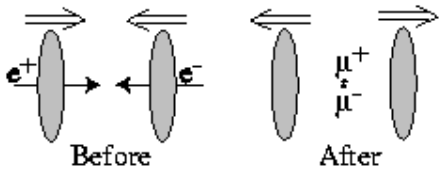

(a) QED ($e^+e^- \to \mu^+\mu^-$)

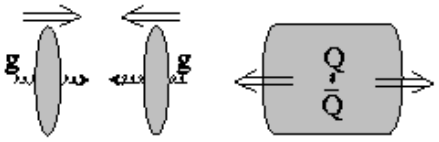

(b) QCD, hadroproduction ($gg \to Q\bar{Q}$)

(c) QCD, photoproduction ($\gamma g \to Q\bar{Q}$)

Fig. 3.3: Schematic scenario of gauge field interactions are compared

The CES distinguishes three proper timescales in quarkonium production:

- $\tau_Q \sim 1/m_Q$, the $Q\bar{Q}$ production time. The heavy quark pair is dominantly created in a color octet configuration, and has to get the quarkonium quantum numbers with further interaction.
- τ_{AP}, the DGLAP scale over which the comoving state is created and interacts with the $Q\bar{Q}$ pair. It is important to notice that $1/\tau_{AP}$ is an intermediate but still perturbative scale.
- $\tau_\Lambda \sim 1/\Lambda_{QCD}$, while rescattering with comoving spectators may occur. This phenomenon obviously concerns AA more than pp interactions.

The first time-scale considered is common to almost all models, but the fact that the $Q\bar{Q}$ pair acquires the quarkonium quantum numbers in a perturbative time-scale is a feature that distinguishes CES from other approaches.

3.2 Experimental data

Every new theory or model created must have a predictive power in order to be meaningful, and it is valid until its predictions aren't confuted by experiments. With the increase of the center of mass energy, the model statements could no longer apply, due to the fact that wider kinematic regions are explored, where the approximations adopted by the theory could no longer subsist, or to the presence of new physical phenomena, that never occurred before. In this case, if models still have free parameters, these can be suitably tuned in order to describe the new data, otherwise substantial modifications should be applied.

As already said, the LHC experiment will achieve energies never reached before and will have to rely on a number of theoretical models. It is thus important to understand the behavior of such models at Tevatron energies, in order to better understand their limits and potentialities.

Moreover results at lower energies are important on their own, as they can be directly compared with future experimental data with the purpose of getting evidences of eventual similarities or differences, due to possible new phenomena.

In the following, the latest results on heavy quarkonia production at the highest energies available, corresponding to the CDF data at ~ 2 TeV, will be summarized.

3.2.1 CDF results

The activity of the Collider Detector at Fermilab (CDF) began in the October of 1985. It is a general purpose experiment for the study of $p\bar{p}$ collisions at $\sqrt{s} = 1.8$ TeV, initially, and $\sqrt{s} = 1.96$ TeV, later, at the Tevatron collider. It operated with a luminosity up to $2{\times}10^{32}$ cm^{-2}s^{-1}, reached in the RunII (started in 2001).

Its main goals are:

- characterization of the properties of the top quark
- a global precision electroweak program, including the measurement of the W boson mass with a precision up to ± 40 MeV
- direct search for new phenomena, predicted by supersymmetry, technicolor and new $U(1)$ symmetries
- tests of perturbative QCD at the Next-to-Leading Order and large Q^2
- constraint of the CKM matrix with high statistics B decays (focusing, among the others, on $B^0 \to J/\psi\, K_S$ and $B_S \to J/\psi\, \phi$)

For further information on each topic see the CDF collaboration home page [19]. In the following, more details will be given about heavy mass quarkonia RunII results, which are strictly connected with the present work.

The study of the heavy flavored mesons was mainly focused on hadrons containing bottom quarks, as the primary aim was an analysis of mixing and oscillation phenomena. However, since the B mesons were above all detected in their J/ψ decay channel, a determination of the charmonium cross section was performable. In particular, owing to the silicon vertex detector, it was possible to disentangle the contribution of J/ψ directly produced in the collision or coming from decay of higher mass charmonia (prompt) from the ones coming from decay of B mesons. This separation is very important for our study because the ALICE detector won't be able to do the same, at least not for charmonia in the dimuon channel, detected in the forward spectrometer.

J/ψ's in the CDF experiment are detected through their decay in muon pairs. Differently from ALICE, the muon chambers are placed concentrically around the barrel, after the vertex detector, the central outer tracker and the electromagnetic and hadronic calorimeters, thus providing a pseudorapidity coverage of $|\eta| < 0.6$. The calorimeter acts as an absorber for the muon detector, which is therefore sensitive only to muons with $p_T > 1.35$ GeV/c. The simulated detector acceptance in p_T is shown in figure 3.4(a) while the corresponding in rapidity is shown in 3.4(b) [20]. Beyond statistical uncertainties, sources of systematic have to be studied, such as J/ψ spin alignment, p_T spectrum, muon chamber simulation and detector material description in GEANT simulations.

Data on charmonium are corrected for trigger and tracking efficiency and for acceptance, in order to get the inclusive J/ψ differential cross section, shown in figure 3.5.

In general, the inclusive cross section contains contributions from various sources, including decays of excited charmonium states and of b-hadrons.

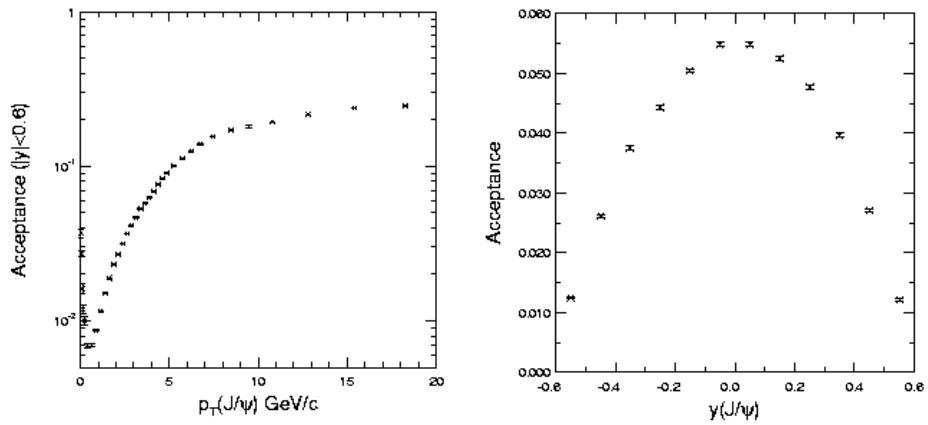

Fig. 3.4: Acceptance of J/$\psi \to \mu\mu$ events determined from a GEANT simulation of the CDF detector. The acceptance as a function of p_T is measured integrated over $|y| < 0.6$, while acceptance as a function of y is shown integrated over all p_T

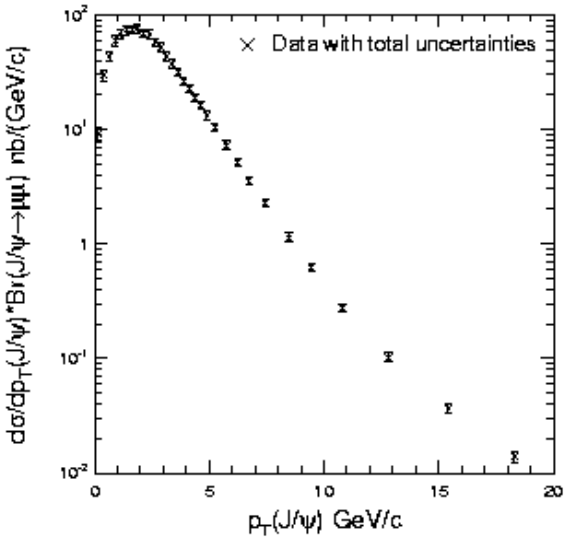

Fig. 3.5: Inclusive J/ψ cross section, dσ/dp_T $BR(J/\psi \to \mu\mu)$, as a function of p_T integrated over the rapidity range $|y| < 0.6$. The differential cross section include systematic and statistical uncertainties.

The charmonium states decay immediately. In contrast, the b-hadrons have long lifetimes that are of the order of picoseconds. This implies that J/ψ events from B decays are likely to be displaced from the beamline, and this fact can be exploited to separate their contribution from the others.

The fraction of such events as a function of p_T was measured for transverse momentum down to 1.25 GeV. The result is shown in figure 3.6.

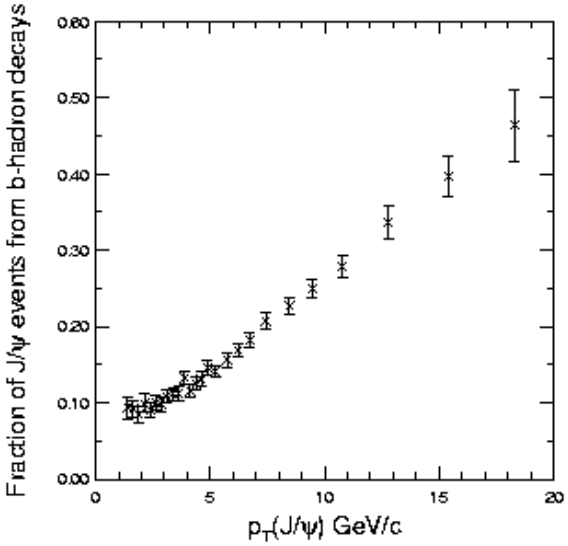

Fig. 3.6: Fraction of J/ψ from b-hadron decays in the inclusive J/ψ events of RunII data as a function of J/ψ transverse momentum. Error bars include both statistical and systematic errors.

It is finally possible to summarize the charmonium p_T differential cross section with a plot, where contribution from different J/ψ sources is shown (figure 3.7).

CDF data fit: NRQCD vs CEM

The NRQCD and CEM results described above can be used to analyze the inclusive heavy quarkonia production, given by the CDF experiment. The comparison was performed by exploiting a general property, which states that any model that can be described in terms of QCD processes at short distances, including the CEM, can be formulated in terms of assumptions about the matrix elements in the NRQCD factorization formula. Under determined assumptions (cf. reference [21]), it is thus possible to derive relationships among the NRQCD non-perturbative factors that follow from the model assumptions of the CEM and compare them with the phenomenological values of the NRQCD matrix elements themselves.

It is instead not worth applying the same study to the CSM, because the model can be excluded as a quantitative way to describe heavy-quarkonium production (see discussion in section 3.1.1).

In fact, even the color evaporation model shows some pronounced problems. The version in which the probability for the formation of a quarkonium

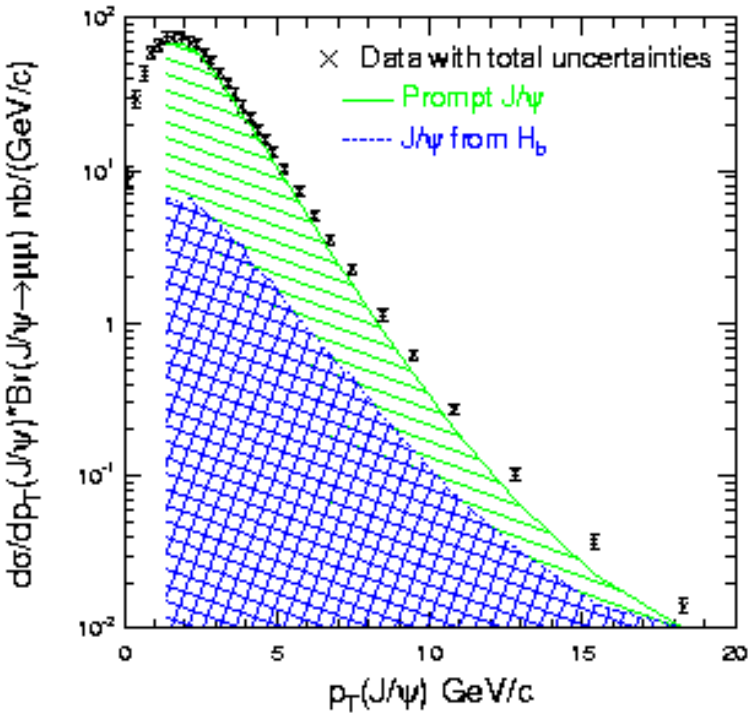

Fig. 3.7: Inclusive J/ψ cross section as a function of p_T integrated over the rapidity range $|y| < 0.6$. Contribution from prompt charmonium production and decays from b-hadrons is shown. In the error bars all uncertainties have been added.

is assumed to be independent of the spin state of the $Q\bar{Q}$ pair, can be ruled out on the basis of simple qualitative predictions. One of these is that the inclusive production rate of a quarkonium state should be independent of its spin state, so that it would always be produced unpolarized. This prediction is contradicted by observation of non-zero polarization of J/ψ's in e^+e^- annihilation at the B factories and by an analogous observation for the bottomonium states $\Upsilon(2S)$ and $\Upsilon(3S)$ in fixed-target experiments.

Moreover the model itself could be ruled out on the basis of the simple qualitative prediction that the ratio between the inclusive production rates for any pair of quarkonium states should be independent of the process. A violation in this sense comes from the fraction of J/ψ's produced from the decays of the P-wave charmonium states χ_{c1} and χ_{c2} (cf. [22]).

However, since the CEM is a model, it can be salvaged simply by declaring it to have a limited domain of applicability. The failure of the predictions for polarization can be avoided by declaring the model to apply only to cross section that are summed over the spin states of the quarkonium. In the case of the predictions that ratios of quarkonium cross sections should

be the same for all processes, the most dramatic failures can be avoided by declaring the model to apply only when the total hadronic energy is sufficiently large. This condition can be used to exclude applications to B decays.

Regarding the NRQCD, the theory is based on a factorization formula which is not at the level of rigor of some hard-scattering formulae, such as those for deep-inelastic scattering, Drell-Yan lepton-pair production and e^+e^- annihilation into hadrons. These last ones have actually been proved to hold at all orders in the strong coupling α_s. The existing all-orders proofs of factorization require that the observed scattered particles are produced at a large transverse momentum compared with the QCD scale Λ_{QCD} and that the cross sections is "sufficiently inclusive". With this expression it is meant that the variables in which the cross section is differential, cannot assume values that restrict final-state parton momenta, in the parton-level cross section, to be $\lesssim \Lambda_{QCD}$ of soft or collinear singularities.

CEM and NRQCD predictions about p_T differential cross sections in prompt J/ψ production were compared [21] to the CDF data. Results are shown in figures 3.8(a) and 3.8(b). Is it possible to notice that the NRQCD approach fits data much better than CEM.

In fact, the pure NLO calculations used for comparison have to be slightly modified. Some kind of smearing over k_T have to be introduced, in order to obtain a smooth transverse momentum distribution that can be compared with data. The physical origin of the smearing is the multiple gluon radiation from the initial and final state partons. A rigorous treatment of the effects of such emissions requires the resummation of logarithmic corrections to all orders in α_s. The k_T smearing is just a modelization of the phenomenon, in which the colliding partons are given gaussian distributions in the intrinsic transverse momentum, with a width $\langle k_T^2 \rangle$ that is treated as a phenomenological parameter.

The k_T smearing was introduced in the analysis, for both CEM and NRQCD (for purpose of comparison), with a value of $\langle k_T^2 \rangle = 2.5$ GeV^2, in order to obtain the best fit with the CDF J/ψ data. Results are shown in figures 3.8(c) and 3.8(d). The smearing substantially improves both the slope and normalization of the CEM fits to the data, and slightly worsens the NRQCD factorization ones. Nevertheless k_T smeared CEM fits are still considerably worse than the corresponding NRQCD fits.

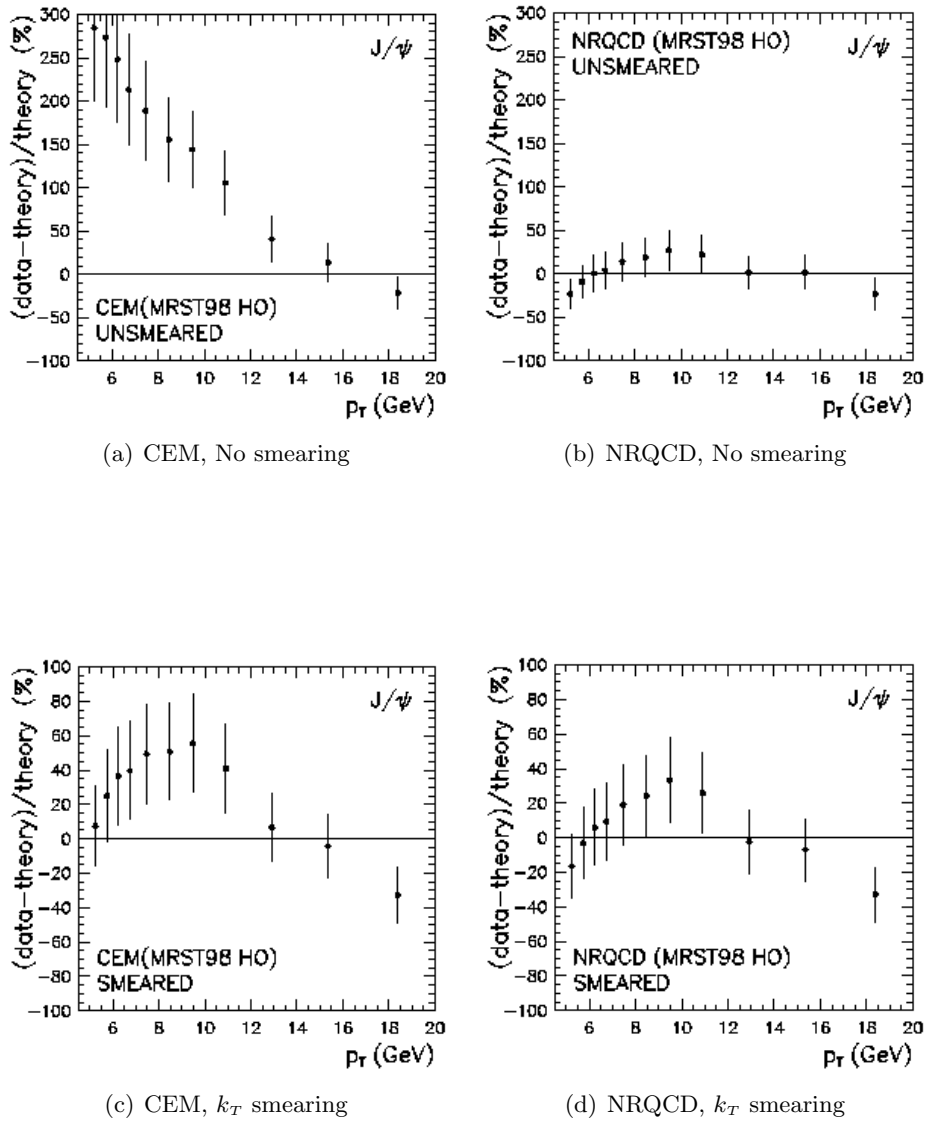

(a) CEM, No smearing

(b) NRQCD, No smearing

(c) CEM, k_T smearing

(d) NRQCD, k_T smearing

Fig. 3.8: J/ψ production: (data-theory)/theory. Comparison between CEM and NRQCD factorization predictions and CDF data.

Chapter 4

Fast simulations

The high luminosity and center of mass energy of LHC make it a high statistics "particle factory". The expected number of quarkonium (charmonium in particular) states detected in the muon spectrometer could be hardly produced and analyzed by full simulations in a reasonable amount of time. So a new kind of approach was adopted in heavy quarkonia production: the *fast simulation*.

The fast simulation is a technique based on the parameterization of the response of the muon spectrometer at the single muon level, which allows to considerably reduce the requested computational time. Given a muon of momentum p, generated at the interaction point at angles ϑ and φ, the fast simulation applies the smearing of the apparatus and gives the reconstructed p', ϑ' and φ', together with the detection probability P_{det} for that muon. This last term is the product of three factors, giving the probability for that muon to satisfy the acceptance (P_{acc}), reconstruction (P_{rec}) and trigger (P_{trig}) requirements.

In the following, some details will be given about the fast simulation implementation, starting from the parameterization of the detector response.

4.1 Fast reconstruction

The first step toward the fast simulation is the so called "fast reconstruction" of the muon track in the tracking system of the muon spectrometer. This procedure allows to skip the time consuming digitization and clusterization processes. Starting from a sample of muons coming from full simulations, the residual distributions are created and then parameterized by a superposition of two gaussians and a constant.

The residual is defined as $\Delta y = y_{cluster} - y_{hit}$, where $y_{cluster}$ is the impact point coordinate obtained with the cluster reconstruction, while the y_{hit} is the generated hit coordinate.

In the full simulation sample used, it is already taken into account the

presence of the background[1], whose effect is to add a flat component to the residual distribution, due to the double hits that are not resolved by the cluster finding algorithm.

Parameterizations obtained were applied to reconstruct the Υ and J/ψ invariant mass spectra for all of the background levels, with the proper p_T cuts (namely 1 GeV for J/ψ and 2 GeV for Υ). The process still needs the creation of hits, but the skipping of digitization and clusterization leads to a speed gain of 3 without background and 70 with nominal background.

4.2 The look up tables

The second step consists in the elimination of the hits creation phase. The objective is actually to directly smear the kinematic variables for each single muon, passing from generation to detector response without any intermediation.

In order to obtain this result it is first of all necessary to parameterize the experimental resolution on the kinematic variables of muons ($\Delta p = p_{rec} - p_{gen}$, $\Delta\vartheta = \vartheta_{rec} - \vartheta_{gen}$, $\Delta\varphi = \varphi_{rec} - \varphi_{gen}$), together with the acceptance and efficiency in several (p,ϑ,φ) intervals.

To this end, a number of positive, single muon tracks have been generated in the kinematic ranges:

- $0 < p < 200$ GeV/c
- $2\,^\circ < \vartheta < 9\,^\circ$ (i.e. detector acceptance)[2]
- $0\,^\circ < \varphi < 360\,^\circ$

each subdivided in 10 bins. In this way a 3-dimensional grid was defined, in which each cell covers 20 GeV/c in momentum, $0.7\,^\circ$ in ϑ and $36\,^\circ$ in φ. In fact the first bin of p and of ϑ has been further subdivided, in order to get a better description of this kinematic region, where the statistics is expected to be lower.

Reconstruction is then performed using the fast technique discussed above and parameter values for acceptance (P_{acc}, the "traceable track" condition), and reconstruction efficiency (P_{rec}) are stored in the *look up tables*. Muons in the geometrical acceptance range of the tracking chambers have been selected if they generated:

- at least 1 (out of 2) hits in each of the stations 1, 2 and 3;

[1] The background considered in the fast reconstruction is constituted by all particles except muons. In practice, it could be made of particles produced in the interaction with absorbers as well as of pions, kaons and electrons that manage in crossing (and hence leaving a track) in the muon spectrometer.

[2] See footnote page 20.

- at least 3 (out of 4) hits in the station 4 and 5 and in the trigger chambers.

The analysis of the Δp, $\Delta\vartheta$ and $\Delta\varphi$ distributions reveals interesting features. Unlike the other two, in fact, the first one is not symmetric, particularly in the lower bins of p. The shape is due to fluctuations in the energy losses, caused by interactions with the absorber. Such interactions, with a large energy transfer, especially through bremsstrahlung, generate an asymmetric function, with a Landau tail for high energy losses. Beyond radiative interactions, other contributions to the shape are given by losses in the cathode planes and to the detector resolution (resulting in a gaussian smearing).

The results of the distribution interpolations lead to the determination of the reconstruction smearing parameters, which are finally stored in the look up tables.

The calculations have been performed with different background levels: no background, half and nominal background. The latter consists in the simulation output of 5% most central $PbPb$ collisions at $2.7 + 2.7\,A$ TeV, with in addition a safety factor of two.

The negative muons were treated using the same parameters and applying the transformation $\varphi \rightarrow -\varphi$. For momenta above 200 GeV/c the parameters have been extrapolated.

The trigger probability has been evaluated after the factorization of the detector acceptance. The spectrometer phase space has been divided into 20×10 cells in the range

- $\diamond\ -90\,^\circ \leq \varphi \leq 90\,^\circ$
- $\diamond\ 2\,^\circ \leq \vartheta \leq 9\,^\circ$

As already said, the low and high trigger p_T cuts correspond to a mean transverse momentum of 1 and 2 GeV/c, used for J/ψ and Υ selection respectively. Due to the granularity of the trigger detector and to the trigger algorithm, the p_T cut is not sharp: the trigger probability has been studied as a function of the transverse momentum in the range $0 \leq p_T \leq 10$ GeV/c. The trigger response, P_{trig}, for single μ^+ has been computed while the response to negative muons was obtained with symmetry arguments (as well as the trigger probability for muons generated in the other half plane). Results are finally stored in the look up tables.

4.3 Fast simulation and physics performance

The analysis involving fast simulations are two steps processes. First of all it is necessary to generate particles. A number of different tools can

be adopted, but the important thing is that only the kinematics of the considered particles and of the muon pair that they produce have to be created. The operation can be even performed by using parameterizations of kinematic variables (such as transverse momentum and rapidity).

Once the dimuons are produced, they can be singularly analyzed, via fast simulation. The procedure consists in getting the p, ϑ and φ parameters for each muon, searching for the corresponding phase space cell in the look up table and determining the tabulated values for the detector acceptance (P_{acc}), tracking efficiency (P_{rec}), trigger efficiency (P_{trig}) and resolution. The latter parameters are employed to extract the reconstructed kinematic values (p', ϑ' and φ').

Such variables are then used to come back to the parent particle properties (such as mass, p_T or rapidity) and the so obtained values can be employed to fill histograms. Every single entry of the histogram has to be weighted with the detection probability of the muon pair, given by:

$$P_{det} = P^+_{acc}\, P^+_{rec}\, P^+_{trig}\, P^-_{acc}\, P^-_{rec}\, P^-_{trig}$$

where the apex + or - refers tho the sign of the muon considered.

Calculations show that the tracking efficiency is about $84 \div 92\%$ for J/ψ and $91 \div 97\%$ for Υ, while the trigger efficiency assumes a value of $\sim 75\%$ for J/ψ and of $\sim 95\%$ for Υ.

4.4 Comparison with the full simulation

Comparison with full simulation shows a very good agreement in the region of $p > 8$ GeV, but some discrepancies are present at very low momenta. The phase space portion with $p < 8$ GeV is quite peculiar, showing steep variations due to the fast rise of acceptance and efficiency.

In any case, the total number of accepted muons is about the same for full and fast simulation even in the problematic region. In the end the fast simulation allows a speed gain of about 30 with respect to full simulation without background and up to 10^3 with nominal background.

Chapter 5

Muon spectrometer physics performance

The main aim of the present thesis is the analysis of the muon spectrometer behavior for the study of heavy quarkonia production in proton-proton collisions with a center of mass energy of 14 TeV.
The study has two main purposes:

- it will provide a baseline for nuclear matter effects in pA or very peripheral AA collisions
- it has an intrinsic interest as quarkonia distributions (in particular p_T distributions) can investigate aspects of NLO perturbative QCD.

5.1 Input parameterizations

The whole analysis was performed with the fast simulation. The quarkonia were not produced with a particle generator tool, but using parameterizations of transverse momentum and rapidity distributions. Successively, the decay in a muon pair is forced, with the PYTHIA[1] decayer tool, and the kinematic variables of the leptons produced are analyzed through fast simulation.

It was chosen to adopt the color evaporation model predictions for rapidity differential cross sections. The calculations [17] were performed employing MRST NLO PDF set (see 6.2.2) and with NLO elementary cross sections for $Q\bar{Q}$ production by Mangano, Nason and Ridolfi [24] (cf. section 3.1.2). Figures 5.1(a) and 5.1(b) show the parameterizations obtained for prompt (i.e. directly produced in the collision) charmonium and bottomonium states respectively.

[1] PYTHIA is a Monte Carlo tool for particle generation. The version used is the 6.214, which is the one of the commonly used version in the ALICE collaboration.

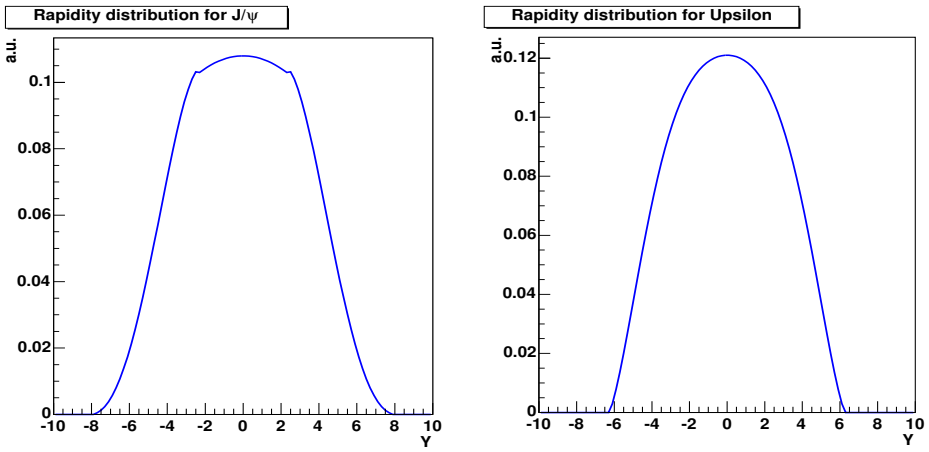

(a) charmonium (b) bottomonium

Fig. 5.1: Parameterization of rapidity distributions given by color evaporation model, adopted as input for fast simulation

Color evaporation model also gives predictions for transverse momentum distributions. However, when it is possible, it's always better to start from experimental data rather than from models. As data from CDF are available, it was decided to scale the results for $p\bar{p}$ collisions at 1.96 TeV in the center of mass [20] to LHC energies.

The operation consists of two steps. First of all it is necessary to fit the experimental data with a suitable function, which was chosen to be

$$f(p_T) = c\frac{p_T}{\left[1+\left(\frac{p_T}{A}\right)^2\right]^n} \tag{5.1}$$

where c, A and n are free parameters. Fit results are summarized in table 5.1. The second step consists in scaling the parameters in order to

Parameter	Energy (TeV)	J/ψ	Υ
c	all	75.14	66.18
n	all	3.821	3.051
A	1.96	4.025	6.49
	14	5.355	8.610

Tab. 5.1: Function parameters for p_T distribution at 1.96 TeV (CDF data fit) and at 14 TeV (fast simulation input)

obtain the p_T distribution at LHC energies. It was predicted (cf. [25]) that while passing from a lower energy to an higher one, the root mean square of the p_T distribution, $\langle p_T^2 \rangle$, increases with the trend shown in figure 5.2.

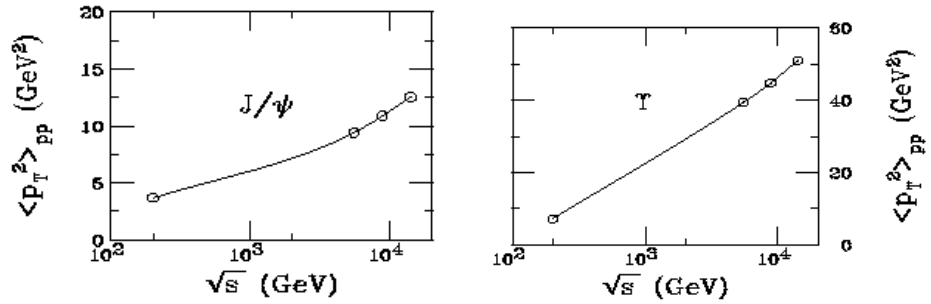

Fig. 5.2: Energy dependence of $\langle p_T^2 \rangle_{pp}$ for J/ψ (left) and Υ production assuming $\langle k_T^2 \rangle_{pp} = 1$ GeV^2. The open circles are the calculated energies at $\sqrt{s} = 0.2$, 5.5, 8, 8 and 14 TeV, interpolated by the solid line.

From calculation[2] we get:

$$\langle p_T^2 \rangle = \frac{\int_0^\infty \mathrm{d}p_T p_T^2 f(p_T)}{\int_0^\infty \mathrm{d}p_T f(p_T)} = \frac{A^2}{n-2}$$

where $f(p_T)$ is the fit function of equation 5.1. The scaling can be done by keeping the parameter n constant and suitably changing the value of A such that

$$A(14\mathrm{TeV}) = \sqrt{\frac{\langle p_T^2(14\mathrm{TeV}) \rangle}{\langle p_T^2(1.96\mathrm{TeV}) \rangle}}\, A(1.96\mathrm{TeV})$$

From figure 5.2 it can be seen that $\langle p_T^2 \rangle$ varies of about 77% for both J/ψ and Υ while passing from CDF to LHC energies, thus leading to a corresponding increase of about 33% in the parameter A. The final results are summarized in table 5.1 and shown in figures 5.3(a) and 5.3(b).

5.2 Simulation and analysis

5.2.1 Pure signal

The first part of the study is focused on the analysis of the pure signal, consisting in opposite sign muons coming from heavy quarkonia decay. Although the simulation of an experiment cannot leave the background out of consideration, it is nonetheless important to know in a proper way all the features of the signal.

Moreover in all of the ALICE simulations the signal and the background are produced separately and then properly merged together. In full simulations this is done because it would be too time consuming to generate

[2]The result holds only if $n > 2$, otherwise the numerator of the expression diverges for $p_T \to \infty$. In our case $n > 3$.

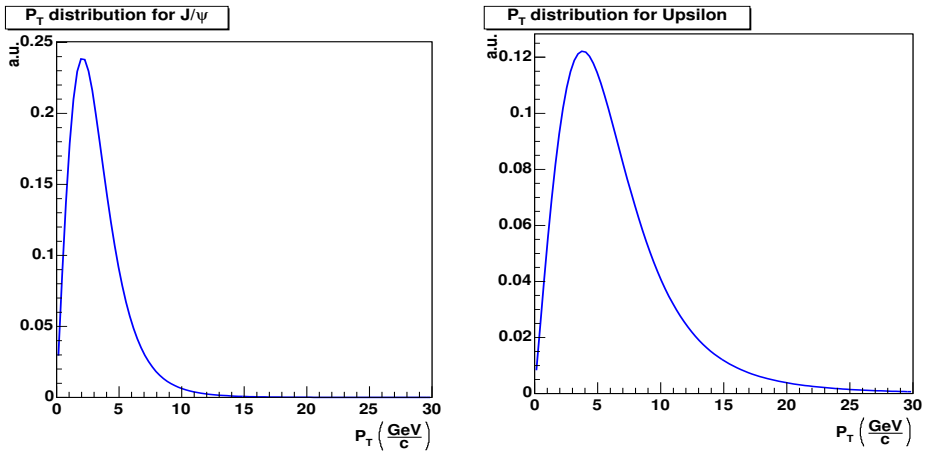

(a) charmonium (b) bottomonium

Fig. 5.3: Parameterization of p_T distributions scaled from CDF data, adopted as input for fast simulation. The area of the distribution is normalized to 1.

both processes at the same time, and it would be thus impossible to reach the expected statistics in a reasonable time. In fast simulations the reason of the separation is even deeper. As already said, particles are generated through parameterizations. We have predictions and hence transverse momentum and rapidity distributions for prompt (i.e. directly produced in a pp collision) heavy quarkonia, but there are no analogous predictions for background. Thus in fast simulations signal and background are handled separately from each other because they are generated in a different way.

The expected number of produced quarkonia, obtained from the input parameterizations described above, is given by the formula

$$N = \sigma \mathcal{L} t \tag{5.2}$$

where σ is the quarkonia cross section, $\mathcal{L}$ is the luminosity and t is the acquisition time. In fact we are interested only in resonances decaying in muon pairs, so it is convenient to generate only a number of particles

$$N = BR_{\mu\mu} \sigma \mathcal{L} t$$

and then to force the decay in muon pairs ($BR_{\mu\mu}$ is the branching ratio of the process). This is a common method to limit computational time and amount of stored data. Simulation parameters for prompt quarkonia are summarized in table 5.2.

After generation, muons produced by input quarkonia are processed by the fast simulation. A weight, corresponding to the detection probability

Parameters	
$\sqrt{s}$ (TeV)	14
Luminosity ($cm^{-2}s^{-1}$)	5×10^{30}
Time (s)	10^7
$\sigma_{c\bar{c}}$ (mb)	11.2
$\sigma_{b\bar{b}}$ (mb)	0.51

Quarkonia	$BR_{\mu\mu}\sigma^{prompt}$ (μb)	Number
J/ψ	3.18	1.59×10^8
ψ'	0.057	2.85×10^6
Υ	0.028	1.4×10^6
Υ'	0.0070	3.5×10^5
Υ''	0.0042	2.1×10^5

Tab. 5.2: Simulation parameters

P_{det} (see chapter 4), is assigned to each lepton. As already said the fast simulation takes into account the detector reconstruction performance by introducing a smearing in the angle ϑ between the muon direction and the beam axis, in the momentum p and in the azimuthal angle φ. From the reconstructed pair is then possible to go back to the heavy quarkonium, whose kinematic parameters can be used to determine the p_T, rapidity (y) or mass distributions. The results of the operation are the so called *raw yields*, corresponding to the expected number of quarkonia per p_T and y bin after one year (10^7 s) of data taking in pp collisions at 14 TeV, with the luminosity shown in table 5.2.

The p_T and rapidity yields for bottomonium states are shown in figure 5.4 and 5.5 respectively.

The case for charmonium states (ψ) is more complex. Besides the ψ directly produced in the collisions it is necessary to include the ψ coming from the decay of B mesons. Unfortunately the color evaporation model doesn't give predictions on them, so the only solution is to leave the "fast" production through parameterizations for the "slow" one, which uses PYTHIA predictions (cf. [26]).

The B mesons used are the same employed for correlated background (see section 5.2.2). The decay into ψ resonances was forced in order to increase statistics. The B mesons distribution is normalized such that the total $b\bar{b}$ cross section is equal to 1. Each ψ created is weighted with the proper branching ratio of the B particle that produced it, and the same happens for muons. The latter are analyzed through the fast simulation, which adds a further weight, taking into account the detector reconstruction probability.

It is then sufficient to scale the distribution by a factor of $\sigma_{b\bar{b}}\mathcal{L}t$, i.e. to the expected number of $b\bar{b}$ with the considered data taking conditions (table 5.2), in order to get the raw yields. The number of charmonium states obtained is about the 20% of the total.

Finally, the raw yields for prompt and from B decay ψ states are summed together giving the results shown in figure 5.6 and 5.7.

The use of the obtained raw yields, together with the knowledge of the

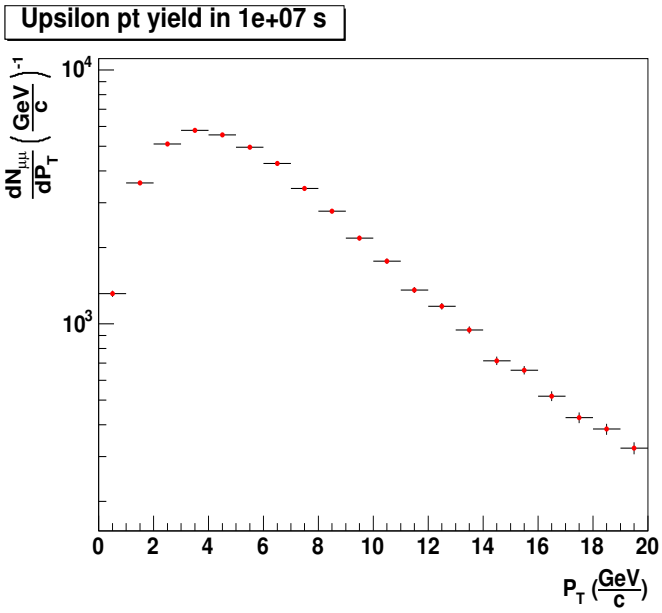

(a) Υ

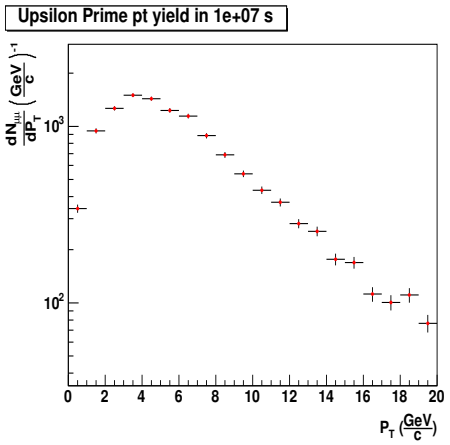

(b) Υ'

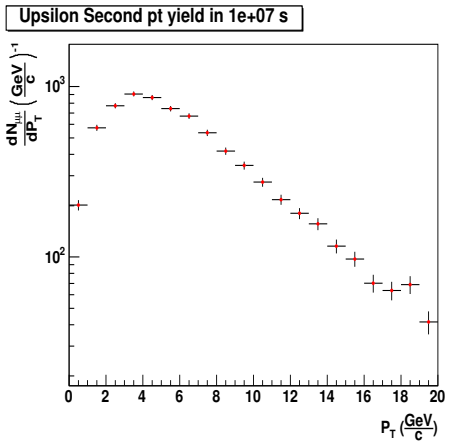

(c) Υ''

Fig. 5.4: p_T raw yields for bottomonium states in 10^7 s of data taking

input distributions, allow to determine the detection probability, which is a convolution of the geometrical acceptance and the trigger and tracking reconstruction efficiency. A general overview of the way to get the detection probability as a function of some observables (such as transverse momentum and rapidity) is given in appendix C. The results of simulation are shown in figure 5.8 and 5.9 for charmonium and bottomonium states respectively.

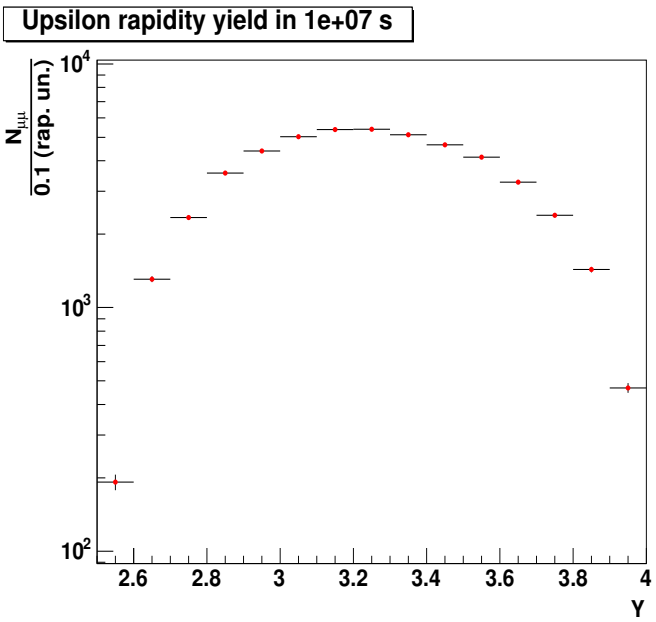

(a) Υ

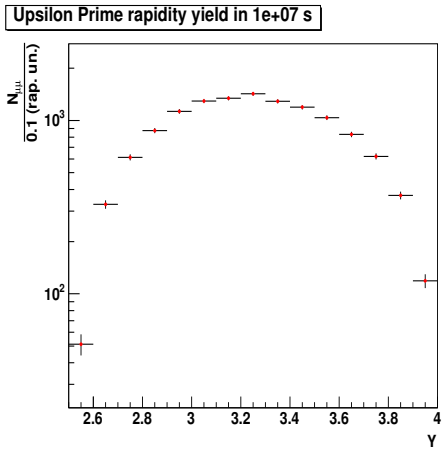

(b) Υ'

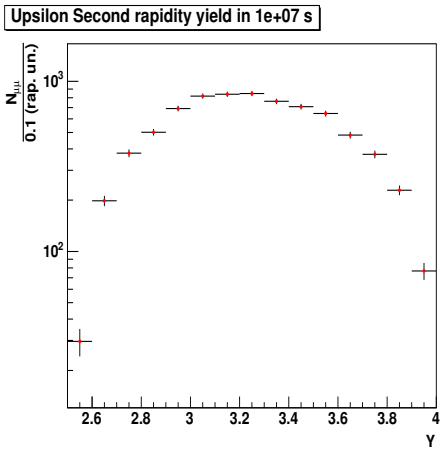

(c) Υ''

Fig. 5.5: Rapidity raw yields for bottomonium states in 10^7 s of data taking

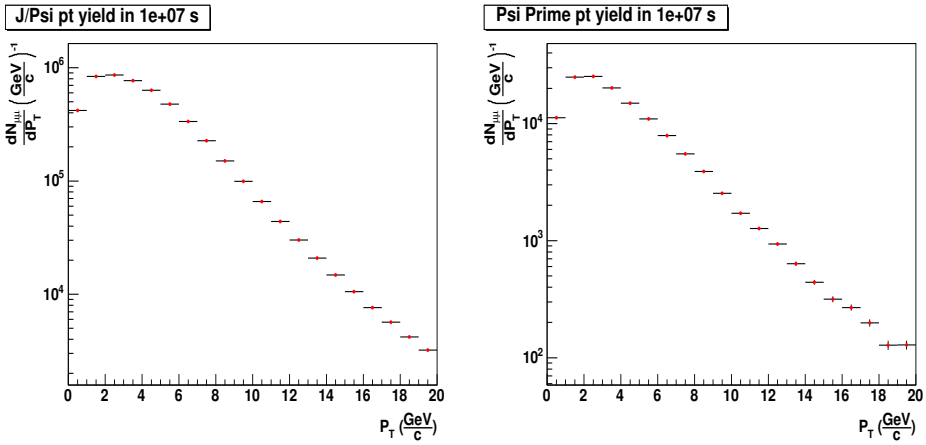

(a) J/ψ (b) ψ'

Fig. 5.6: p_T raw yields for charmonium states in 10^7 s of data taking

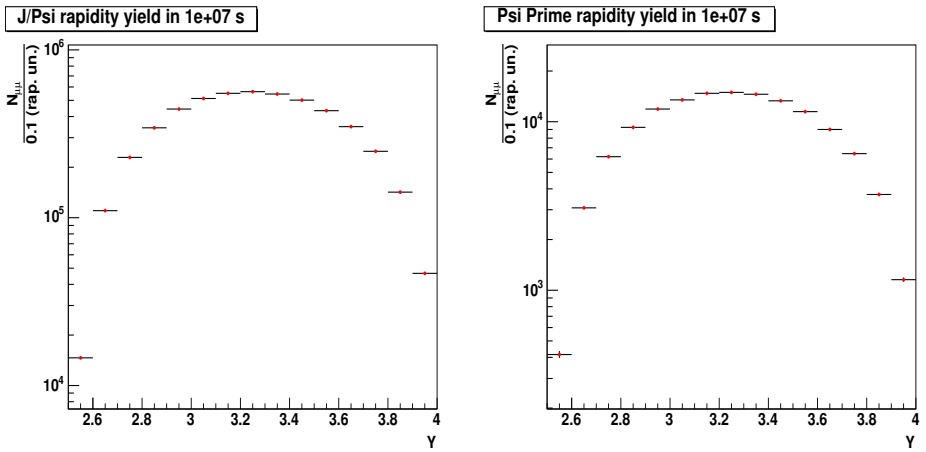

(a) J/ψ (b) ψ'

Fig. 5.7: Rapidity raw yields for charmonium states in 10^7 s of data taking

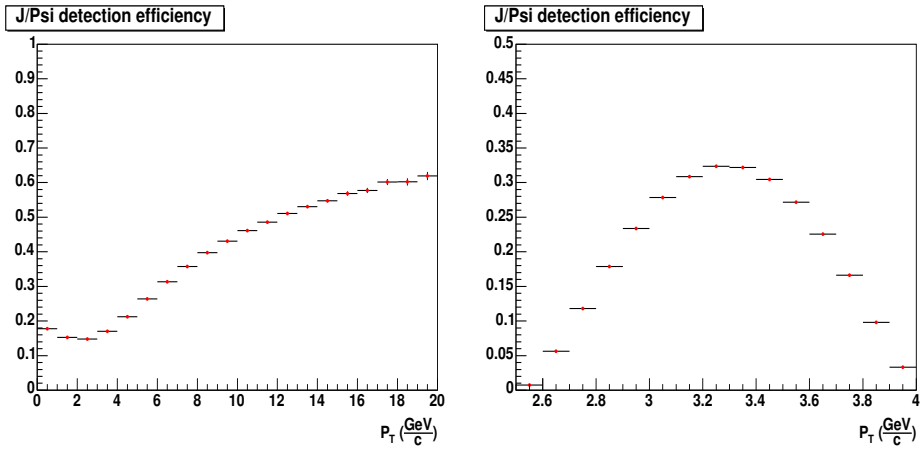

(a) J/ψ, $\varepsilon(p_T)$ (b) J/ψ, $\varepsilon(y)$

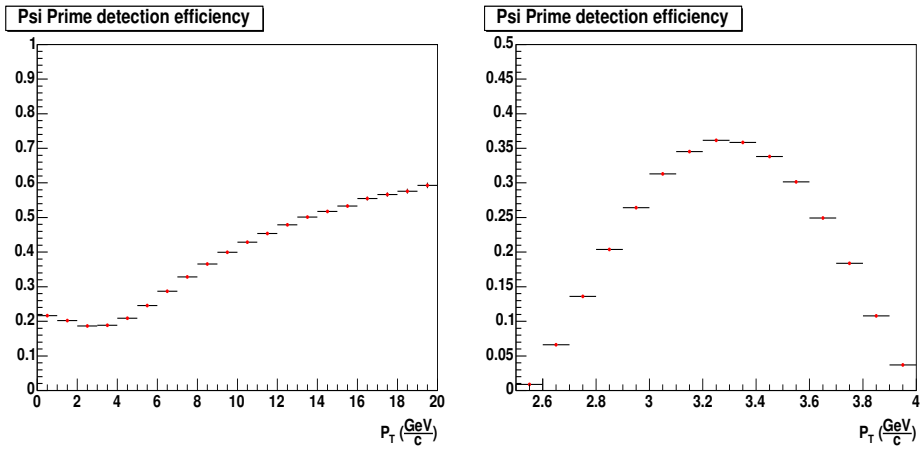

(c) ψ', $\varepsilon(p_T)$ (d) ψ', $\varepsilon(y)$

Fig. 5.8: p_T (left) and y (right) detection probabilities for charmonium states

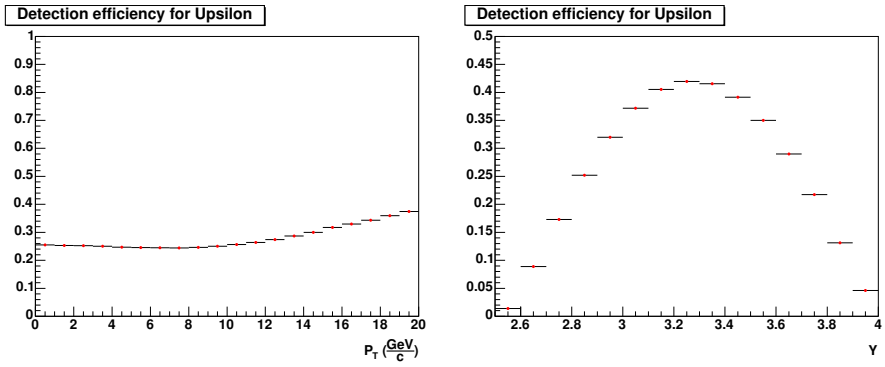

(a) Υ, $\varepsilon(p_T)$

(b) Υ, $\varepsilon(y)$

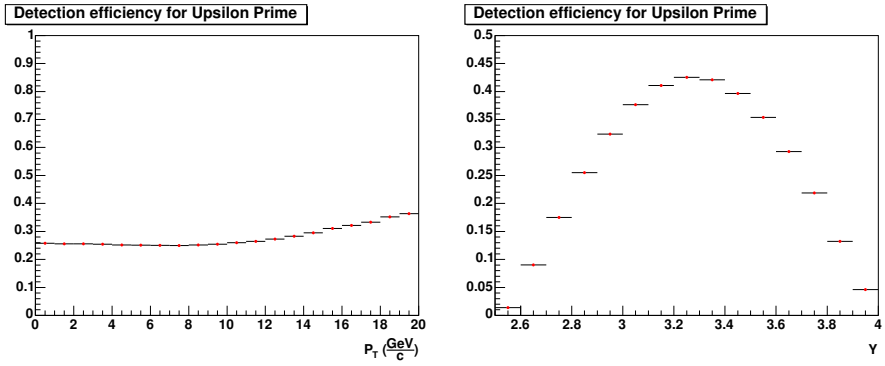

(c) Υ', $\varepsilon(p_T)$

(d) Υ', $\varepsilon(y)$

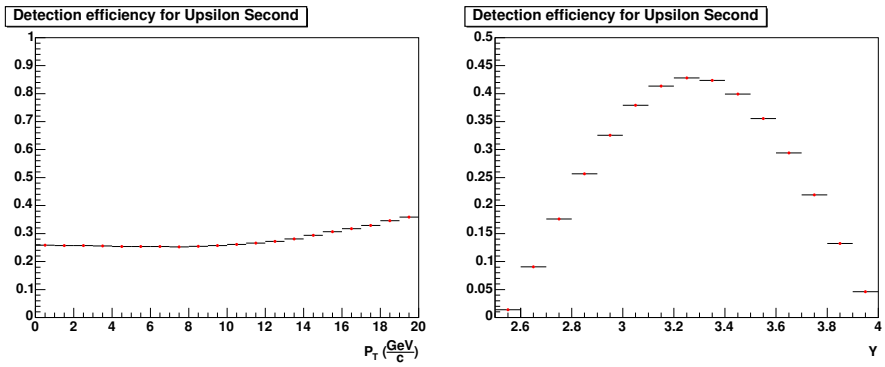

(e) Υ'', $\varepsilon(p_T)$

(f) Υ'', $\varepsilon(y)$

Fig. 5.9: p_T (left) and y (right) detection probabilities for bottomonium states

Finally, the mass spectra for each p_T or y bin are created and then fitted with a suitable function. The results will be used later in this chapter, when, having simulated data as they will appear after about one year of data taking at LHC, the contribution of quarkonia will be separated from the background.

The function used for the bottomonium states is the same adopted for the fit of charmonia resonances in the NA60 experiment [27]. It was found that the central part of the distributions could be described sufficiently well by a gaussian, with, in addition, two more gaussians of variable width for the large tails. The function has 11 parameters (p_0, p_1, ..., p_{10}) and reads:

$$\frac{dN_{sig}}{dm_{\mu\mu}} = p_0 \exp\left\{-\frac{1}{2}\left(\frac{m_{\mu\mu}-p_1}{\sigma}\right)^2\right\} \tag{5.3}$$

where

$$\sigma = \begin{cases} p_2\left[1+p_3(p_1p_9-m_{\mu\mu})^{(p_4-p_5\sqrt{p_1p_9-m_{\mu\mu}})}\right] & m_{\mu\mu} < p_1p_9 \\ p_2 & p_1p_9 \le m_{\mu\mu} \le p_1p_{10} \\ p_2\left[1+p_6(m_{\mu\mu}-p_1p_{10})^{(p_7-p_8\sqrt{m_{\mu\mu}-p_1p_{10}})}\right] & m_{\mu\mu} > p_1p_{10} \end{cases}$$

In the case of charmonium states it was noticed that, probably due to the higher statistics and to the better mass resolution, the NA60 fit function couldn't provide a good description of the mass distribution. In particular, it is clearly noticeable that the distribution shape is asymmetric even close to the mode. Hence it was decided to fit the central part of the mass spectrum not with just one gaussian, but with a gaussian (in the right side) and a gaussian with variable length (in the left side). The so obtained function has 15 parameters (p_0, p_1, ..., p_{14}) and can be described by the same formula adopted before (equation 5.3), but where:

$$\sigma = \begin{cases} \sigma'\left[1+p_{12}(p_1p_{11}-m_{\mu\mu})^{(p_{13}-p_{14}\sqrt{p_1p_{11}-m_{\mu\mu}})}\right] & m_{\mu\mu} < p_1p_{11} \\ p_2\left[1+p_3(p_1p_9-m_{\mu\mu})^{(p_4-p_5\sqrt{p_1p_9-m_{\mu\mu}})}\right] & p_1p_{11} \le m_{\mu\mu} < p_1p_9 \\ p_2 & p_1p_9 \le m_{\mu\mu} \le p_1p_{10} \\ p_2\left[1+p_6(m_{\mu\mu}-p_1p_{10})^{(p_7-p_8\sqrt{m_{\mu\mu}-p_1p_{10}})}\right] & m_{\mu\mu} > p_1p_{10} \end{cases}$$

The value of σ' is:

$$\sigma' = p_2\left[1+p_3(p_1p_9-p_1p_{11})^{(p_4-p_5\sqrt{p_1p_9-p_1p_{11}})}\right]$$

and corresponds to the value of the left tail of the peak at its limit. In this way the continuity of the function is preserved.

The fit to the pure signal events for the charmonium (bottomonium) states allows to fix 12 (8) out of the 15 (11) free parameters, corresponding

to the shape of the tails. In this way, when the fitting operation will be complicated by the presence of the background, only the mode value p_1, the width p_2 and the normalization p_0 will be let free to change.

Before going further, two considerations have to be done about the meaning of these parameters:

1. in the fast simulation the p_T smearing of each single muon is computed by sampling from an asymmetric distribution (see discussion in chapter 4), where mode and mean don't coincide. On average, the correction due to energy loss in the absorber corresponds to the mean of such distribution. Hence, when the muon pair invariant mass is calculated, the parameter correlated to the quarkonia mass is not the mode, p_1, but the mean, $\langle \mathrm{d}N_{sig}/\mathrm{d}m_{\mu\mu} \rangle$.

2. The quarkonia fit function parameter σ doesn't coincide with the standard deviation as we are not using a proper gaussian, except in a subrange of the mass spectra. However, in the following, such parameter will be often referred to as the distribution width, of which it is a rough estimate. Nevertheless, when the calculation of the total number of quarkonia in a $\pm n\sigma$ region around the peak will be performed, we will more appropriately refer to the half width half maximum (HWHM), which is well defined.

Due to the large statistics, it is possible to determine the mass distribution for quarkonia whose transverse momentum or rapidity is within a given interval. In this way it will be possible to determine, even with the presence of the background, the p_T and y distributions.

For each p_T or y bin, the mass spectra for charmonium resonances were fitted with the usual function of equation 5.3, leaving all parameters free. It was noticed that the shape of the tails showed some variations with respect to the one determined with the mass distribution integrated over p_T and rapidity. This can be easily understood, especially for the spectra where dimuons are chosen according to their p_T, because, at low transverse momenta, effects of the cut on muons and of energy loss in the absorber can be important.

In the case of bottomonium resonances, instead, due to the lower statistics, possible effects cannot be appreciated, so a reasonably good interpolation is obtained by fixing the tail parameters (from p_3 to p_{10}), with the values that we get from the mass spectrum integrated over p_T and y.

5.2.2 Correlated background[3]

The production of the background events proceeds parallel to the signal generation. With the term background it is meant muon pairs detected by the muon spectrometer, but that were not produced by heavy quarkonia decays. We distinguish between two main kinds of background:

- **combinatorial**, constituted, for *pp* collisions, by muons coming from abundantly produced kaons or pions. They have no correlation among each other, as they are generated by uncorrelated particles.
- **correlated**, constituted by muons coming from open beauty and open charm (i.e. respectively bottom and charm flavored mesons, such as B and D) decay. The pairs, although not produced from the same particle, are correlated because they're generated in the same process.

The combinatorial background haven't been produced in *pp* collisions at 14 TeV yet. This, of course, has to be done as soon as possible. However referring to the results from a previous work (cf. [8]), we don't expect this kind of background to count much, as it is almost one order of magnitude lower than the correlated.

There are five main processes contributing to the combinatorial background:

DDprompt:	$\mu^+ X_1$	$\leftarrow D(c)$	$D(\bar{c}) \rightarrow$	$X_2\, \mu^-$
BBdiff:	$\mu^+ X_1$	$\leftarrow B(\bar{b})$	$B(b) \rightarrow$	$X_2\, \mu^-$
BDdiff:	$\mu^+ X_1$	$\leftarrow B(\bar{b})$	$B(b) \rightarrow$	$D(c)\, X_2$
				$\hookrightarrow X_3\, \mu^+$
DDdiff:	$X_1\, D(\bar{c})$	$\leftarrow B(\bar{b})$	$B(b) \rightarrow$	$D(c)\, X_2$
	$\mu^-\, X_3 \hookleftarrow$			$\hookrightarrow X_4\, \mu^+$
BDsame:	$X_1\, X_2$	$\leftarrow B(\bar{b})$	$B(b) \rightarrow$	$D(c)\, \mu^-$
				$\hookrightarrow X_3\, \mu^+$

The naive picture is somewhat complicated by B meson oscillations, included in the simulation, that can change the sign of the muons produced.

Heavy flavor decays can be divided into two main topologically distinct contributions: b-chain decays where low mass and high transverse momentum dimuons are produced (BDsame) and muon pairs where the two muons originate from different quarks emitted at large angles, resulting in large invariant masses. If a cut in the muon transverse momentum is applied, the secondary decays are heavily suppressed, as some fraction of the momentum has already been used in the primary decay.

[3]Many thanks to *Rachid Guernane* from Clermont-Ferrand university, who actually generated the open charm and bottom mesons obtained with PYTHIA and provided me with the analysis macro.

The produced background has been analyzed through the fast simulation. Two different results are produced, according to which trigger cut is used (1 GeV if we want to study charmonia, 2 GeV for bottomonia). The contribution of each background component is shown in figure 5.10(a) and 5.10(b). In the analysis, like-sign muons have been rejected.

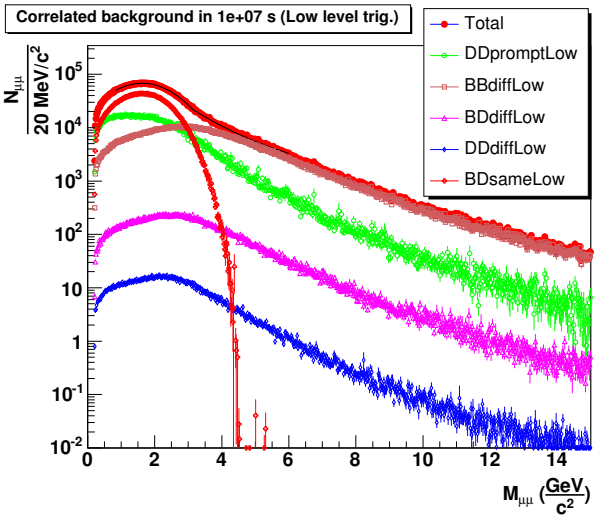

(a) p_T cut = 1 GeV

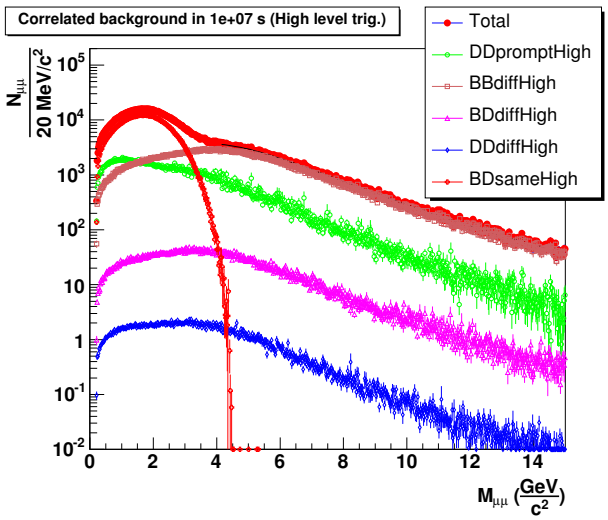

(b) p_T cut = 2 GeV

Fig. 5.10: Correlated background mass distribution analyzed with fast simulation. Contribution from different sources is shown.

It is clear from the picture that the background fluctuations, especially at high p_T, are too large if compared with the pure statistical ones (going like the square root of the number of particles per bin, $\sqrt{N}$). This is due to the fact that it was generated a number of events lower than the one expected in 10^7 s, and then the result was opportunely scaled to the expected value. In order to take into account this fact, the obtained mass distribution was fitted with a suitable function and then the background was generated again from the so obtained parameterization with the desired statistics. The background in the 1 GeV p_T cut was interpolated in the mass region $0.81<m_{\mu\mu}<6.02$, while the one with the 2 GeV cut in the region $4.1<m_{\mu\mu}<14.4$.

The function used has 5 free parameters (p_0^{bkg}, p_1^{bkg}, ..., p_4^{bkg}) and reads:

$$\frac{dN_{corr}}{dm_{\mu\mu}} = p_0^{bkg} \exp\left\{-\frac{1}{2}\left(\frac{m_{\mu\mu}-p_1^{bkg}}{\sigma}\right)^2\right\} \tag{5.4}$$

where

$$\sigma = \begin{cases} p_2^{bkg} & m_{\mu\mu} < p_4^{bkg} \\ p_2^{bkg}\left[1+p_3^{bkg}(m_{\mu\mu}-p_4^{bkg})\right] & m_{\mu\mu} \geq p_4^{bkg} \end{cases}$$

5.2.3 Signal + background

The signal and the background, separately generated, have to join together in the final analysis. The raw mass distribution yields, obtained by using the same data taking conditions, can be summed together without further scalings. The result is what we expect to see after about one year of data taking at LHC (excluding the combinatorial background), and corresponds to the starting point of the analysis, which consists in disentangling the contribution of signal and background.

The disentanglement proceeds in two steps:

1. **Background fit.** A fit, with the function of equation 5.4, is performed in the mass region were the contribution of resonances is negligible. The operation allows to fix the function parameters from p_2^{bkg} to p_4^{bkg}: only the normalization (p_0^{bkg}) is let free.

2. **Global fit.** The mass distributions of the opposite sign muon pairs are interpolated by a function which is a sum of the background described by equation 5.4 and as many functions determined by equation 5.3 as the number of quarkonia. The free parameters are just the background and resonances normalizations and the resonances widths and mean values.

The results are shown in figure 5.11(a) and 5.11(b) for charmonia and bottomonia respectively.

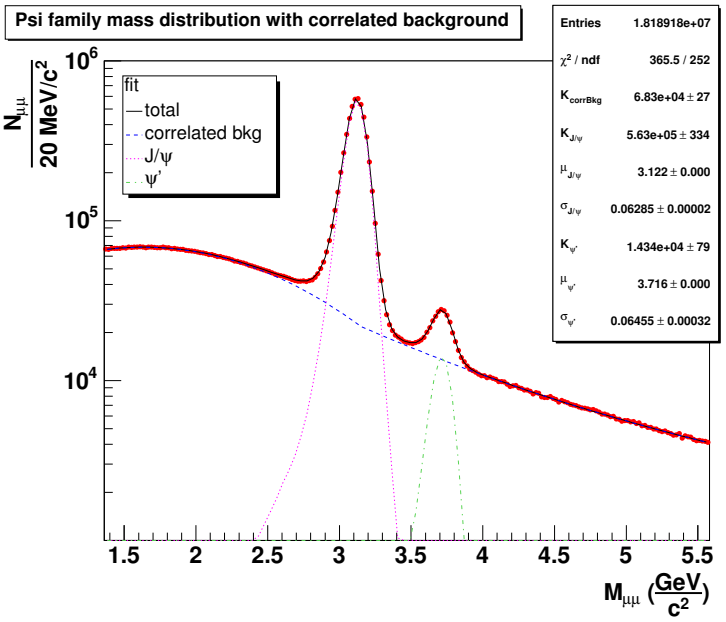

(a) ψ family

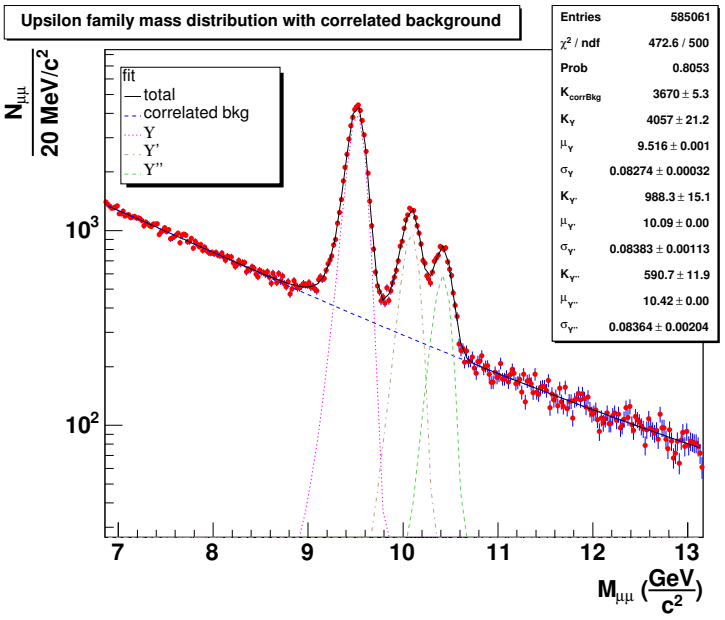

(b) Υ family

Fig. 5.11: Unlike-sign dimuon mass spectra for a running time of 10^7 s

From the fit functions it is possible to get the expected number of quarkonia. Since the global fit is obtained by summing together the background

and the signal, the parameters it gives already take into account each single contribution to the total yield. This means that, if we want to get the expected number of quarkonia, it is enough to integrate the resonance fit function of equation 5.3 with the parameters we got from the global fit.

The uncertainty on the final results comes from two different sources: the error on the normalization and the one on the distribution width, both given by the root minimization package *TMinuit* (cf. root homepage [29] for further details). The error on the mean value doesn't affect in any way the integral, as it changes only the position of the peak. Therefore it is not taken into account. From the other side it is clear that the other quantities are correlated because, for a fixed integral value, an increase of the distribution width implies a lower value of the normalization factor.

Error on parameters has to be properly propagated in order to get the uncertainty on the integral. If we consider a function of N parameters $f(x_1, x_2, \ldots, x_N)$ and we indicate with δ_{x_i} the error on each parameter, the uncertainty on the function is given by the formula:

$$\delta_f^2 = \sum_{i=1}^{N} \left(\frac{\partial f}{\partial x_i} \, \delta_{x_i} \right)^2 + \sum_{i<j}^{N} 2 \frac{\partial f}{\partial x_i} \, \frac{\partial f}{\partial x_j} \, \delta_{x_i x_j}$$

where $\delta_{x_i x_j}$ is the covariance.

The normalization parameter is just a multiplicative factor, hence if we call $N_{sig}(p_0, p_2)$ the integral of the quarkonia fit function of equation 5.3, namely

$$N_{sig} = \int_{m_1}^{m_2} \mathrm{d}m_{\mu\mu} \frac{dN_{sig}}{dm_{\mu\mu}}$$

we get:

$$\frac{\partial N_{sig}}{\partial p_0} = \frac{N_{sig}}{p_0}$$

More complicated is the case of the partial derivative with respect to the width p_2, due to the fact that the fit function is not analytically integrable. In this case we can give an estimate of the value of the derivative by exploiting its definition as limit of the incremental ratio for a step-size that goes to zero. If the uncertainty on the parameter, δ_{p_2}, is small enough we can write:

$$\frac{\partial N_{sig}}{\partial p_2} \simeq \frac{N_{sig}(p_0, p_2 + \delta_{p_2}) - N_{sig}(p_0, p_2)}{\delta_{p_2}}$$

The value of the covariance is again given by the root minimization package. Thus we finally get:

$$\delta_{N_{sig}}^2 = \left(\frac{N_{sig}(p_0, p_2)}{p_0} \, \delta_{p_0} \right)^2 + \left[\left(N_{sig}(p_0, p_2 + \delta_{p_2}) - N_{sig}(p_0, p_2) \right) \, \delta_{p_2} \right]^2 + 2 \frac{N_{sig}(p_0, p_2)}{p_0} \, \frac{N_{sig}(p_0, p_2 + \delta_{p_2}) - N_{sig}(p_0, p_2)}{\delta_{p_2}} \, \delta_{p_0 p_2}$$

The described method was applied to the global invariant mass distributions of figures 5.11(a) and 5.11(b) in order to get the expected rates of signal and correlated background. The results are summarized in table 5.3, together with the signal-to-background (S/B) ratio and the significance ($S/\sqrt{S+B}$) for detecting the various resonances. The values, except when explicitly indicated, have been calculated in a region where the width of the distribution corresponds to twice the FWHM.

Quarkonium	Signal (S) in units of 10^3		Correlated background (B) in units of 10^3	$\frac{S}{B}$	$\frac{S}{\sqrt{S+B}}$
	FWHM	2 FWHM			
J/ψ	3526	4674	370	12.6	2081
ψ'	92	122	220	0.55	209
Υ	33.5	44.7	7.7	5.8	195
Υ'	8.5	11.4	6.1	1.9	86
Υ''	5.2	6.9	5.4	1.3	62

Tab. 5.3: Expected signal rates for different quarkonium states. The numbers correspond to an interval where the width of the mass distribution corresponds to twice the FWHM (except when specified). All rates and ratios are for 10^7 s running time. *Only correlated background is taken into account.*

If we take into account the mass distribution of dimuon pairs whose p_T or y lie within a specified interval and we perform the global fit, we can get the number of resonances (with the corresponding error) per each p_T or y bin and we can hence reproduce the distributions previously obtained with the pure signal only. Even in this analysis the tails are fixed (see discussion at the end of section 5.2.1).

Two different approaches are followed for charmonium and bottomonium states. In the latter case the normalization, mode and width of each resonance are let free, exactly as in the global fit. In the former, instead, it was decided to fix the mode and the width of ψ', because the results of the fit depends, to some extent, on the shape of the J/ψ tail.

The results are shown in figures 5.12 and 5.13 for J/ψ and Υ respectively.

For higher mass quarkonia some work still has to be done. In fact due to their lower statistics, their mass distribution is affected by the shape of the background and of the right tail of the $1S$ state. Thus, the reconstructed p_T and y distributions show fluctuations which are not explained by statistical error only. The effects that lead to such variations should be further investigated, but, as they can be classified as part of the systematic, their analysis is beyond the objectives of this thesis and won't be presented. Nevertheless, an accurate study of such phenomena and of the systematic

error has to be performed as soon as possible, together with the inclusion of the combinatorial background and the analysis of the $\psi(nS)/\psi(1S)$ and $\Upsilon(nS)/\Upsilon(1S)$ observables.

Finally, if we correct for detection probabilities we can get the differential cross section in transverse momentum and rapidity (figures 5.14 and 5.15). The distributions in p_T are integrated in the rapidity coverage of the detector ($2.5 < y < 4$).

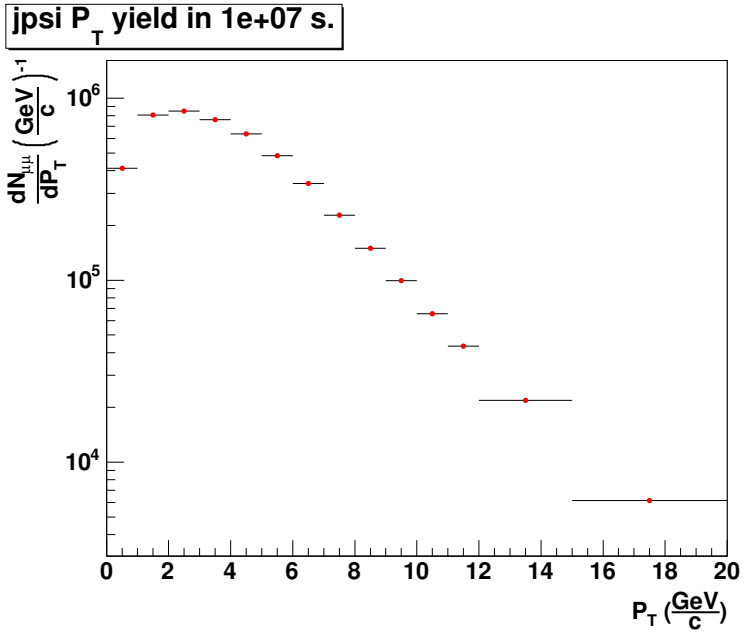

(a) p_T

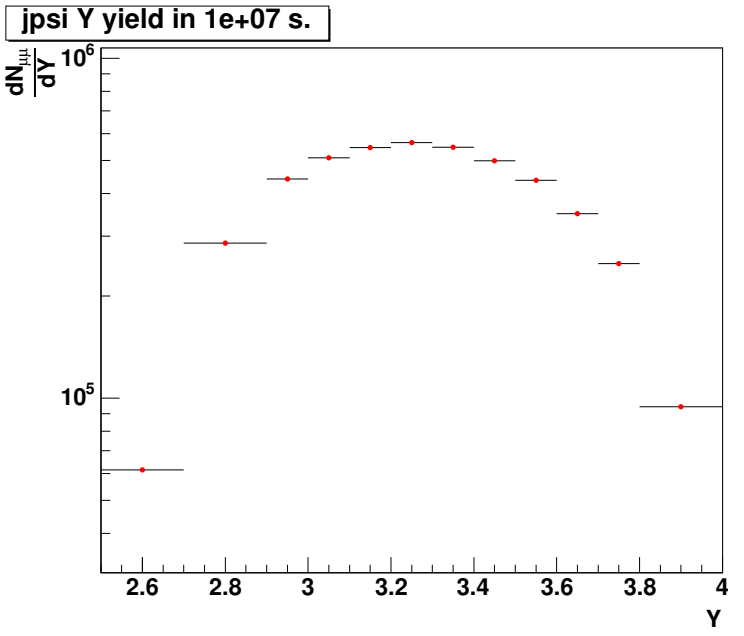

(b) y

Fig. 5.12: p_T and y raw yields for J/ψ in 10^7 s of data taking, obtained after background subtraction

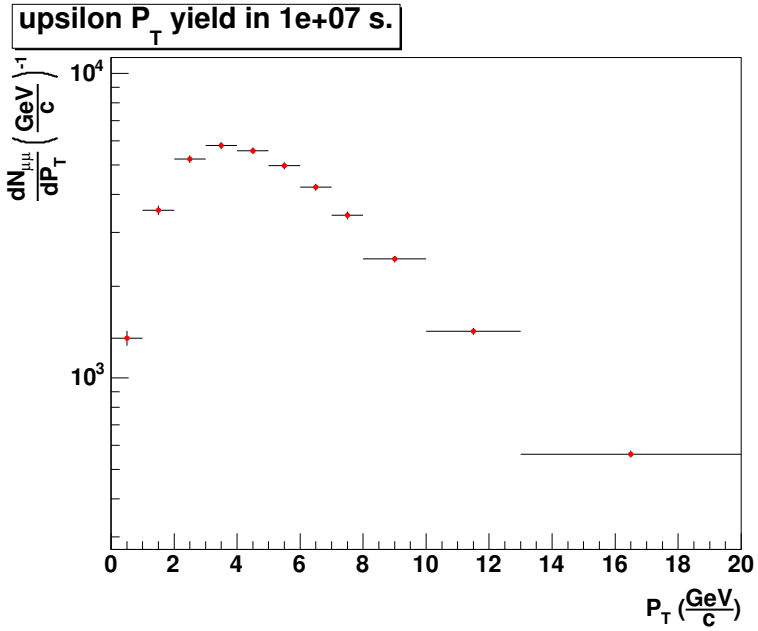

(a) p_T

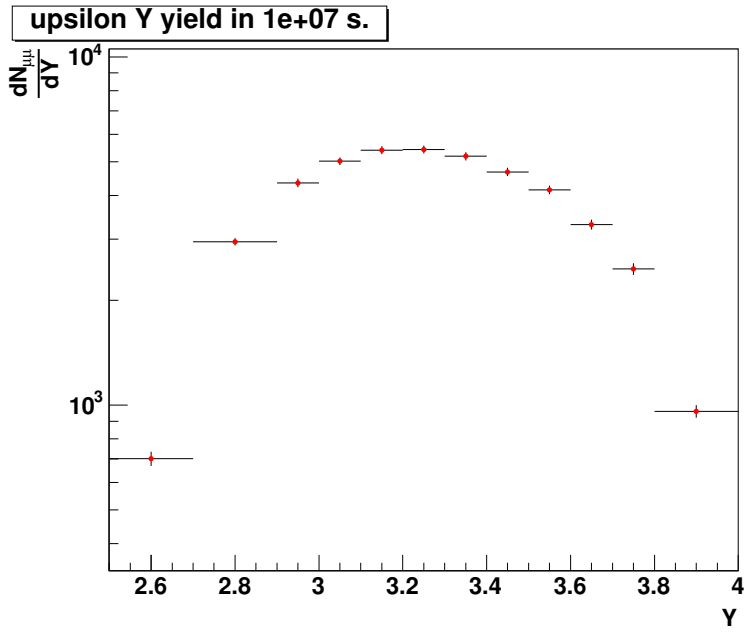

(b) y

Fig. 5.13: p_T and y raw yields for Υ in 10^7 s of data taking, obtained after background subtraction

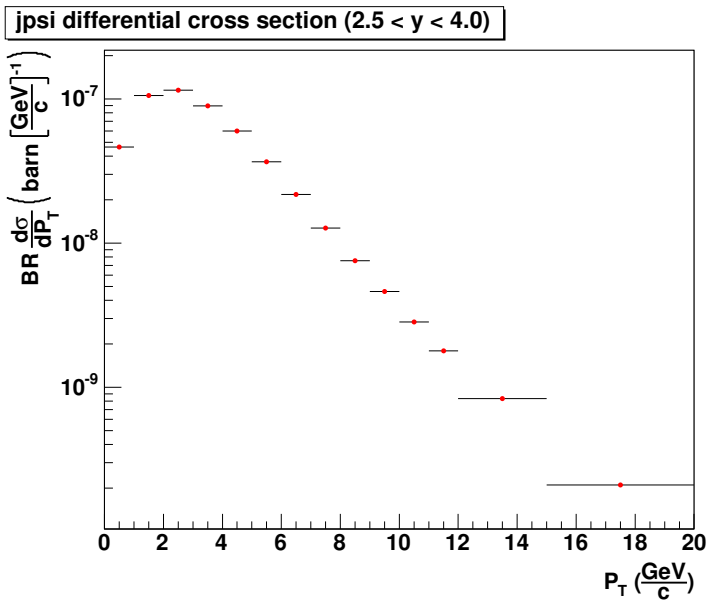

(a) p_T

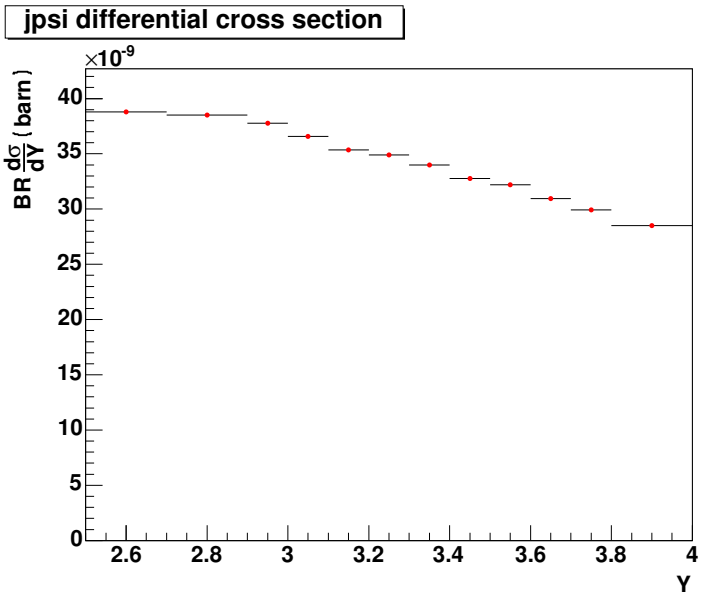

(b) y

Fig. 5.14: p_T and y differential cross section for J/ψ, obtained after background subtraction. The results are expected to be measured in 10^7 s. p_T cross section is integrated in the detector rapidity coverage ($2.5 < y < 4$).

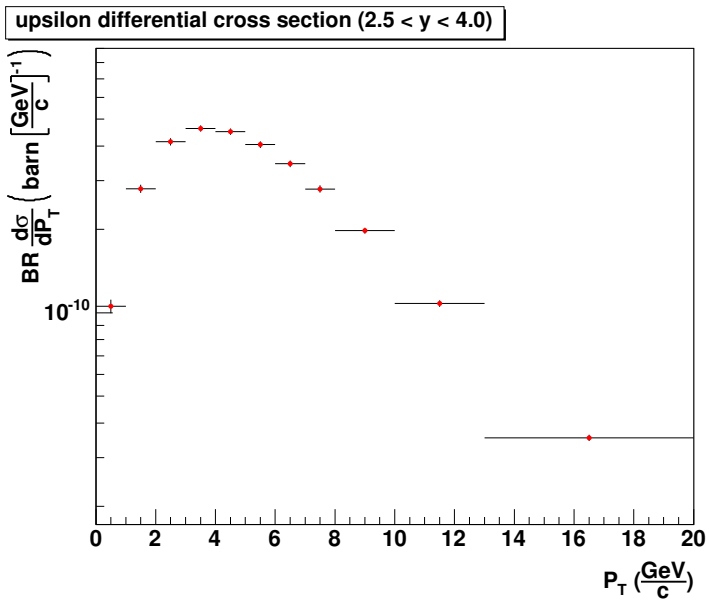

(a) p_T

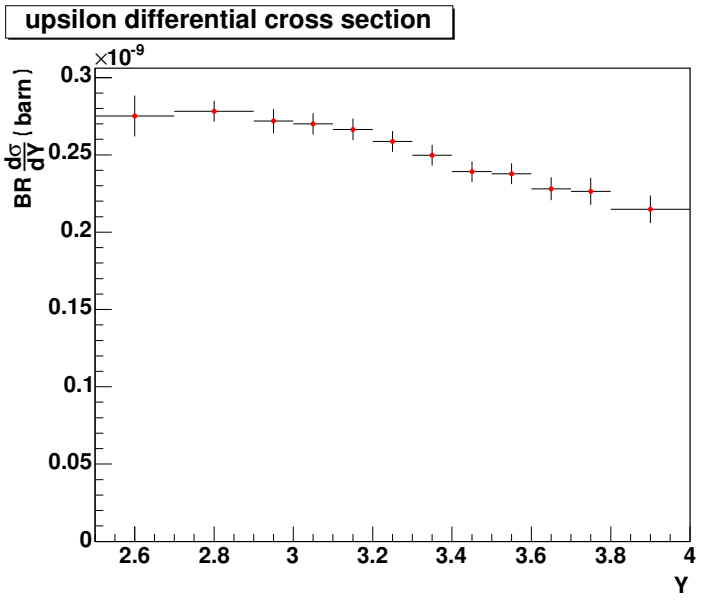

(b) y

Fig. 5.15: p_T and y differential cross section for Υ, obtained after background subtraction. The results are expected to be measured in 10^7 s. p_T cross section is integrated in the detector rapidity coverage ($2.5 < y < 4$).

Chapter 6

Study of an unexplored physical region

In the previous section of this thesis simulation results concerning the performance of the muon spectrometer with respect to heavy quarkonia detection were shown. Starting from rapidity distributions predicted by the color evaporation model and from transverse momentum ones, opportunely rescaled from CDF data at lower center of mass energy, it was possible to obtain the distributions expected with the defined data taking conditions (cf. section 5.2).

In this section, a further interesting use of the forward muon spectrometer will be shown: the study of Parton Distribution Functions (PDF) in a still unexplored physical region.

6.1 Introduction

The concept of parton distribution function was born several years ago, after a long discovery process that, from the description of the world in terms of atoms, led to an analogous one in terms of quarks and leptons.

At the beginning of the 40s, the advent of the accelerators allowed the study of the until then known particles, with higher and higher energies. In particular it was noticed that hadrons such as the proton, which appeared as point-like if probed with low energy leptons, showed an inner charge distribution if probed with higher momentum projectiles, thus suggesting the presence of a deeper structure, typical of composed objects. Nevertheless, if energy was high enough (Deep Inelastic Scattering), the effects of the inner structure seemed to disappear and the probing particles showed the same behavior they would have if colliding against point-like objects.

In 1964 Gell-Mann and Zweig suggested that hadrons were formed by point-like fundamental constituents with fractional electromagnetic charge: the partons. After the initial hesitation in accepting a theory whose con-

stituents couldn't be experimentally observed (due to the confinement), the Gell-Mann and Zweig hypothesis, after evolving into the quark concept, merged into the current particle physics theory: the Standard Model.

High energy collisions between hadrons, can thus be more easily explained through collisions between quarks and gluons inside the hadrons themselves. Unfortunately, while the energy and momentum of particles composing the beam in collider and linear accelerator experiments are usually well known, the kinematic distribution of the fundamental constituents is not known a priori and has to be determined phenomenologically by a global analysis of a wide range of available hard scattering processes involving initial-state hadrons, using the perturbative QCD-parton framework.

A lot of work has been done about this topic (e.g. see [30, 31]), but the characteristics of the experiments allow to probe for parton distribution functions only in limited regions. Every possible extension of the studied domain is of fundamental importance for the knowledge of QCD phenomena.

Before going further in the description of the PDFs used, it is necessary to give some definitions. In order to better understand the physical meaning of the relativistic invariant variables that will be used in the following, they won't be described in a proton-proton collision but in a simpler case.

Let's consider in particular the inelastic lepton-proton scattering (figure 6.1), which was historically important because it led to the first clear evidence for scattering from individual quark constituents confined within the proton.

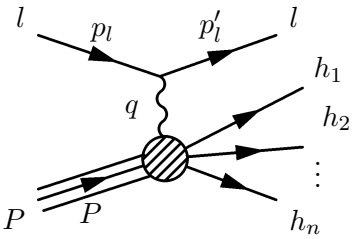

Fig. 6.1: Scheme of electron proton scattering

The cross section of the process is a generalization of the Rosenbluth formula and reads:

$$\left.\frac{d\sigma}{d\Omega dE'}\right|_{LAB} = \frac{\alpha^2}{4|\vec{p}_l|^2 \sin^4 \vartheta/2} \cos^2 \vartheta/2 \left(W_2(\nu, q^2) + W_1(\nu, q^2) \tan^2 \vartheta/2\right)$$

where ϑ is the angle of the outgoing lepton with respect to the ingoing one. The cross section can be parameterized by two *structure functions* $F_1(x, Q^2)$ and $F_2(x, Q^2)$, which are the analogous of the form factor and are defined

as:

$$\begin{aligned} F_1(x, Q^2) &= MW_1(\nu, q^2) \\ F_2(x, Q^2) &= \nu W_2(\nu, q^2) \end{aligned}$$

The Q^2 is the square of the quadri-momentum transferred, given by:

$$Q^2 = -q^2 = -\left[(E_l - E'_l)^2 - (\vec{p}_l - \vec{p}'_l)^2\right]$$

where the initial and final leptons have energies and momenta (E_l,$\vec{p}_l$) and (E'_l,$\vec{p}'_l$) respectively.

The relativistic invariant x (Bjorken), is:

$$x = \frac{Q^2}{2P \cdot q}$$

where P is the proton initial quadri-momentum (see figure 6.1).

In the parton model, the interaction of a lepton with a proton can be seen as the elementary interaction with a constituent parton. From this point of view it can be shown that if $Q^2 \gg M_p^2$ (i.e. the proton mass), the Bjorken x assumes the physical meaning of the *fraction of proton momentum carried by the parton*.

By increasing the center of mass energy it is possible to probe lower x values, i.e. constituents which carry a lower fraction of the hadron momentum. At present the explored region goes down to x values of 10^{-5}.

The use of perturbative QCD makes possible to relate the structure functions $F_1(x, Q^2)$ and $F_2(x, Q^2)$ to process independent *parton distribution functions* $f_i(x, Q^2)$ which describe the distribution of the i-th quark (gluon) carrying a fraction x of the hadron momentum. The relations can be determined at a specific order in perturbation theory, thus giving rise to LO or NLO PDFs that will be discussed in the following. At leading order we get:

$$F_2(x, Q^2) = x \sum_q e_q^2 f_q(x, Q^2)$$

where e_q^2 is the fractional electric charge of the involved quark q.

6.2 Parton Distribution Functions (PDFs)

The global analysis of parton distributions requires a continuous effort. As new experimental and theoretical advances occur, the parton distributions can be determined with increasing accuracy and over a wider x domain. There are two important motivations for the vigorous pursuit of global analysis:

- when available experimental constraints exceed the degrees of freedom of the theory, they can be used to prove the validity or to set the boundaries of applicability of the theory itself
- since the global analyses inevitably involve both experimental and theoretical uncertainties, it is important to quantify the uncertainties in the resulting parton distributions.

A huge number of parton distribution functions are at present employed in particle physics. In the following analysis it will be shown a comparison between three of them, provided by the CTEQ and MRST collaboration.

6.2.1 CTEQ

The *Coordinated Theoretical-Experimental Project on QCD* (CTEQ) is a multi-institutional collaboration devoted to a broad program of research projects and cooperative enterprises in high-energy physics centered on Quantum Chromodynamics (QCD) and its implications in all areas of the Standard Model and beyond.

The collaboration created several PDFs with increasing accuracy, due to the possibility to access newer data from recent experiments and to an improvement of theoretical calculations. The series of global QCD analyses of the CTEQ group [32] was extended in order to include significant new experimental results that will be briefly summarized. The first version considered in this thesis is the CTEQ5 (cf. reference [30]).

Deep inelastic scattering: Results from NMC and CCFR collaborations respectively on muon-nucleon and neutrino-nucleon scattering lead to subtle changes in their implications for α_s and parton distribution determination. Moreover the data from H1 and ZEUS collaborations at HERA on total inclusive structure functions F_2^p provide tighter constraints on the quark and gluon distributions, mainly through the Q evolution of the structure functions.

Lepton pair production (p/d) asymmetry: E866 collaboration has measured the ratio of lepton pair production (Drell-Yan process) in pp and pd collisions over the x range 0.03-0.35, thus expanding greatly the experimental constraint on the ratio of parton distributions $\bar{d}/\bar{u}$.

Lepton charge asymmetry in W production: CDF collaboration has improved the accuracy and extended the rapidity range of the measurement of the asymmetry between $W \to l^{\pm}\nu$ at the Tevatron, which lead to additional constraints on d/u.

Inclusive large p_T jet production: Inclusion of systematic errors by D$\emptyset$ collaboration and new results in inclusive jet production data by CDF

led to a better constraint on the parton transverse momentum distributions.

Direct photon production: E706 collaboration at Fermilab has published the highest energy fixed-target direct photon production data available. The measured cross sections lie a factor of 2-3 above the traditional NLO QCD calculation.

The $\{x, Q\}$ region covered by the experiments is shown in figure 6.2. Using these data as a baseline, it was possible to generate a number of different parton distribution functions, summarized in table 6.1. We are particularly interested in the CTEQ5L, i.e. the leading order QCD and in the CTEQ5M, defined in the $\overline{MS}$ scheme, matched with conventional NLO hard cross sections calculated in the zero-quark-mass approximation for all active flavors. The latter is specifically the most convenient to use for general calculations.

Figure 6.3 shows the output of CTEQ5M PDF set for all partons and gluons.

PDF Set	**Description**
Conventional (zero-mass parton) sets	
CTEQ5M	$\overline{MS}$ scheme
CTEQ5D	DIS scheme
CTEQ5L	Leading-order
CTEQ5HJ	Large-x gluon enhanced
on-mass-shell heavy quark sets	
CTEQ5HQ	$\overline{MS}$ (ACOT) scheme
CTEQ5F3	Fixed-flavor-number ($N_f = 3$) scheme
CTEQ5F4	Fixed-flavor-number ($N_f = 4$) scheme

Tab. 6.1: CTEQ5 PDF sets summary

The second CTEQ version adopted in this thesis is the more recent CTEQ6 (cf. reference [33]). It improves the analysis of the data sets used by the previous CTEQ5, owing to the study of the correlated systematics errors, and makes use of more recent results. Particularly noteworthy are the recent neutral current deep-inelastic scattering (DIS) structure function measurements of H1 and ZEUS, and the inclusive jet cross section measurement of DØ (in several rapidity bins, up to a rapidity of 3). Other recent data used in the analysis are the updated E866 measurements of the Drell-Yan deuteron/proton ratio and the re-analyzed CCFR measurement of F_2.

Even in the case of CTEQ6, many different versions were developed, within different renormalization schemes and calculation orders, exactly as

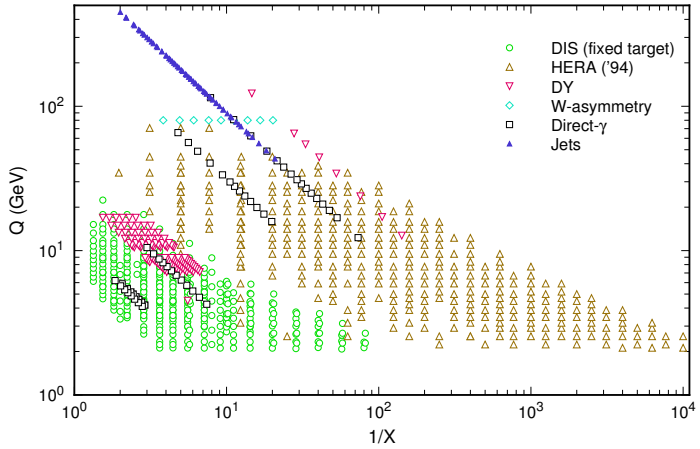

Fig. 6.2: Kinematic $\{x$,Q$\}$ map of the experiments used in the CTEQ5 fit

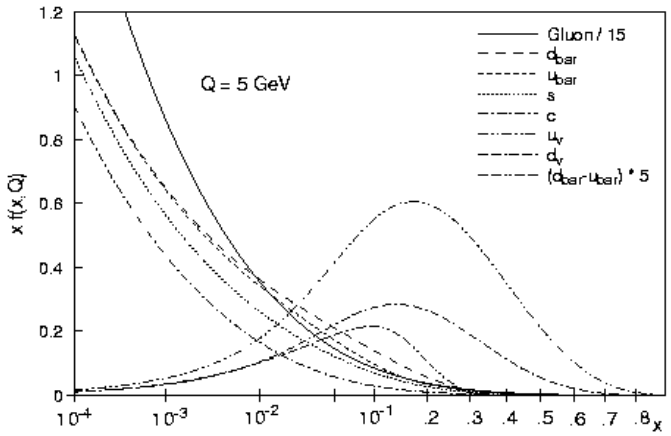

Fig. 6.3: Overview of CTEQ5M parton distributions (multiplied by x) at $Q = 5$ GeV. The gluon distribution is scaled down by a factor of 15, and the $\bar{d} - \bar{u}$ distribution is scaled by a factor of 5

in the case of CTEQ5. A global overview of the CTEQ6M PDF set is shown in figure 6.4.

6.2.2 MRST

The second set of PDFs considered here is the *Martin, Roberts, Stirling and Thorne* (MRST) one.

Even in this case it exists a constant updating of PDFs, by including significant new experimental results. In particular, the 1998 structure function set (cf. [31]) was taken into account. The experimental measurements

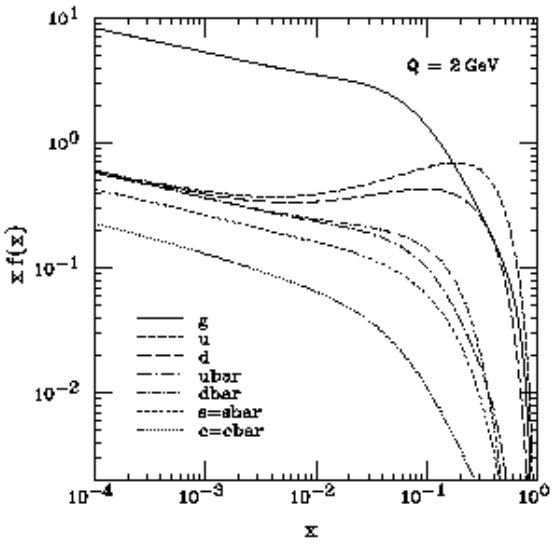

Fig. 6.4: Overview of CTEQ6M parton distributions (multiplied by x) at $Q = 2$ GeV.

employed by MRST collaborations are almost exactly the same adopted in CTEQ5 calculation, summarized in section 6.2.1. There are only two differences:

- The Drell-Yan production obtained by E772 collaboration is employed together with the data from E605, which is used to constrain the sea (as in CTEQ). For $x_F \sim 0$ both experiments provide a useful measure of the quark sea at larger value of x, typically $x \lesssim 0.3$. For larger x_F the E772 data probe, in principle, the valence quarks at $x \sim 0.5$ and the sea quarks at $x \sim 0.025$.

- The W70 prompt proton measurements are used in order to set constraints on the gluon distributions outside the HERA small x ($x \sim 10^{-3}$). CTEQ5 collaboration employed E706 data instead.

The parton distribution functions are determined from a global fit to a wide range of deep inelastic and related hard scattering data. The basic procedure is to parameterize the $f_i(x, Q^2)$ at a low value of $Q^2 = Q_0^2$ such that they can be calculated at higher Q^2 by using NLO DGLAP (Dokshitzer-Gribov-Lipatov-Altarelli-Parisi) evolution equations. Data are fitted for all $Q^2 > Q_1^2$, where $Q_1^2 > Q_0^2$ is a value of Q^2 where perturbative QCD is believed to be the dominant contribution.

A detailed description of the procedure adopted to get the MRST PDF set is given in the Martin, Roberts, Stirling, Thorne paper [31], and won't be further discussed. However, as we are particularly interested in gluon

distribution functions, some more information about this topic will be provided.

As already said the main constraints in the gluon distribution at large x are data on prompt photon production in pp or pA collisions from WA70 and E706 experiments. The latter data confirm the implication from other high energy prompt photon experiments that a significant initial state partonic transverse momentum is needed to obtain agreement with the NLO QCD prediction. A question rose whether such a transverse momentum component should be included when determining the behavior of the gluon at large x ($x \simeq 0.4$) from the lower energy ($\sqrt{s} = 23$ GeV) WA70 experiment — even though the WA70 data can be adequately described without such a component. E706 data (corresponding to $\sqrt{s} = 31.5$ and 38.8 GeV) were found to require an average value of the transverse momentum of the initial partonic system $\langle k_T \rangle \sim 1$ GeV, expected to be less for experiments at lower energies. $\langle k_T \rangle$ values from 0 to 0.64 GeV, i.e. the maximum value found compatible with a reasonable description of WA70 data, were taken into account. Three gluon distributions were thus created, namely:

- MRST($g \uparrow$), called higher gluon ($\langle k_T \rangle = 0$ GeV)
- MRST, called central gluon ($\langle k_T \rangle = 0.4$ GeV)
- MRST($g \downarrow$), called lower gluon ($\langle k_T \rangle = 0.64$ GeV)

The name derive from the fact that a smaller gluon density is compensated by a larger $\langle k_T \rangle$. Differences among the three distributions are shown in figure 6.5. The choice of the set, although affecting the large x region ($x \gtrsim 10^{-2}$), has almost no effect on the small one, which is the region that can be studied in the detector acceptance (see figure 6.10).

The PDF set adopted in this thesis is the MRST central gluon, in order to be consistent with Ramona Vogt's color evaporation model calculations [34]. An overview of this set for Q^2 values of 20 GeV^2 is shown in figure 6.6.

6.2.3 Main differences between models

In order to compare two different parton distribution function sets, it is necessary to take into account possible discrepancies not only in input data and analysis procedure but also in choices of renormalization and factorization schemes.

If we take into account the gluon distributions given by CTEQ and MRST, we notice that the difference due to the choice of the scheme is completely overshadowed by that due to the choice of experimental input. In order to complement the DIS constraints in determining $G(x, Q^2)$, CTEQ collaboration used inclusive jet data of CDF and D$\emptyset$, whereas MRST relied on direct photon production results of WA70, applying a range of $\langle k_T \rangle$ broadening corrections using the E706 data as a constraint, as previously

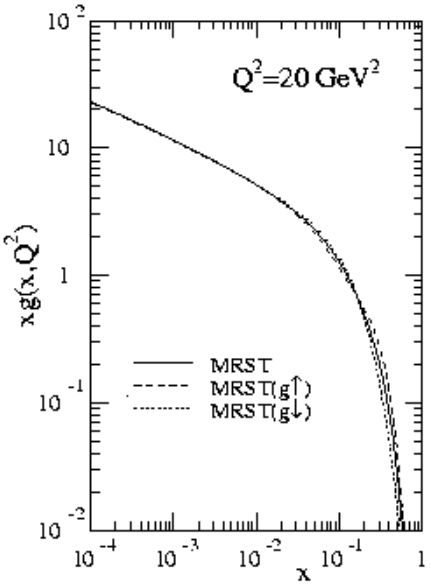

Fig. 6.5: The gluon distributions (multiplied by x) at $Q^2 = 20\,GeV^2$ corresponding to the MRST, MRST(g↑) and MRST(g↓) sets of partons with, respectively, the central, larger and smaller gluon at large x

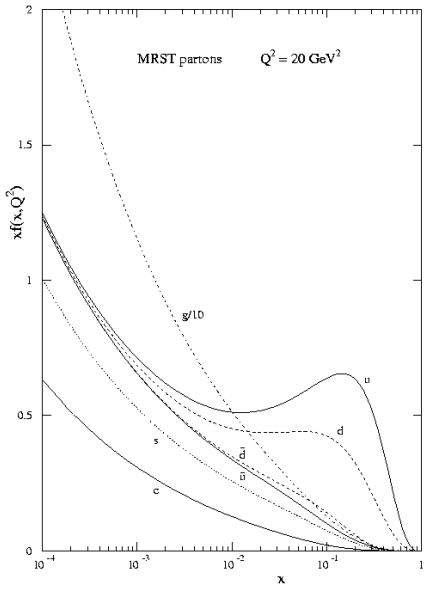

Fig. 6.6: Overview of MRST parton distributions at $Q^2 = 20\,GeV^2$. Distributions are multiplied by x

discussed (cf. section 6.2.2). These experiments affect directly the determination of $G(x, Q^2)$ in the medium to large x gluons. The difference is clearly shown in figure 6.7.

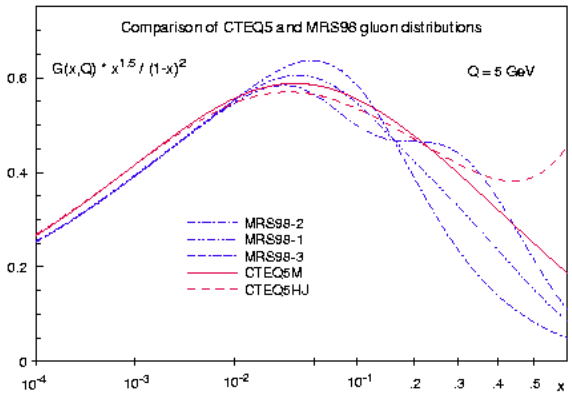

Fig. 6.7: Comparison of the gluon distributions from MRST with those from CTEQ5 at 5 GeV. In order to better show the differences, distributions are multiplied by $x^{1.5}/(1-x)^2$

The choice of input is the main cause of differences between the CTEQ5 and CTEQ6 PDFs as well. While the discrepancy among distributions of quarks is negligible, the most noticeable change occurs in the gluon distribution. In the moderate to high x range, $x > 0.01$, the inclusive jet data are now playing a very important role. The combined effects of the precision DIS and jet data have made a significant shift in the shape of the gluon distribution which is significantly harder for CTEQ6 than for CTEQ5M1 and all MRST PDF sets at all Q scales.

The gluon distribution is valid till x values of about 10^{-5}. For lower values no data are available and the shape provided comes from an extrapolation. Figures 6.8(a) and 6.8(b) show the comparison among the currently available PDFs parameterizations of CTEQ5 and MRST98 (both in the official CERN libraries) and of CTEQ6, respectively for LO and NLO calculation. It is clear that differences in the medium to large x gluons, though sensitive, especially for LO calculation, are totally overwhelmed by the ones in the low x, due to the different extrapolation chosen.

It will be shown soon that the muon spectrometer at the LHC can probe that region, providing additional constraints in this barely unknown phase space region.

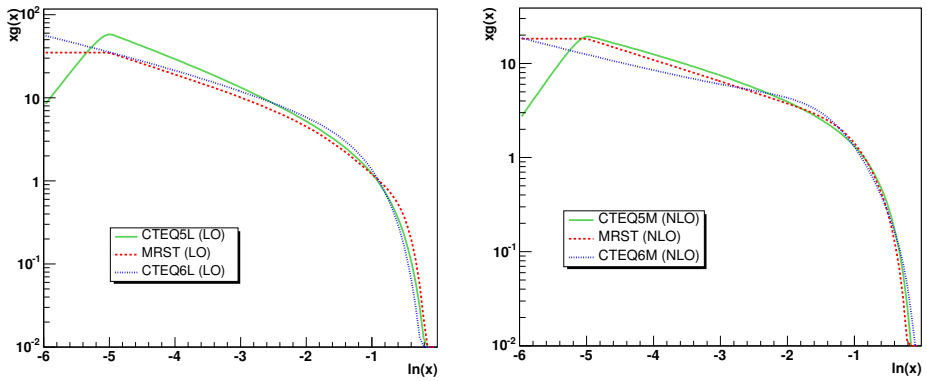

(a) LO calculation (b) NLO calculation

Fig. 6.8: Comparison of the gluon distributions from MRST with those from CTEQ

6.3 Probe of low x regions through J/ψ analysis

The main aim of this chapter is to show the possibility to probe low (and hence not yet well studied) x region inside proton through the analysis of J/ψ detected in the ALICE muon spectrometer. All the calculations that will be performed will be leading order.

At leading order, the heavy quark production in the collision between two protons can be seen as the reaction $q\bar{q}\,(gg) \rightarrow Q\bar{Q}$, with q (g) any quark (gluon) inside the proton and Q the heavy quark created. The Feynman diagrams involved are shown in the figure 6.9.

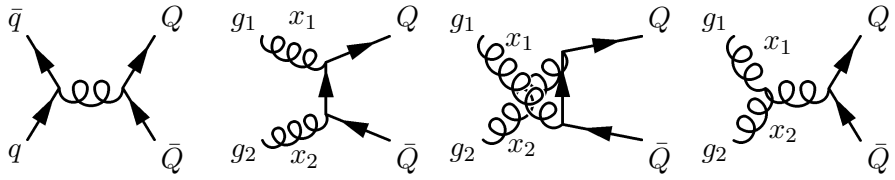

Fig. 6.9: Heavy quarkonia production Leading Order

The square of the heavy quark pair invariant mass is equal to the square of the center of mass energy of the initial quarks (or gluons), $\hat{s}$,

$$M^2_{Q\bar{Q}} = \hat{s} = x_1 x_2 s$$

where x_1 and x_2 are the gluon momentum fractions and $s = (14\ \text{TeV})^2$ is the square of the pp center of mass energy at LHC.

The longitudinal rapidity of the pair in the laboratory is given by[1]:

$$y = \frac{1}{2}\ln\left(\frac{E+p_z}{E-p_z}\right) = \frac{1}{2}\ln\left(\frac{x_1}{x_2}\right)$$

From these relation we get:

$$x_1 = \frac{M_{Q\bar{Q}}}{\sqrt{s}}e^{y_{Q\bar{Q}}} \qquad x_2 = \frac{M_{Q\bar{Q}}}{\sqrt{s}}e^{-y_{Q\bar{Q}}} \tag{6.1}$$

As the momentum fraction x is proportional to the heavy quark invariant mass, it is clear that charm probes smaller x than beauty. The (x_1,x_2) plane for charm and bottom measurement in pp collisions at 14 TeV is shown in figure 6.10 [35].

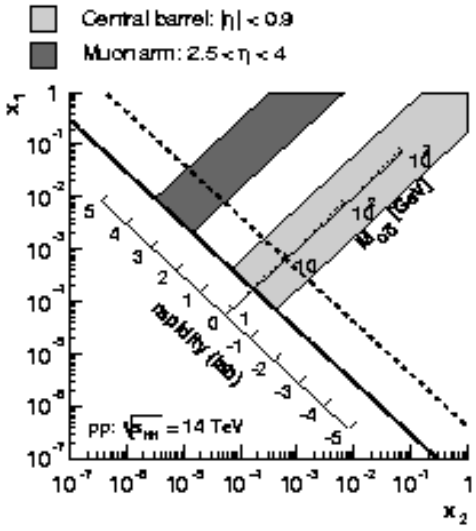

Fig. 6.10: ALICE heavy flavor acceptance in the (x_1,x_2) plane for pp collisions

In this plane, points of constant invariant mass lie on hyperbolae, which are straight lines in the log-log scale. The solid and dashed lines correspond to $c\bar{c}$ and $b\bar{b}$ pair production at threshold.

Let's consider the muon spectrometer rapidity acceptance for quarkonia ($2.5 < y < 4.0$, see A.2). From relation 6.1 it is possible to show that the minimum explored x is 3.14×10^{-6} for J/ψ and 1.18×10^{-5} for Υ. As we are interested in the region of $x < 10^{-5}$ it is clear that we have to focus our attention on the first meson. Figures 6.11(a) and 6.11(b) show the differences between the parton distribution functions in the x region respectively probed by J/ψ and Υ.

[1]The second equivalence of the rapidity formula holds only if we consider LO processes

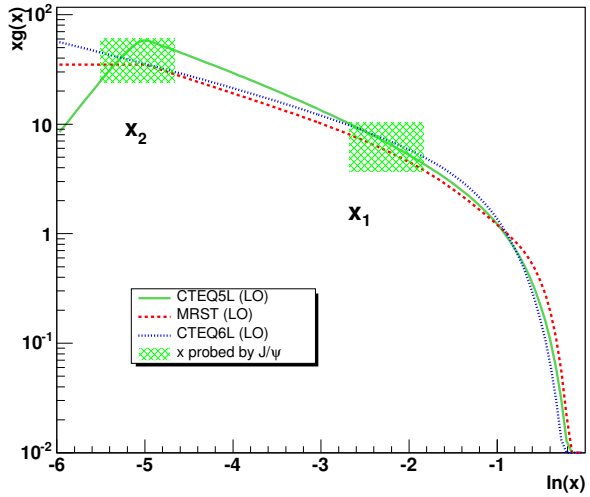

(a) LO calculation

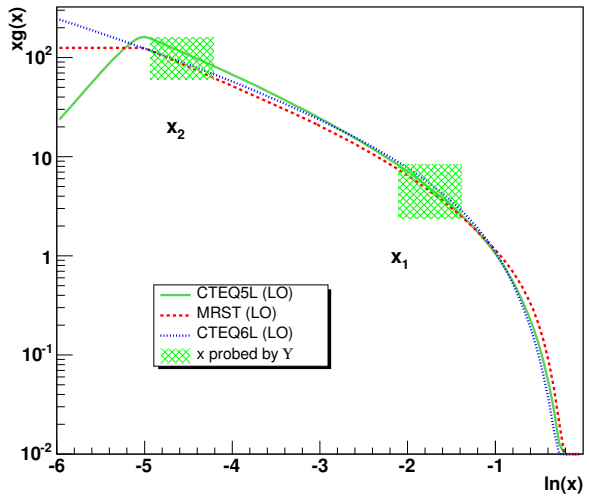

(b) NLO calculation

Fig. 6.11: Comparison of the gluon distributions from MRST with those from CTEQ. x regions probed by J/ψ and Υ are shown.

Let's recall the Color Evaporation Model formula given in equation 3.1, namely:

$$\sigma_C^{CEM} = F_C \sum_{i,j} \int_{4m_Q^2}^{4m_H^2} \mathrm{d}\hat{s} \int \mathrm{d}x_1 \mathrm{d}x_2 \, f_{i/A}(x_1,\mu^2) f_{j/B}(x_2,\mu^2) \hat{\sigma}_{ij}(\hat{s}) \delta(\hat{s} - x_1 x_2 s)$$

The total cross section for quarkonia production clearly depends on the parton distribution functions $f_{i/A}(x_1,\mu^2)$ and $f_{j/B}(x_2,\mu^2)$, but however it is not so sensitive to changes in the adopted PDF set. It is therefore convenient to

search for an observable that shows a stronger dependance on PDFs. A possible solution could be the rapidity differential cross section (see appendix B for details):

$$\frac{d\sigma_C^{CEM}}{dy} = \frac{F_C}{s} \sum_{i,j} \int_{4m_Q^2}^{4m_H^2} \mathrm{d}\hat{s}\, \hat{\sigma}_{ij}(\hat{s}) f_{i/A}(\sqrt{\frac{\hat{s}}{s}} e^{y}, \mu^2) f_{j/B}(\sqrt{\frac{\hat{s}}{s}} e^{-y}, \mu^2) \quad (6.2)$$

The central point of the chosen observable is that the *shape* of the differential cross section strongly depends on parton distribution functions.

In order to perform calculations we did two approximations:

1. in the elementary cross section $\hat{\sigma}_{ij}$, only the dominant contribution $gg \to Q\bar{Q}$ is taken into account
2. PDFs and cross section used are leading order

The first approximation is fairly good as at low x the gluon contribution becomes dominant, thus overwhelming the $q\bar{q}$ interaction. The second is a matter of consistency because the relation 6.1, necessary to pass from equation 3.1 to 6.2 holds only at leading order. Moreover the parton densities have to be of the appropriate order for the cross sections to be meaningful. A collaboration with theoreticians should be undertaken in order to push calculation to better precision.

The $gg \to Q\bar{Q}$ cross section can be easily calculated [36] and gives the following result:

$$\hat{\sigma}_{gg} = \frac{\pi \alpha_s^2(\mu_R)}{3\hat{s}} \left[-\frac{1}{4}\chi \left(7 + 31\frac{m_Q^2}{\hat{s}} \right) + \left(1 + 4\frac{m_Q^2}{\hat{s}} + \frac{m_Q^4}{\hat{s}^2} \right) \ln\left(\frac{1+\chi}{1-\chi} \right) \right]$$

with

$$\chi = \sqrt{1 - 4\frac{m_Q^2}{\hat{s}}}$$

where m_Q is the heavy quark mass and $\alpha_s(\mu_R)$ is the strong coupling constant evaluated at the renormalization scale μ_R. The value α_s is well known and can be easily calculated at all scales (cf. [37]). The scale is not totally arbitrary: it is related to the typical energies involved in the process. The color evaporation model prediction for J/ψ production (equation 3.1) performs an integration over a small range of center of mass energies, namely from the square of twice the quark mass ($4m_Q^2 = 5.76$ GeV) to the square of twice the mass of the lightest heavy flavored hadron produced ($4m_H^2 = 13.84$ GeV), thus strongly constraining the value of the scale. If we adopt a $\mu_R = 2.4$ GeV, corresponding to twice the charm mass, we get $\alpha_s(2.4) = 0.27612$.

Calculation with the described parameter leads to the result shown in figure 6.12(a). Figure 6.12(b) is a zoom of the rapidity region covered by the

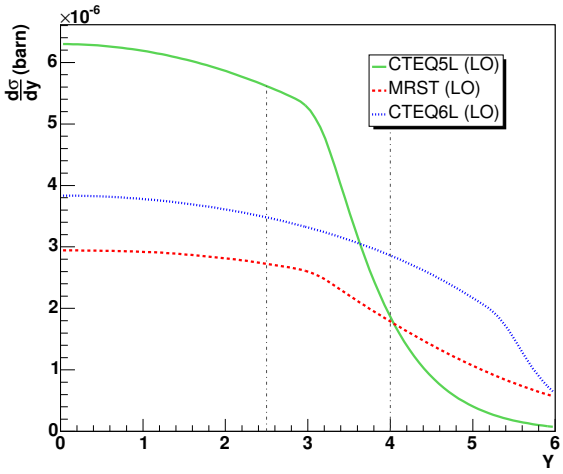

(a) Direct calculation results

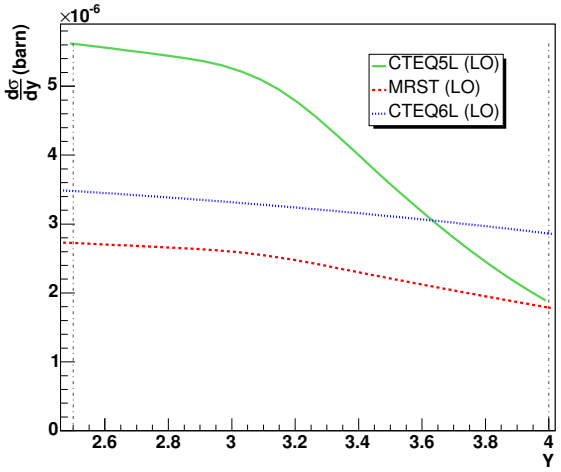

(b) Zoom in the rapidity acceptance

Fig. 6.12: Comparison between J/ψ rapidity distributions obtained with three different PDF sets

spectrometer acceptance that better shows the difference in the distribution slope for rapidity higher than 3, corresponding to values of $x < 10^{-5}$.

As we are interested only in the shape of the distribution, results obtained with the different PDFs can be normalized in such a way that the integral in the spectrometer rapidity acceptance ($2.5 < y < 4$) is 1, in order to better notice the discrepancies (figure 6.13). The slope of the rapidity distribution is strongly dependent on the input parton distribution function adopted. As expected, if we repeat the same procedure for Υ, differences between PDFs are not noticeable (figure 6.14).

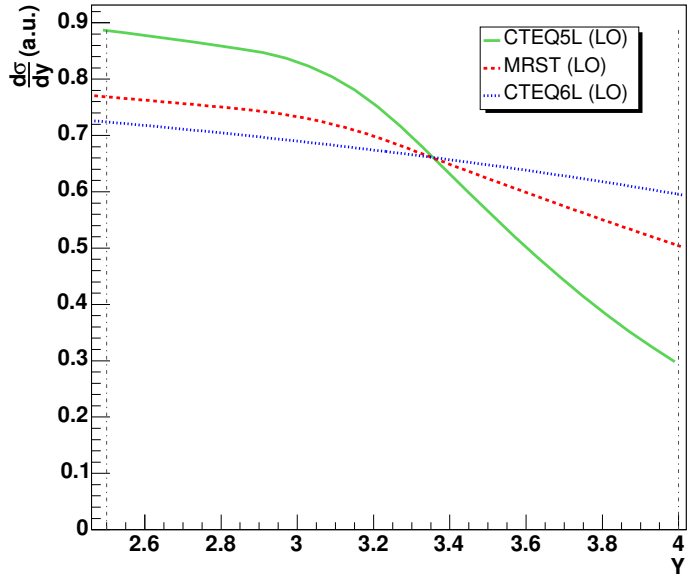

Fig. 6.13: Comparison between J/ψ rapidity distributions obtained with three different PDF sets (area in detector acceptance is normalized to 1).

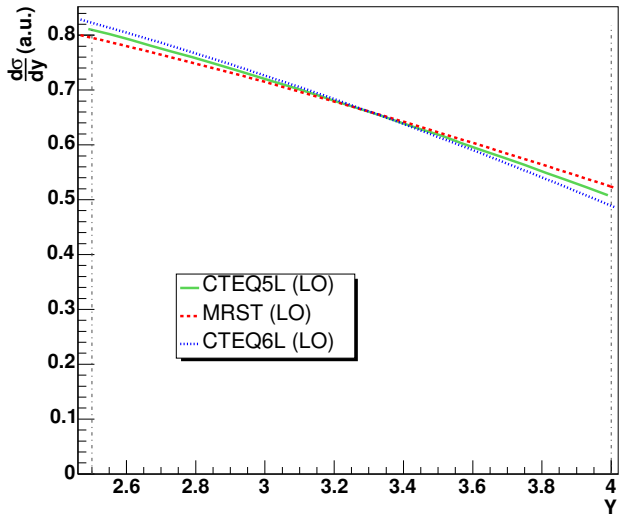

Fig. 6.14: Same as figure 6.13 but for Υ

It has however to be said that the experimental results on bottomonium will be, in any case, extremely important, since they will explore a new physical region. It is in fact true that the available data concern x values down to 10^{-5}, but such values are reached only at low scales, as it can be seen in figure 6.2. At the scale of the Υ ($\sim$ 10 GeV), the x region explored is

higher than few 10^{-3}, which is much larger than the values that the ALICE muon spectrometer can probe.

PDFs are calculated at a low scale ($\sim$ 1 GeV) and than their evolution with Q^2 is performed with the DGLAP equations (see section 6.2.2). Thus the bottomonium state could be exploited to probe the validity of such equations in a new physical region. Further studies should be performed on this topic, which is not discussed in this thesis.

The next step is to show that the accuracy of the data that will be taken with the ALICE muon spectrometer is adequate to distinguish between different PDFs. This analysis was performed using the results shown in section 5.2.3. In fact the input of the fast simulation is a parametrization of the J/ψ rapidity distribution obtained with the NLO MRST PDF set. Nevertheless if we compare the NLO input parameterization with the LO calculation, we notice that the differences involved are negligible (see figure 6.15), thus allowing us to directly compare simulation results to LO differential rapidity cross sections obtained from equation 6.2.

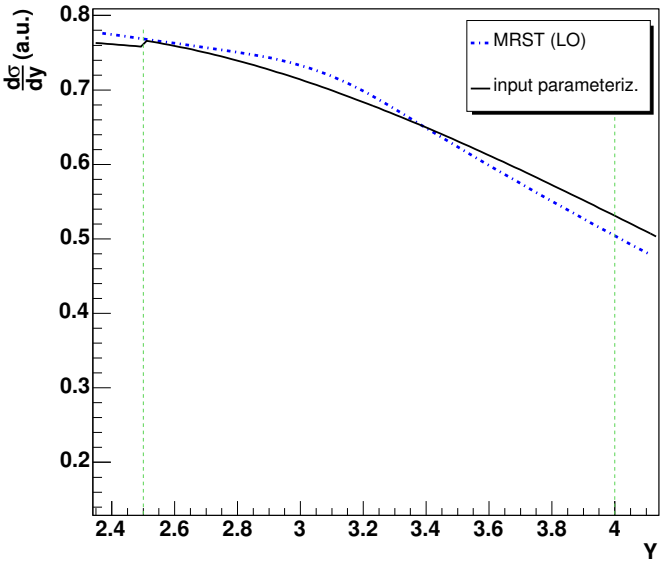

Fig. 6.15: Comparison between J/ψ rapidity distributions used in simulations (obtained with NLO MRST PDF) and the analogous with LO calculation. Area in detector acceptance is normalized to 1.

The simulation results and the rapidity distribution with different PDF sets, with their areas inside the spectrometer acceptance normalized to 1 are shown in figure 6.16.

It is possible to notice a slight difference between MRST and simulation, which is due to two main causes:

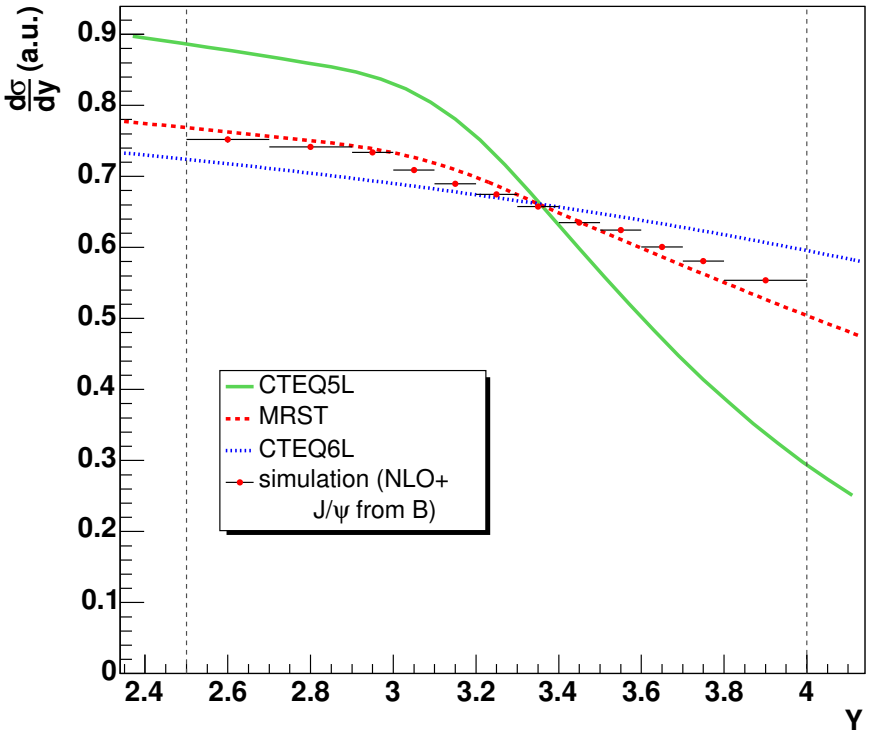

Fig. 6.16: Comparison between calculated J/ψ distribution and simulation results

1. the input parameterization of the adopted J/ψ prompt differential cross section is NLO, while calculation are LO

2. simulation results already take into account J/ψ from B mesons decay, thus slightly modifying the rapidity shape.

Moreover, for "historical" reasons (before the present work, the possibility that different PDFs could lead to such unlike results was not taken into account), the J/ψ mesons from B decay were obtained by adopting the CTEQ4L parton distribution. However we are confident that we didn't make relevant mistakes. The CTEQ4L is indeed practically equal to the CTEQ5L (see figure 6.17). B mesons are quite heavy, thus exploring x regions where CTEQ and MRST results are really similar, which allows us to confidently use one or the other without introducing significant discrepancies in rapidity distributions (cf. figure 6.14). For these reasons, despite of the differences previously explained, it can be concluded that the accuracy of data that will be taken in the spectrometer detector is good enough to distinguish between different PDFs used.

In conclusion, the possibility to probe gluon distribution for values of $x <$

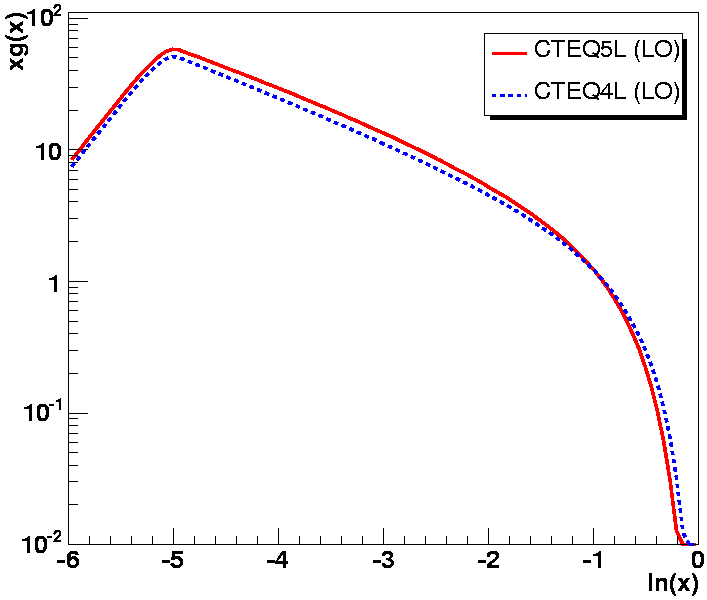

Fig. 6.17: Comparison between calculated CTEQ5L and CTEQ4L PDF sets

10^{-5} through the analysis of J/ψ detected by the ALICE muon spectrometer was shown.

In fact further work still has to be done. The next to leading order calculation should be performed, in order to get more accurate predictions. It could be even possible to substitute the adopted color evaporation model with a less phenomenological approach such as non-relativistic QCD. But clearly on this topic a collaboration with theoreticians would be welcome.

Finally the study could be extended to asymmetric collisions (such as pPb and Pbp). In that case it is predicted a $Q\bar{Q}$ rapidity shift of

$$\Delta y_{Q\bar{Q}} = \frac{1}{2} \ln \left(\frac{Z_1 A_2}{Z_2 A_1} \right)$$

with Z and A respectively the charge and mass number of the colliding nuclei. In the LHC case the pPb (Pbp) collisions will lead to a rapidity shift of $\Delta y = +0.47$ (-0.47) thus allowing a larger x_1 and x_2 coverage. This effect could be exploited in order to explore lower x values with J/ψ on one hand, and to allow the use of Υ as probe for $x < 10^{-5}$ on the other.

Chapter 7

Conclusions

In the present thesis, the ALICE muon spectrometer performance for heavy quarkonia detection has been studied.

Yields for charmonium and bottomonium states expected in 10^7 s of collected data with foreseen luminosity for pp collisions at 14 TeV at the LHC have been evaluated. The cross sections adopted are provided by the Color Evaporation Model (CEM).

The analysis was performed with the aid of fast simulation, which enables processing of the high statistics expected. The input parameterizations of quarkonia rapidity (y) and transverse momentum (p_T) distributions were provided, respectively, by CEM and by recent results from CDF data, opportunely scaled to LHC center of mass energies.

The simulation takes into account the correlated background, constituted by muons coming from heavy flavored hadron decays, but they do not yet include the combinatorial background. Though its contribution is expected to be only a fraction of the correlated one, the combinatorial background has to be added in the near future.

Simulation results end in very high statistics for J/ψ's, and high statistics for ψ' and bottomonium states, thus allowing an accurate analysis of quarkonia in different p_T and y bins, showing that p_T and y distributions can be precisely measured, at least for J/ψ's and Υ's. Further work has yet to be done for higher mass quarkonia, because, due to their lower statistics, they are influenced by the shape of the tails of $1S$ states.

The distributions were corrected for the muon spectrometer acceptance and divided by the integrated luminosity in order to obtain the J/ψ and Υ differential cross section in the interval $2.5 < y < 4.0$ (the detector acceptance).

The obtained p_T differential cross section for J/ψ and Υ can be used to provide very useful information on the quarkonia production mechanism. This topic has already been analyzed by CDF data, but the higher center

of mass energy and, most importantly, the possibility of studying quarkonia down to $p_T = 0$ will allow ALICE to contribute significantly to open questions.

During the course of the thesis it was for the first time noted that the y distributions of J/ψ in rapidity region covered by the ALICE muon spectrometer could provide important information on gluon distribution functions at low-x. At present the available data cover an x region down to 10^{-5} for energies on the order of charmonium state mass, and even higher x values for the energy scale of bottomonium. For lower x values, extrapolation are used for gluon distributions.

Leading Order calculations performed in the present thesis show that, owing to the high rapidity range covered by the ALICE muon spectrometer, the shape of the J/ψ rapidity differential cross section is sensitive to gluon distribution functions at low-x. In addition, the comparison with simulations suggests that the measured y distributions can, in principle, be used to constrain the gluon PDFs in the x range of sensitivity.

Appendix A

Kinematics and muon spectrometer acceptance

Despite of the complexity of the particle production in proton-proton collisions at LHC, which can be appropriately studied through numerical simulations, an approximate study of the pure kinematics can be performed, thus providing a deeper understanding of the phase space region accessible inside the detector acceptance.

In the following pages, a brief investigation of the kinematics of quarkonia production is presented. I will concentrate more in charmonium states, but the reasonings will apply to bottomonium states as well.

A.1 Momentum acceptance

As the muon spectrometer detects resonances decaying in muon pairs, the kinematics of the process is the two bodies one, which makes calculations easy.

In the muon pair center of mass rest frame[1], the momentum of the couple of particles produced is fixed and equal to[2]:

$$|\vec{p}_{\mu}^{*}| = \frac{\sqrt{M^2 - 4m^2}}{2}$$

with $\vec{p}_{\mu}^{*}$ = muon 3-momentum in the center of mass rest frame, M = resonance mass, m = muon mass.

In the passage from the center of mass frame to the laboratory one, the muons undergo a Lorentz boost. In this case two possible situations can occur, according to the relation between the boost and muon β. This leads to a momentum limit, $|\vec{p}_{res}^{lim}|$, for the resonance such that

[1] In the following all of the quantities related to the center of mass rest frame will be indicated with the apex *

[2] Here and in the following, Natural Units are adopted in formulae.

- $|\vec{p}_{res}| < |\vec{p}_{res}^{\,lim}| \Rightarrow$ a *lower* limit in the angle between muons in the laboratory occurs (when $\vartheta_\mu^* = \frac{\pi}{2}$)
- $|\vec{p}_{res}| > |\vec{p}_{res}^{\,lim}| \Rightarrow$ an *upper* limit in the angle between muons in the laboratory occurs

with $|\vec{p}_{res}|$ = resonance momentum, ϑ_μ^* = angle in the muon pair center of mass between the muon direction and the direction of the resonance in the laboratory.

Indicating with β_μ and β_{res} the speed of the muon and of the resonance respectively, the described limit condition is obtained when $\beta_\mu^* = \beta_{res}$. In formulae

$$\begin{aligned} \beta_\mu^* &= \frac{|\vec{p}_\mu^*|}{E_\mu^*} = \frac{\sqrt{M^2 - 4m^2}}{M} \\ \beta_{res} &= \frac{|\vec{p}_{res}|}{E_{res}} \\ |\vec{p}_{res}^{\,lim}| &= \frac{M\sqrt{M^2 - 4m^2}}{2m} \end{aligned}$$

Let's now consider the case $|\vec{p}_{res}| < |\vec{p}_{res}^{\,lim}|$, when a minimum angle ($\vartheta_{\mu\mu}^{min}$) between muons can be found. Due to the detector geometry, it exists a maximum angle between muons ($\vartheta_{det}^{max} = 18°$) such that they can both be detected, and it can be reached only when quarkonia are emitted along the beam axis ($\vartheta_{res} = 0$) (see figure A.1)

It is clear that muons are not in the spectrometer acceptance if $\vartheta_{\mu\mu}^{min} > \vartheta_{det}^{max}$.
We get:

$$\tan\vartheta_\mu = \frac{|\vec{p}_\perp^{\,\mu}|}{|\vec{p}_\parallel^{\,\mu}|} = \frac{\sqrt{M^2 - 4m^2}}{\gamma_{res}\beta_{res}M}$$

which leads:

$$\vartheta_{\mu\mu}^{min} = 2\arctan\frac{\sqrt{M^2 - 4m^2}}{|\vec{p}_{res}|} \tag{A.1}$$

The formula shows that as quarkonium momentum decreases, the minimum angle between muons increases. But $\vartheta_{\mu\mu}^{min}$ cannot be greater than 18 ° and thus we get:

$$|\vec{p}_{res}^{\,min}| = \frac{\sqrt{M^2 - 4m^2}}{\tan\frac{\vartheta_{det}^{max}}{2}} \tag{A.2}$$

Table A.1 summarizes the minimum momentum values of quarkonia analyzable by the spectrometer.

It is important to notice that all values of $|\vec{p}_{res}^{\,min}|\left(\frac{GeV}{c}\right)$ are less than $|\vec{p}_{res}^{\,lim}|\left(\frac{GeV}{c}\right)$, so that the calculations performed are consistent.

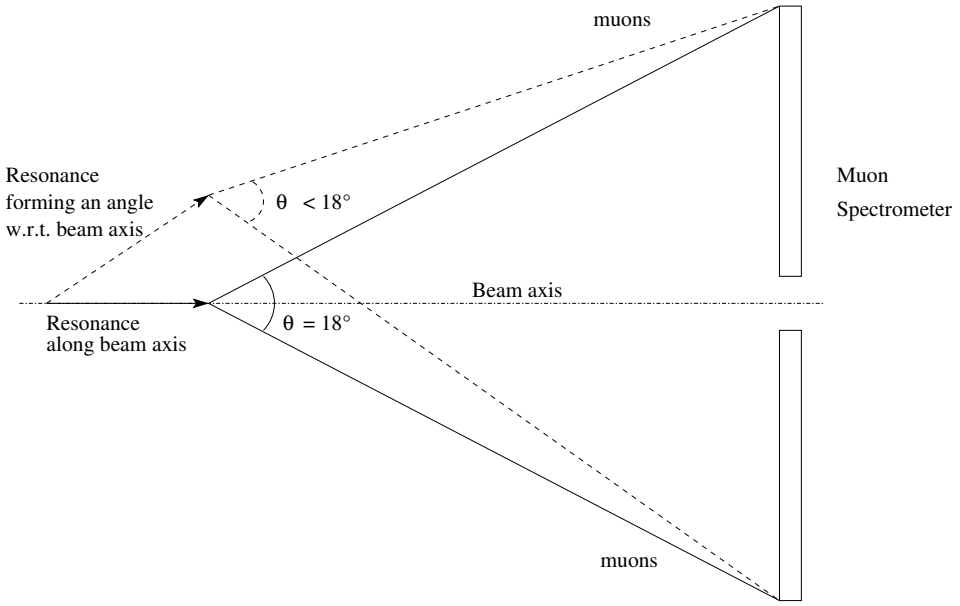

Fig. A.1: Maximum angle detector acceptance

Quarkonium	$\lvert\vec{p}_{res}^{\,min}\rvert \left(\frac{GeV}{c}\right)$	$\lvert\vec{p}_{res}^{\,lim}\rvert \left(\frac{GeV}{c}\right)$
J/ψ	19.508	45.28
ψ'	23.235	64.19

Tab. A.1: Minimum momentum values of charmonia analyzable by the muon spectrometer and charmonium states momenta above which the angles between muons have an upper limit instead of a lower one

Finally let's consider the case $|\vec{p}_{res}| > |\vec{p}_{res}^{\,lim}|$, searching for a maximum momentum value beyond which no quarkonia can be detected. If the resonance is emitted with an angle between 2° and 9°[3], its momentum has clearly no upper limit, as the higher it is, the narrower is the angle between muons that can in this way enter in the spectrometer acceptance.

A different situation is encountered when the resonance forms an angle less than 2° with the beam axis. If that condition is considered, the Lorentz boost can force muons to be produced in a small cone around the quarkonium direction, and the particles can pass through the hole in the middle of the detector itself. Calculations, performed numerically, show that the momentum of resonances has to be extremely high (more than 600 GeV/c for J/ψ), in order, for the cone width, to be less than the angular width of the detector hole ($\vartheta_{det}^{min} = 4^\circ$).

[3]See footnote at page 20

Figure A.2 shows the plot of the distribution of the angles between muons ($\vartheta_{\mu\mu}$) as a function of the J/ψ momentum. The red dots represent the $\vartheta_{\mu\mu}$

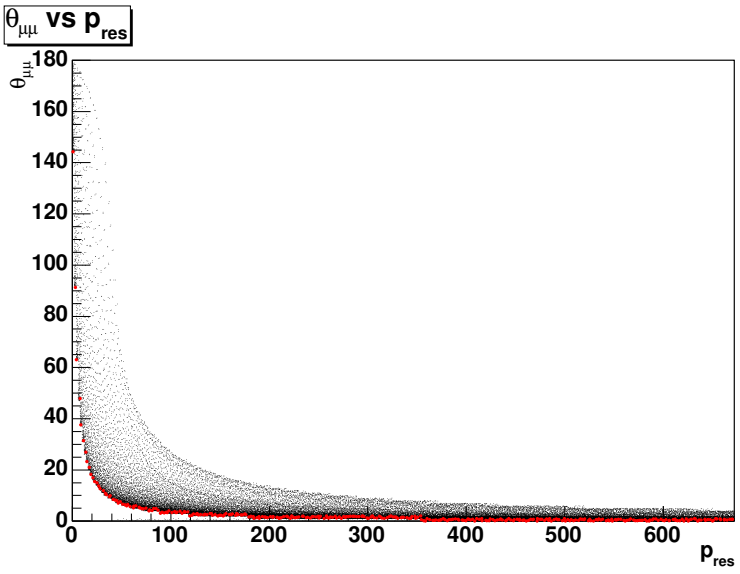

Fig. A.2: Angle between muons as a function of the quarkonium momentum

that we get when $\vartheta^*_\mu = \pi/2$. If we zoom in the region where $p_{res} > p^{lim}_{res}$ (see figure A.3), we notice that the Lorentz boost tends to distribute the bulk of the particles in the region close to such red dots. Thus, if we consider a quarkonium momentum slightly larger than the one for which the angle between muons produced at $\pi/2$ in the resonance rest frame becomes less than (ϑ^{min}_{det}), we can see that the number of detectable pairs become very low.

Therefore, we can conclude that the expression

$$|\vec{p}^{\,max}_{res}| = \frac{\sqrt{M^2 - 4m^2}}{\tan\frac{\vartheta^{min}_{det}}{2}} \tag{A.3}$$

can give a rough estimate of the maximum quarkonium momentum for which a consistent part of the muon pairs can be detected.

This result is extremely important in order to understand the rapidity acceptance discussed in the following section.

A.2 Rapidity acceptance

Rapidity and pseudorapidity are two important physical variables which are strictly correlated among each other. In particular if we call p, m and γ

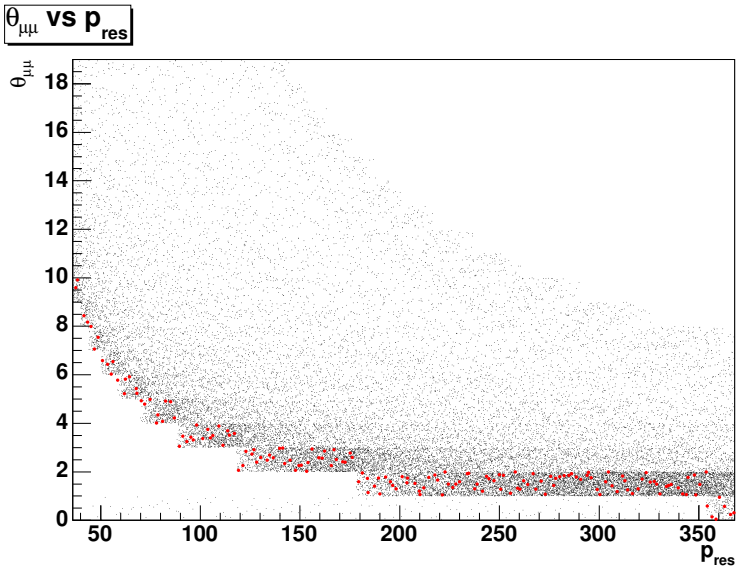

Fig. A.3: Angle between muons as a function of the quarkonium momentum. Zoom.

respectively the momentum, the mass and the Lorentz factor of a particle, and if we define as ϑ the angle with respect to the beam axis, which is chosen to be the z axis, we get that pseudorapidity is approximately equal to rapidity when $p \gg m$ and $\vartheta \gg 1/\gamma$.

In the present thesis a big part of the analysis was made by studying different rapidity bins, so it is oppotune to get a better understanding of this physical variable and of the spectrometer acceptance.

The pseudorapidity, defined as

$$\eta = -\ln \tan \frac{\vartheta}{2}$$

has a pure geometrical meaning, being related only to the angle that the particle makes with the beam axis. In the case of the ALICE, as the muon spectrometer covers the azimuthal region $2\,^\circ < \vartheta < 9\,^\circ$, we can easily estimate that the corresponding pseudorapidity region is $2.5 < \eta < 4.05$.

A more complex case is instead offered by the rapidity, defined as

$$y = \frac{1}{2} \ln \left(\frac{E + p_z}{E - p_z} \right)$$

with E and p_z the particle energy and the momentum along the beam axis. The quantity actually depends both on the geometry and the kinematics.

It is clear that with the ALICE muon spectrometer it is possible to measure quarkonia with $\eta = 0$, but this doesn't correspond to an infinite

rapidity. In fact the conditions necessary to get a divergent rapidity are:

$$y \to \infty \Leftrightarrow E = p_z \Leftrightarrow \begin{cases} m = 0 \quad or \quad |\vec{p}| \to \infty \\ \vartheta = 0 \end{cases}$$

This can be easily understood if we rewrite the rapidity as:

$$y = \frac{1}{2} \ln \left(\frac{\sqrt{tan^2\vartheta + 1 + \frac{m^2}{p_z^2}} + 1}{\sqrt{tan^2\vartheta + 1 + \frac{m^2}{p_z^2}} - 1} \right)$$

As previously seen (cf. section A.1) the two conditions cannot be satisfied at the same time because $|\vec{p}| \to \infty$ only if $2\,^\circ < \vartheta < 9\,^\circ$, while if $\vartheta = 0$ quarkonia must have a momentum less than the one showed in equation A.3 in order to be detected. The maximum rapidity corresponds then to one of these two situations, that can be numerically evaluated. Results are shown in table A.2.

$\vartheta = 0$		
Quarkonium	$\lvert\vec{p}_{res}^{\,max}\rvert \left(\frac{GeV}{c}\right)$	y_{res}^{max}
J/ψ	88.477	4.046
ψ'	105.382	4.046

$\vartheta = 2\,^\circ \qquad \lvert\vec{p}_{res}\rvert \to \infty$	
Quarkonium	y_{res}^{max}
J/ψ	4.0481
ψ'	4.0481

Tab. A.2: Maximum rapidity values of charmonia analyzable by the muon spectrometer

The evaluation of the minimum rapidity value is a more difficult task. As rapidity increases when ϑ decreases, one could say that the minimum value is obtained with the maximum angle with respect to beam axis, i.e. $9\,^\circ$. Unfortunately muons coming from quarkonium decay lay in a cone around the mother particle direction whose width decreases with momentum. Thus as far as quarkonium direction gets closer to detector acceptance, its momentum has to grow so that the cone inside which muons lay is entirely inside the spectrometer acceptance. Unfortunately rapidity grows with momentum and the absolute minimum value it can get depends on the combining action of angle and momentum which have opposite effects. So the precise value has to be determined through simulations, and it is found to be about 2.5.

However, considering that it is about the same value for all the resonances, we can suppose that it is determined by geometrical reasons more than kinematical ones. So we can make an approximate calculation taking into account the condition $\vartheta \to 9\,^\circ$ and $|\vec{p}| \to \infty$, which gives a value of $y_{res}^{min} = 2.542$.

Appendix B

From the CEM formula to the rapidity differential cross section

In the following section, the algebraic calculations that lead from the color evaporation model formula for quarkonia production of equation 3.1 to the rapidity differential cross section of equation 6.2 will be shown.

Let's recall again the first formula:

$$\sigma_C^{CEM} = F_C \sum_{i,j} \int_{4m_Q^2}^{4m_H^2} \mathrm{d}\hat{s} \int \mathrm{d}x_1 \mathrm{d}x_2 \, f_{i/A}(x_1, \mu^2) f_{j/B}(x_2, \mu^2) \hat{\sigma}_{ij}(\hat{s}) \delta(\hat{s} - x_1 x_2 s)$$

In order to perform the integration over x_2, it is necessary to write the Dirac delta in a suitable way, namely $\delta(x_2 - x_2^0)$. We use a property which states:

$$\delta(f(x) - f(x_0)) = \frac{\delta(x - x_0)}{|f'(x_0)|}$$

where $f'(x_0)$ is the prime derivative of function $f(x)$ calculated in x_0.
In our case $f(x_2) = x_1 x_2 s$ and $f(x_2^0) = \hat{s}$, thus

$$\delta(\hat{s} - x_1 x_2 s) = \frac{\delta(x_2 - \frac{\hat{s}}{x_1 s})}{x_1 s}$$

If we now perform the integration over x_2 we get:

$$\sigma_C^{CEM} = F_C \sum_{i,j} \int_{4m_Q^2}^{4m_H^2} \mathrm{d}\hat{s} \int \frac{\mathrm{d}x_1}{x_1 s} \, f_{i/A}(x_1, \mu^2) f_{j/B}(\frac{\hat{s}}{x_1 s}, \mu^2) \hat{\sigma}_{ij}(\hat{s})$$

Let's recall again the relation (equation 6.1) occurring between x and the rapidity y, namely :

$$x_1 = \sqrt{\frac{\hat{s}}{s}} \, e^{y_{Q\bar{Q}}} \qquad x_2 = \sqrt{\frac{\hat{s}}{s}} \, e^{-y_{Q\bar{Q}}}$$

From the CEM formula to the rapidity differential cross section

If we substitute these relations inside the integral we find that $\mathrm{d}x_1 = x_1 \mathrm{d}y$, and hence:

$$\sigma_C^{CEM} = \frac{F_C}{s} \sum_{i,j} \int_{4m_Q^2}^{4m_H^2} \mathrm{d}\hat{s} \int \mathrm{d}y f_{i/A}(\sqrt{\frac{\hat{s}}{s}} e^y, \mu^2) f_{j/B}(\sqrt{\frac{\hat{s}}{s}} e^{-y}, \mu^2) \hat{\sigma}_{ij}(\hat{s})$$

Deriving both sides with respect to rapidity we finally get:

$$\frac{d\sigma_C^{CEM}}{dy} = \frac{F_C}{s} \sum_{i,j} \int_{4m_Q^2}^{4m_H^2} \mathrm{d}\hat{s}\, \hat{\sigma}_{ij}(\hat{s}) f_{i/A}(\sqrt{\frac{\hat{s}}{s}} e^y, \mu^2) f_{j/B}(\sqrt{\frac{\hat{s}}{s}} e^{-y}, \mu^2)$$

Appendix C

Detection probability

One of the most important part of a simulation is the determination of the detection probability, which is a convolution of the geometrical acceptance and the trigger and tracking reconstruction efficiency. Its determination requires the knowledge of kinematic distributions of both produced and detected particles. The detection probability can depend on several observables, but in the following it will be considered only as a function of the transverse momentum p_T and the rapidity y.

The total number of produced particles depends on luminosity ($\mathcal{L}$), cross section (σ) and acquisition time (t) (see equation 5.2). Nevertheless, if we don't directly measure those particles, we are interested only in the ones decaying in the products that can be detected. The number of such events is

$$N_{prod} = BR\mathcal{L}t \int \mathrm{d}p_T \int \mathrm{d}y \frac{\mathrm{d}^2\sigma}{\mathrm{d}p_T\,\mathrm{d}y}$$

where BR is the branching ratio in the considered process.

The number of revealed particles is instead

$$N_{det} = BR\mathcal{L}t \int \mathrm{d}p_T \int \mathrm{d}y \frac{\mathrm{d}^2\sigma}{\mathrm{d}y\mathrm{d}p_T}\,\varepsilon(p_T, y)$$

where $\varepsilon(p_T, y)$ is the detection probability,

The total detection efficiency is clearly defined as

$$\varepsilon = \frac{N_{rev}}{N_{prod}}$$

If we are instead interested in the efficiency as a function of one of the two variables, let's say p_T but the case for y is analogous, we have

$$\varepsilon(p_T) \overset{def}{\equiv} \frac{\frac{\mathrm{d}N_{riv}}{\mathrm{d}p_T}}{\frac{\mathrm{d}N_{prod}}{\mathrm{d}p_T}} = \frac{\int \mathrm{d}y \frac{\mathrm{d}^2\sigma}{\mathrm{d}y\mathrm{d}p_T}\,\varepsilon(p_T, y)}{\int \mathrm{d}y \frac{\mathrm{d}^2\sigma}{\mathrm{d}y\mathrm{d}p_T}}$$

List of Tables

List of Figures

LIST OF FIGURES

Bibliography

[1] J. Rafelski and J. Letessier. **Strangeness and Quark Gluon Plasma**. *J.Phys. G30*, pages S1–S28, 2004. arXiv:hep-ph/0305284.

[2] D. Elia. **Strange particle production in 158 and 40 A GeV/c Pb-Pb and p-Be collisions**. *J. Phys. G: Nucl. Part. Phys. 31*, pages S135–S140, 2005.

[3] T. Matsui and H. Satz. **J/ψ Suppression by Quark-Gluon Plasma Formation**. *Phys. Lett. B178*, pages 416–422, 1986.

[4] NA50 Collaboration. **A new measurement of J/ψ suppression in *PbPb* collisions at 158 GeV per nucleon**. *Eur.Phys.J. C39*, pages 335–345, 2005. arXiv:hep-ex/0412036.

[5] H. Satz. **Color Deconfinement in Nuclear Collisions**. *Rep.Prog.Phys. 63*, pages 1151–1574, 2000. arXiv:hep-ph/0007069.

[6] ALICE collaboration. **ALICE: Physics Performance Report, Volume I**. *J.Phys. G: Nucl.Part.Phys. 30*, pages 1517–1763, 2004.

[7] H. Satz. **The SPS Heavy Ion Programme**. *Phys.Rep. 403-404*, pages 33–50, 2004. arXiv:hep-ph/0405051.

[8] ALICE Collaboration. **The forward muon spectrometer. Addendum to the ALICE Technical Proposal**. Technical report, CERN, 15 October 1996. LHCC 96-32 / LHCC P3 Add.1.

[9] R. Arnaldi et al. **Spatial resolution of RPC in streamer mode**. *Nucl.Instrum. and Methods A490*, pages 51–57, 2002.

[10] E. Vercellin. **ALICE**. *Eur.Phys.J. A19*, pages 223–228, 2004.

[11] ALICE Collaboration. **ALICE. Technical Design Report of the Dimuon Forward Spectrometer**. Technical report, CERN, 13 August 1999. LHCC 99-22 / ALICE TDR 5.

[12] ALICE Collaboration. **ALICE. Technical Proposal for A Large Ion Collider Experiment at the CERN LHC**. Technical report, CERN, 15 December 1995. LHCC 95-71 / LHCC P3.

[13] R. Vogt. **The A Dependence of Open Charm and Bottom Production**. *Int.J.Mod.Phys. E12*, pages 211–270, 2003. arXiv:hep-ph/0111271.

[14] F. Abe et al. **J/ψ and ψ(2S) Production in $p\bar{p}$ Collisions at $\sqrt{s}$ = 1.8 TeV**. *Phys.Rev.Lett. 79*, page 572, 1997.

[15] N. Brambilla et al. **Heavy Quarkonium Physics**. *arXiv:hep-ph/0412158*, 2004.

[16] V. D. Barger, W. Y. Keung, and R. J. Phillips. **On ψ and Υ production via gluons**. *Phys.Lett. B91*, pages 253–258, 1980.

[17] R. Gavai, D. Kharzeev, H. Satz, G. A. Schuler, K. Sridhar, and R. Vogt. **Quarkonium Production in Hadronic Collisions**. *Int.J.Mod.Phys. A10*, pages 3043–3070, 1995. arXiv:hep-ph/9502270.

[18] G. T. Bodwin and G. P. Lepage E. Braaten. **Rigorous QCD Analysis of Inclusive Annihilation and Production of Heavy Quarkonium**. *Phys.Rev. D51*, pages 1125–1171, 1995. arXiv:hep-ph/9407339.

[19] **CDF experiment homepage**. http://www-cdf.fnal.gov/index.html.

[20] D. Acosta et al. **Measurement of the J/ψ Meson and b-Hadron Production Cross Sections in $p\bar{p}$ Collisions at $\sqrt{s}$ = 1960 GeV**. *Phys.Rev. D71*, page 032001, 2005. arXiv:hep-ex/0412071.

[21] G. T. Bodwin, E. Braaten, and J. Lee. **Comparison of the color-evaporation model and the NRQCD factorization approach in charmonium production**. *arXiv:hep-ph/0504014*, 2005.

[22] F. Abe et al. **Production of J/ψ Mesons From χ_c Meson Decays in $p\bar{p}$ Collisions at $\sqrt{s}$ = 1.8 TeV**. *Phys.Rev.Lett 79*, page 578, 1997.

[23] P. Cortese. Private communication.

[24] M. L. Mangano, P. Nason, and G. Ridolfi. **Heavy-quark Correlations in Hadron Collisions at Next-to-Leading Order**. *Nucl.Phys. B431*, page 453, 1994.

[25] Accardi et al. **Hard Probes in Heavy Ion Collisions at the LHC: PDFs, Shadowing and pA collisions**. *arXiv:hep-ph/0308248*, v1, 2003.

[26] T. Sjostrand. **PYTHIA 5.7 and JETSET 7.4 Physics and Manual**. *arXiv:hep-ph/9508391*, 1995.

[27] A. Colla. ***Study of Charmonium Production and Suppression in Indium-Indium Collisions at 158 GeV/nucleon***. phD, Università degli Studi di Torino. Facoltà di Scienze MFN, 2004.

[28] R. Guernane, P. Crochet, A. Morsch, and E. Vercellin. **Measuring the *b*-Meson Production Cross Section in 5.5 TeV $Pb-Pb$ Collisions Using Semileptonic Decay Muons**. ALICE-INT-2004-v1.0, 2004.

[29] **ROOT hompage**. http://www.root.cern.ch.

[30] H. L. Laif, J. Hustond, S. Kuhlmanna, J. Morfinb, F. Olnesse, J. F. Owensc, J. Pumplind, and W. K. Tung. **Global QCD Analysis of Parton Structure of the Nucleon: CTEQ5 Parton Distributions**. *Eur.Phys.J. C12*, pages 375–392, 2000. arXiv:hep-ph/9903282.

[31] A. D. Martin, R. G. Roberts, W. J. Stirling, and R. S. Thorne. **Parton distributions : a new global analysis**. *Eur.Phys.J. C4*, pages 463–496, 1998. arXiv:hep-ph/9803445.

[32] James Botts, Jorge G. Morfin, Joseph F. Owens, Jianwei Qiu, Wu-Ki Tung, and Harry Weerts. **CTEQ Parton Distributions and Flavor Dependence of Sea Quarks**. *Phys.Lett. B304*, pages 159–166, 1993. arXiv:hep-ph/9303255.

[33] J. Pumplin, D.R. Stump, J. Huston, H.L. Lai, and P. Nadolsky andW.K. Tung. **New Generation of Parton Distributions with Uncertainties from Global QCD Analysis**. *JHEP 0207*, page 012, 2002. arXiv:hep-ph/0201195.

[34] M. Bedjidian et al. **Hard Probes in Heavy Ion Collisions at the LHC: Heavy Flavor Physics**. *arXiv:hep-ph/0311048*, v1, 4 November 2003.

[35] N. Carrer and A. Dainese. **Charm and beauty production at LHC**. *ALICE Collaboration Note*, 2003. arXiv:hep-ph/0311225.

[36] B. L. Combridge. **Associated Production of Heavy Flavor States in pp and $\bar{p}p$ Interactions: Some QCD Estimates**. *Nucl.Phys. B151*, page 429, 1979.

[37] S. Eidelman et al. **Review of Particle Physics**. *Phys.Lett. B592*, page 1, 2004. http://pdg.lbl.gov/.

Ringraziamenti (Acknowledgements)

E così, dopo 10 mesi di gestazione, parte dei quali trascorsi ad argomentare in C++ con il calcolatore, il presente lavoro vede infine la luce.

Non si tratta della conclusione di un percorso, iniziato cinque anni or sono, quanto piuttosto di una tappa di esso, una tappa importante. Fortunatamente, lungo il cammino ho avuto modo di incontrare molte persone che, in modi diversi, mi hanno aiutato a giungere sin qui e alle quali va tutta la mia riconoscenza.

Confesso che, al termine di una tesi scritta interamente in inglese, lingua cui chiedo venia per aver tanto indecorosamente maltrattato durante la stesura, è con immenso sollievo che torno all'italiano, che mi consente di tingere con sfumature diverse un unico immenso

Grazie!!

Ai miei genitori, e non solo per la tesi o per gli ultimi cinque anni, ma anche, e soprattutto, perché mi sono stati accanto e mi hanno sostenuto sempre.

Al prof. Lorenzo Magnea, per le illuminanti discussioni sulla parte di impronta più fenomenologica della tesi, inerente alle funzioni di distribuzione partonica.

Al gruppo Pinot, che oggi come due anni fa mi ha accolto con stima e simpatia. Al prof. Emilio Chiavassa, al prof. Mauro Gallio, a Nora, ad Alfredo, a Giovanna e ancora al prof. Giuseppe Dellacasa e ad Anna che mi hanno seguito passo passo durante la tesi di laurea triennale.

A Pietro, Chiara, Enrico ed Alessandro, sempre disponibili a chiarirmi

dubbi e/o ad aiutarmi nell'ancestrale disputa tra l'uomo ed aliroot.

A Roberta, di cuore. Perché ha pazientemente resistito alla tempesta di domande che quasi quotidianamente si abbatteva su di lei e mi ha fornito preziosissimi consigli.

Une autre fois, merci à Rachid pour sa précieuse contribution.

A Roberto, Frederic, Francesca, Martino e Alberto i miei compagni dottorandi o (da poco) post-doc.

All'allegra compagnia di fisici conosciuti qui 5 anni or sono, che mi hanno accompagnato in questa avventura attraverso lezioni, esami, gite in montagna e lunghi pranzi.

Ad una piccola parte di questa compagnia, in modo particolare: a Riccardo ed Alessandro con cui ho affrontato tutti i laboratori, dal primo al sesto... ed oltre.

Agli amici di Andezeno, gli amici di sempre.

E infine al mio relatore, prof. Ermanno Vercellin. Alla sua disponibilità ed alla stima che mi ha sempre mostrato: una guida davvero insostituibile, lungo tutto il corso della tesi.